

Excitation of resonant plasmonic cavities by integrated waveguides for sensing applications

THÈSE N° 7198 (2016)

PRÉSENTÉE LE 2 DÉCEMBRE 2016

À LA FACULTÉ DES SCIENCES ET TECHNIQUES DE L'INGÉNIEUR

LABORATOIRE D'OPTIQUE APPLIQUÉE

PROGRAMME DOCTORAL EN PHOTONIQUE

ÉCOLE POLYTECHNIQUE FÉDÉRALE DE LAUSANNE

POUR L'OBTENTION DU GRADE DE DOCTEUR ÈS SCIENCES

PAR

Gaël David OSOWIECKI

acceptée sur proposition du jury:

Prof. C. Moser, président du jury
Prof. H. P. Herzig, directeur de thèse
Prof. H. Zappe, rapporteur
Prof. C. Rockstuhl, rapporteur
Prof. Y. Bellouard, rapporteur



ÉCOLE POLYTECHNIQUE
FÉDÉRALE DE LAUSANNE

Suisse
2016

Abstract

Optical sensors represent a large growing market which is nowadays focusing onto advancement in mobile technology. Innovations in the field of optical sensors are mostly driven by the technological advancements in the domain of micro & nanofabrication. One key to the miniaturization of optical sensors is their integration onto small chips having their own light sources and detectors. This thesis shows two separate applications of integrated optical sensors which benefit from the implementation of optical nano-structures.

A first study investigates a biosensor based on a plasmonic slot waveguide cavity for the detection of changes in refractive index in femto-liter volumes. By integrating the biosensor onto a silicon-on-insulator platform, we could confine the light excitation of the cavity into a single-mode silicon strip waveguide. In a first step realized by simulation, we showed the efficient coupling of the fundamental quasi-transverse electric mode of the waveguide to the plasmonic slot waveguide cavity. We showed that the strong light confinement into the slot is an intrinsic property of the plasmonic slot waveguide which is based on the excitation of a guided wave at a metal-insulator-metal interface. We investigated the surface sensitivity of this biosensor which revealed its potential to detect single-molecules at high concentrations. Moreover, we reported a high bulk sensitivity of up to 600nm per refractive index units. In a second step, we developed a multi-step process based on electron beam lithography to fabricate the sensor. In a third step, we characterized the propagation properties of the fabricated waveguides. Finally, we measured the transmission properties of the integrated sensor as well as the far-field scattering of the plasmonic cavity.

A second study focused on a new architecture of a standing-wave integrated Fourier transform spectrometer. This type of spectrometer uses nano-samplers (metallic nano-structures) to probe the intensity of a standing wave generated inside a single-mode waveguide terminated by a mirror. To enhance the well known bandwidth limitation of this type of spectrometer, we implemented a scanning mirror enabling the sub-sampling of the interferogram between each fixed nano-sampler. We fabricated a chip containing a 1D array of low Δn single-mode waveguides made out of epoxy-based "EpoCore" polymer. Equidistant metallic nano-samplers were patterned on top of the waveguides thanks to electron beam lithography. Micro-lenses were fabricated, aligned and glued to the facet of the chip to enable the free space coupling of the waveguides. We implemented a mechanical setup which included a closed-loop piezo actuated mirror to induce an additional phase shift to the interferogram. The realization of an optical setup taking care of the readout of the interferogram showed a 2D multiplexing potential of the spectrometer by realizing the simultaneous detection of independent waveguides.

We also investigated the calibration procedures to overcome the fabrication uncertainties by an adapted post-processing step.

Key words: Sensors, Biosensing, Nano-photonics, Plasmonics, Waveguides, Fourier transform spectrometer, SWIFTS.

Résumé

De nos jours, les capteurs optiques représentent un marché en pleine expansion qui se concentre sur les technologies mobiles. Les innovations au sein de ce domaine sont nourries par les avancements technologique de la micro- & nano-fabrication. Une des clés menant à la miniaturisation de ces capteurs optiques est leur intégration dans une puce contenant aussi bien les sources que les détecteurs de lumière.

La présente thèse expose deux différentes applications de capteurs optiques intégrés qui reposent sur l'implémentation de structures optique nanométriques.

Une première étude s'est concentrée sur un biosenseur optique basé sur une cavité de type guide d'ondes plasmonique à fente pour la détection de changement d'indice de réfraction dans des volumes de l'ordre du femto-litre. En intégrant ce biosenseur dans une puce basée sur une structure de type silicium sur isolant, nous avons pu confiner la lumière servant à exciter les cavités à l'intérieur de guides d'ondes monomodes en silicium. Dans une première phase de simulation, nous avons pu trouver un couplage efficace du mode d'excitation fondamental transverse électrique du guide d'ondes à la cavité plasmonique. Nous avons ensuite montré que la forte concentration de la lumière à l'intérieure de la fente de la cavité à guide d'ondes plasmonique est une propriété intrinsèque des modes guidés au interfaces de type métal-diélectrique-métal. D'une part, nous avons constaté par simulation des valeurs de sensibilité volumique de l'ordre de 600nm par indice de réfraction. D'autre part nous avons étudié la sensibilité surfacique du capteur aux changements d'indice de réfraction. Celle-ci étant très élevée, elle démontre finalement le potentiel de ce biosenseur à détecter des molécules isolées dans un liquide qui en contient une concentration élevée. Dans une deuxième phase, nous avons développé un procédé de fabrication basé sur la lithographie par faisceau d'électron comprenant de multiples étapes lors de la mise en œuvre du capteur. Dans une troisième phase, nous avons caractérisé les propriétés de guidage des guides d'ondes fabriqué. Le capteur fonctionnant en analysant la lumière transmise à travers les guides a également été caractérisé. Finalement, nous avons effectué la mesure du spectre de la lumière diffusée par la cavité plasmonique afin de la comparer aux résultats obtenus par transmission.

Une deuxième étude a été consacré à la réalisation d'une nouvelle architecture d'un spectromètre intégré à transformé de Fourier. Ce type de spectromètre utilise des nano-échantillonneurs (nanostructures en métal) pour sonder l'intensité d'une onde stationnaire présente à l'intérieur d'un guide d'ondes monomode terminé par un miroir. Pour élargir la largeur de bande qui est reconnue être une limitation majeure de ce type de spectromètre, nous avons tout d'abord implémenté un miroir mobile étant capable de palier au problème de sous-échantillonnage

en induisant des différences de chemin optique supplémentaires. Nous avons ensuite fabriqué une puce contenant un réseau unidimensionnel de guides d'ondes à faible différence d'indice Δn fait de polymère à base d'époxy appelé EpoCore. Des nano-échantillonneurs équidistants ont été évaporés sur le dessus des guides d'ondes qui avaient été auparavant exposés par lithographie par faisceau d'électron. Des microlentilles ont ensuite été fabriquées, alignées et collées sur la facette des puces pour faciliter l'injection de la lumière à l'intérieur des guides d'ondes. Nous avons alors implémenté un dispositif mécanique sur lequel est placée la puce incluant un miroir pouvant être déplacé par un actuateur piézo-électrique commandé par un contrôle en boucle fermée. Finalement nous avons réalisé un système de lecture optique complet de l'interférogramme incluant le dispositif mécanique qui a démontré le potentiel de multiplexage bidimensionnel de la mesure de spectre par de multiples guides d'ondes adjacent. Nous avons par ailleurs aussi étudié les procédures de calibration nécessaires pour corriger les imperfections dues à la fabrication.

Mots clefs : Capteur, Biosenseur, Nano-photonique, Plasmonique, Guide d'ondes, Spectrométrie par transformée de Fourier, SWIFTS.

V

Contents

2.3.3.1	Waveguide injection setup	29
2.3.3.2	Wavelength interrogation method	30
2.3.3.3	Broadband measurement set-up	30
2.3.3.4	Far field scattering measurements	31
2.4	Simulation Results	33
2.4.1	Silicon photonics building blocks	33
2.4.1.1	Injection optimized silicon slab waveguide	34
2.4.1.2	Single mode silicon wire waveguide	35
2.4.1.3	Silicon waveguide adiabatic taper	36
2.4.1.4	Silicon wire waveguide bends	37
2.4.2	Plasmonic slot waveguide	38
2.4.2.1	Plasmonic slot waveguide modes	39
2.4.2.2	Coupling of silicon wire waveguide to Plasmonic slot waveguide (PSW)	41
2.4.2.3	Coupling length	42
2.4.3	Plasmonic slot waveguide cavity resonances	44
2.4.3.1	Influence of the cavity length and the coupling strength on the Fabry-Pérot resonance of the PSWC	46
2.4.3.2	Influence of the slot width and the gold thickness on the resonance of the PSWC	48
2.4.3.3	Influence of the slot lateral position with regard to the silicon waveguide	49
2.4.4	Field enhancement in the slot of the PSWC	49
2.4.4.1	Influence of different metals and different cavity lengths on the PSWC resonance	51
2.4.5	Sensitivity to refractive index of the coupled system	52
2.5	Experimental Results	55
2.5.1	Silicon waveguide propagation losses	55
2.5.1.1	Absorption losses in silicon	56
2.5.1.2	Surface scattering losses	57
2.5.1.3	Radiation losses	58
2.5.2	Measurement of the propagation losses	58
2.5.2.1	Cut-back method loss measurement	60
2.5.2.2	Fabry-Pérot resonator losses measurement	62
2.5.2.3	Fourier analysis of the Fabry-Pérot resonator	65
2.5.3	Broadband transmission measurements of the integrated PSWC	68
2.5.4	Far field scattering measurements of the excited PSWC	74
2.5.5	PSWC sensitivity measurement	74
2.6	Future perspectives and developments	77
2.7	Conclusion	78

3	Standing wave integrated Fourier transform spectrometer	81
3.1	Introduction	81
3.1.1	Standing wave integrated Fourier transform spectrometer principle . . .	82
3.1.1.1	Interference fringes in Lippmann SWIFTS	83
3.1.1.2	Ideal nano-sampler scattering cross-section	86
3.1.1.3	Bandwidth and resolution	86
3.1.2	Calibration of the non-ideal SWIFTS	88
3.1.3	The scanning SWIFTS	88
3.2	Objectives	90
3.3	Approach, Methods and tools	91
3.3.1	SWIFTS design	91
3.3.1.1	Single-mode Epocore waveguides	91
3.3.1.2	Design of the Injection optics	92
3.3.1.3	Design of the nano-samplers	93
3.3.1.4	Summary of the designed scanning SWIFTS	94
3.3.2	Fabrication	94
3.3.2.1	Micro-lens fabrication	94
3.3.2.2	Scanning SWIFTS chip fabrication	95
3.3.2.3	Alignment of the of the micro-lenses	98
3.3.3	Experimental set-up	99
3.3.3.1	Optical read-out of the sampled interferogram	99
3.3.3.2	The scanning mechanical setup	100
3.4	Results	102
3.4.1	Calibration light sources	104
3.4.2	The recorded interferogram	105
3.4.3	Post-processing of the interferogram for calibration	106
3.4.3.1	Nano-sampler DC level calibration	106
3.4.3.2	Nano-sampler scattering efficiency calibration	108
3.4.3.3	Correction of the nano-sampler position – Phase matching . . .	109
3.5	Futur perspectives	112
3.6	Conclusion	113
4	Conclusion	115
A	Appendix	117
A.1	Fabrication recipes	117
A.1.1	PECVD SiO ₂ deposition	117
A.1.2	Waveguide dry etching	118
A.1.3	EpoCore and EpoClad photolithography parameters	120
	Bibliography	123
	Acknowledgements	137

Contents

Curriculum Vitae	139
------------------	-----

List of Figures

2.1	Dispersion diagram of a surface plasmon excited at an air-gold interface. The dispersion diagram is showing the surface plasmon can be excited by using an SiO ₂ prism for example.	7
2.2	Conceptual sketch of an optical label-free biosensor	9
2.3	Schematic of the periodic plasmonic slot waveguide cavity (PSWC) sensor design inspired by extraordinary optical transmission (EOT) [1].	15
2.4	Design of the fabricated chips.	19
2.5	Process flow of the fabrication of the PSWC. 1) silicon-on-insulator (SOI) substrate (handle wafer not shown). 2) Deposition of the SiO ₂ spacer by plasma enhanced chemical vapor deposition (PECVD). 3) Spin-coating of ZEP520A e-beam resist. 4) Resist exposition and development. 5) reactive ion etching (RIE) with induced coupled plasma (ICP) etching of the SiO ₂ spacer and the silicon waveguide. 6) O ₂ plasma ashing of the ZEP520A resist and piranha cleaning. 7) Spin-coating of ZEP520A resist. 8) Exposure and development of the resist. 9) Evaporation of titanium seed layer and gold layer. 10) Metal and resist lift-off followed by a piranha cleaning.	20
2.6	Dose test from 40 to 70 $\mu\text{C}/\text{cm}^2$ for five PSWC with different gap sizes exposed on a 70nm thick ZEP520A resist on a silicon substrate. The gap ranges (w_s) from 30 to 70nm from left to right.	23
2.7	scanning electron microscope (SEM) images showing the developed waveguides having all a width of 600nm in the layout for different exposure doses in ZEP520A resist.	24
2.8	Single mode silicon waveguide with SiO ₂ spacer etched with "pseudo Bosch process".	26
2.9	Cross section of the etched waveguides coated with ZEP520A e-beam resist. a) ZEP520A : Anisol 1:2 dilution: Spin-coating at 1000rpm for 60sec with an acceleration of 500rpm/s. b) ZEP520A : Anisol 1:1 dilution: Spin-coating at 1000rpm with an acceleration of 500rpm/s.	27
2.10	PSWC aligned on top of a single mode silicon waveguide.	28
2.11	Picture of the injection setup used to measure the waveguide transmission. . .	29
2.12	Wavelength interrogation method optical setup.	30
2.13	Light management setup of the supercontinuum laser source and fiber injection. .	31
2.14	Far field scattering optical setup.	32

List of Figures

2.15 a) Comparison of injection losses inside a $3\mu\text{m}$ by $0.25\mu\text{m}$ silicon slab waveguide between a butt coupling with a PM1300 fiber having a $9\mu\text{m}$ mode field diameter (MFD) and an end-fire coupling with a polarization maintaining (PM) lensed fiber having a spot size of $2\mu\text{m}$. b) Coupling losses of a $2\mu\text{m}$ spot size lensed fiber versus the lateral size of a rectangular silicon slab waveguide having a $0.25\mu\text{m}$ height.	35
2.16 Dispersion diagram of a silicon wire waveguide of 450nm by 220nm cross-section on top of a $2\mu\text{m}$ thick SiO_2 cladding and outer medium of refractive index of 1, showing the two allowed propagating modes quasi-transverse electric (q-TE) and quasi-transverse magnetic (q-TM) over the desired wavelength bandwidth from 1200nm to 1700nm	36
2.17 Transmission for different taper lengths calculated with the time domain solver of CST Microwave Studio (CST MWS) showing the losses from 1200 to 1700nm . $2\mu\text{m}$ SiO_2 substrate ($n_{\text{SiO}_2}=1.46$), $3\mu\text{m}$ by 220nm silicon slab input waveguide, 450nm by 220nm silicon wire output waveguide. The silicon material properties have been taken from D. E. Aspnes and J. B. Theeten [2]. They include material dispersion which is fitted with a second order polynomial. The top cladding above the waveguide is air.	37
2.18 a) Transmission from 1200nm to 1700nm of 2D silicon waveguides of 450nm width in air having bend radius from 1 to $15\mu\text{m}$. b) $ E $ -field for a $15\mu\text{m}$ radius bend at $\lambda=1.5\mu\text{m}$	39
2.19 Drawing of a typical plasmonic slot waveguide (PSW) with metal thickness of 20nm (t_s), width of 450nm (w) and slot width of 20nm (w_s) lying on top of a silicon dioxide substrate and surrounded by air. The two figure insets show the absolute electric field amplitude at $\lambda = 1500\text{nm}$ of the two propagating modes A_0 and S_0	40
2.20 Dispersion diagram of the PSW symmetric (S_0) and asymmetric (A_0) modes depicted in Fig. 2.19 showing the influence of the slot width reduction on the A_0 slot mode propagation constant.	41
2.21 Dispersion diagram of uncoupled and coupled q-TE mode of the silicon wire waveguide and A_0 PSW mode.	42
2.22 2D E_y -field amplitude component at $\lambda=1500\text{nm}$. a) q-TE mode of the silicon wire waveguide with an SiO_2 top layer (spacer) ($t_s = 40\text{nm}$, $w = 450\text{nm}$). b) Asymmetric mode (A_0) of the PSW with the waveguide core material replaced by SiO_2 ($t_m = 20\text{nm}$). c) Coupled hybrid even mode (H_{TE_0}) of the PSW and the silicon wire waveguide. d) Coupled hybrid odd mode (H_{TE_1}) of the PSW and the silicon wire waveguide.	43
2.23 (a): E_y -field amplitude showing the coupling between the dielectric waveguide and the metallic slot calculated with 3D frequency-domain solver of CST MWS. (b) and (c): E_y -field amplitude of the 2D mode profile at $z = 0$ and $z = 1.78\mu\text{m}$. (d): Transmission of the excited cavity as function of the cavity length at $\lambda = 1500\text{nm}$	44

2.24	Drawing of the hybrid photonic-plasmonic cavity. On top of a single crystal silicon waveguide there is a PSWC which is separated from it by a silicon oxide film. Invariant spatial parameters of this structure are $t_{wg} = 220nm$, $w = 450nm$ and $w_s = 50nm$. Variable spatial parameters of the PSWC are $L = 600nm$, $t_s = 40nm$ and $t_m = 20nm$	45
2.25	Transmission spectra of a PSWC with standard geometrical parameters (see paragraph 2.4.3 on page 44). a) Dependence of the transmission spectra as function of the cavity length (L). b) Dependence of the transmission spectra as function of the spacer thickness (t_s). Both figures exhibit typical Fabry-Pérot resonance peaks.	47
2.26	Transmission spectra of a PSWC with standard geometrical parameters (see paragraph 2.4.3 on page 44). a) Dependence of the transmission spectra as function of the slot width (w_s). b) Dependence of the transmission spectra as function of the gold thickness (t_s). Both figures exhibit typical Fabry-Pérot resonance peaks.	49
2.27	Transmission spectra dependence upon different slot lateral misalignments for a PSWC with standard geometrical parameters (see paragraph 2.4.3 on page 44). A stronger resonance for a 75nm misalignment can be observed.	50
2.28	a) Transmission spectrum compared to the averaged electric field enhancement around a gold PSWC ($t_s = 40nm$, $w = 450nm$, $t_m = 20nm$, $w_s = 50nm$, $L = 600nm$). b) 2D normalized $ E ^2$ -field distribution at half the metal thickness of the plasmonic cavity at resonance frequency.	51
2.29	Real and imaginary parts of the dielectric function of silver [3], gold [3] and silver[4].	52
2.30	a) and b) Transmission spectra for PSWC of 300nm and 600nm length (L) made out of silver, gold and aluminium. c) and d) Averaged electric field amplitude enhancement over a volume including the PSWC.	53
2.31	(a): Bulk sensitivity for silver and gold PSWC of 300 nm length as function of the spacer thickness. (b): Bulk sensitivity for silver, gold and aluminium PSWC of 600 nm length as function of the spacer thickness. (c): Resonance wavelength shift of a 600 nm (L) long gold PSWC as a function of the thickness of a molecular layer of refractive index of 1.4 deposited on it.	54
2.32	Refractive index and absorption coefficient of crystalline silicon at 300°K reproduced from [5].	56
2.33	Typical transmission spectrum acquired by sweeping a tunable laser from 1500-1510nm in 1pm steps. The spectrum shows high contrast Fabry-Pérot fringes. A bad alignment stability is shown here by the DC power (Fourier filtered signal) shown in red which drops over time due to injection misalignment.	59
2.34	Transmission measurement without a chip; from PM lensed fiber to lensed fiber. 60	
2.35	Measurement of the normalized coupling efficiency as function of the PM lensed fiber misalignment (2μm spot size) for a 3μm by 0.22μm silicon slab waveguide covered with a 50nm thick SiO ₂ layer.	61

List of Figures

2.36	Propagation losses of silicon waveguides of 450nm width and 220nm height with and additional 50nm of SiO ₂ deposited by PECVD at $\lambda_0 = 1500\text{nm}$ measured by fringe contrast method. (Chip 34).	64
2.37	Fourier transform of the transmission spectrum of a waveguide with $L_2 = 100\mu\text{m}$. The spectrum is showing the different cavities formed in the waveguide because of the tapers and the bends.	66
2.38	Propagation losses calculated with three different methods: the fringe contrast method, the harmonic amplitude ratio (HAR) of peak 0 and 1 and the HAR of peak 1 and 2.	67
2.39	Normalized transmission measurements in dB of a waveguide (transverse electric (TE) mode) with a $178\mu\text{m}$ long strip waveguide section. The fiber-to-fiber measurement as well as the raw waveguide transmission spectrum is shown for clarity.	68
2.40	Transmittance of chip 41 waveguides (a.) without and (b.) with PSWC. (c.) Δ transmittance between waveguide with and without PSWC.	69
2.41	Normalized transmittance spectra of waveguides having different lengths but all exciting the same PSWC with a spacer thickness (t_s) off 10nm . The transmission spectra have been normalized by the spectra of identical waveguides having no PSWC.	70
2.42	SEM images showing the PSWC on top of each different waveguide of chip 41. .	71
2.43	(a.) shows the raw spectrum measured with the optical spectrum analyzer at the output of the waveguide, once with and once without a PSWC. The standard deviation is shown based on 5 repetitive measurements for which a new alignment of the fibers is done each time. (b.) shows the transmittance of the waveguide with and without the PSWC normalized by the fiber-to-fiber transmission. (c.) shows the transmittance of the PSWC obtained by dividing the transmittance of the curve in (b.) with a PSWC by the one without a PSWC. The curve is exhibiting the plasmonic resonance located at around $\lambda = 1300\text{nm}$. The dashed curve in (c.) is the transmittance obtained by simulation with CST MWS in which the spacer thickness (t_s) was set to 10nm.	72
2.44	Far field scattering of the PSWC compared with the measured transmittance of the PSWC through the waveguide and the CST MWS TD simulation.	75
2.45	Measured transmittance of the PSWC of Chip 41 and waveguide of length $L_2 = 878\mu\text{m}$ in air and in water. Simulation results obtained with the time domain solver of CST MWS are superposed on the measurements.	75
2.46	SEM image of the deformed PSWC after a piranha cleaning. Rapid grain growth of the gold layer occurred due to elevated temperature in the piranha bath. . .	76
3.1	Schematic representations of the Gabor and Lippmann type standing-wave integrated Fourier transform spectrometer (SWIFTS)	83

3.2	Sampled interferogram of an ideal Lippmann SWIFTS described by equation 3.11. $N = 200$, $\Delta x = 10\mu\text{m}$, $\eta = 0.01$ and $\lambda = 750\text{nm}$. The two decaying red curves are the two first terms expressing the loss of intensity due to the nano-sampler scattering.	85
3.3	Amplitude of the measured interference term as function of the nano-sampler scattering cross-section.	87
3.4	Conceptual sketch of the spectrum retrieval from a scanning SWIFTS. On the left, a waveguide sustaining a standing wave is shown for four different mirror positions. The nano-samplers intensity is recorded for each batch of measurements. The data is recombined in a post-processing step to create the interferogram. The raw interferogram is then numerically post-processed to take into account several errors due to fabrication. The interferogram is then Fourier transformed to find the optical spectrum.	89
3.5	Band diagram of an EpoCore waveguide having a width of $3\mu\text{m}$ and a height of $2\mu\text{m}$. 91	
3.6	Electric field amplitude of EpoCore single-mode waveguide at $\lambda = 762.5\text{nm}$ simulated with CST MWS mode solver. $n_{\text{core}} = 1.58$; $n_{\text{clad}} = 1.57$, $n_{\text{eff}} = 1.574$. 92	
3.7	Ray trace with Oslo free educational version of a $245\mu\text{m}$ in diameter micro-lens focusing on the backside of its substrate.	93
3.8	Sketch of the Lippmann SWIFTS configuration with a moving mirror. This allows to increase the sampling frequency of the interferogram, in other terms allow to acquire spectra with larger bandwidth with respect to the static configuration. 94	
3.9	(a) Image of the fabricated photoresist micro-lenses with their backside black photoresist. Epi-illumination. (b) Same image with dia-illumination showing the $10\mu\text{m}$ apertures through the black photoresist positioned in the back focal plane.	95
3.10	Sketch of the different fabrication steps of the waveguide chip of the SWIFTS spectrometer.	96
3.11	Gold nano-samplers fabricated by electron beam lithography (EBL) with aligned EpoCore waveguide on top.	97
3.12	Continuous gold nano-samplers fabricated by EBL with EpoCore waveguide on top. No need for alignment in that case.	97
3.13	SEM image of fabricated EpoCore single-mode waveguide.	98
3.14	Scanning SWIFTS chip ready to be implemented into the mechanical setup with the moving mirror. The images are showing the integration of the micro-lenses onto the facet of the SWIFTS chip.	99
3.15	Image of the complete spectrometer setup including the camera and objective that are imaging the planar nano-cavities located on top of the waveguides. The mirror is driven by a closed-loop piezo actuator.	100
3.16	3D drawing of the chip holder including the scanning mirror driven by a piezo actuator.	101

List of Figures

3.17 Typical image acquired by the SBIG camera showing the sampled interferogram of six adjacent waveguides. The mirror is on the top. We show how we defined the minimal mirror gap (xm_0) and the distance of the first nano-sampler to the waveguide facet (xw_0). The average value of the blue lines is used to calculate the spectrum.	103
3.18 a. Spectrum of the LP785-SF20 laser diode. b. Spectrum of the LP660-SF60 laser diode. The resolution of the spectrum is 0.01nm.).	104
3.19 a. Spectrum of tunable external-cavity laser diode (SDL-8630). b. Spectrum of the HeNe laser. The resolution of the spectrum is 0.01nm.	105
3.20 Raw interferogram of the first 64 nano-samplers without any post-processing for 871 mirror steps of 20nm at $\lambda = 789\text{nm}$. Each different color represents another nano-sampler.	106
3.21 Example of a complete interferogram showed in 2 dimension for 871 mirror steps of 20nm each at $\lambda = 789\text{nm}$. The x-axis represents the optical path difference (OPD) induced by the first 64 nanosamplers. The y-axis represents the OPD induced by the mirror.	107
3.22 Interferogram of the 5 first nano-samplers on a total of 64. On the top is the raw data. In the middle is the DC corrected data. On the bottom is the RMS corrected data.	108
3.23 Complete interferogram without overlapping OPD samples ont the top. Phase matched interferogram by zero-padding on the bottom.	109
3.24 Spectrum of the external cavity laser diode at $\lambda = 789\text{nm}$. The spectrum is obtained by Fourier transform of the non-zero padded interferogram.	110
3.25 Spectrum of the external cavity laser diode at $\lambda = 789\text{nm}$. The spectrum is obtained by Fourier transform of the zero padded interferogram. Less leakage can be seen.	111

List of Tables

3.1	EpoCore waveguide parameters.	92
A.1	PECVD SiO ₂ depositon process parameters	117
A.2	O ₂ plasma descum recipe to clean resist residues after development of the ZEP520A118	
A.3	SiO ₂ etch process parameters on STS Multiplex ICP etcher	118
A.4	Pseudo Bosch process parameters on STS Multiplex ICP etcher	119
A.5	Recipe given by Microresist Technology for layer of EpoClad_5 and EpoCore_2.	121

Acronyms

ATR attenuated total reflectance. 10

CCD charge-coupled device. 31, 99

CMOS complementary metal oxide semi-conductor. 18, 21

CSEM Swiss Center for Electronics and Microtechnology. 2, 82

CST MWS CST Microwave Studio. x, xii, xiii, 17, 18, 33, 37, 36, 38, 39, 42, 43, 46, 63, 71, 73, 74, 92

DFB distributed feedback laser. 104

DUT device under test. 27

EBL electron beam lithography. xiii, 21, 22, 23, 24, 25, 26, 95, 97, 95, 98

EM electromagnetic. 5, 12, 17, 18, 36

EMPA Swiss Federal Laboratories for Materials Science and Technology. 2, 82, 95

EOT extraordinary optical transmission. ix, 15

EPFL Ecole Polytechnique Fédérale de Lausanne. 18

ESA European Spatial Agency. 2, 81, 82

EUVL extreme ultraviolet lithography. 21

FDTD finite-difference time-domain. 17

FFT fast Fourier transform. 102, 109

FITD finite-integration time-domain. 17

FOM figure of merit. 55

FWHM full width at half maximum. 55

GFP green fluorescent protein. 8

Acronyms

HAR harmonic amplitude ratio. xii, 66

HeNe helium-neon. 104

ICP induced coupled plasma. ix, 19, 22, 25

IPA Isopropyl alcohol. 22, 95

IR infrared. 81

LSPR localized surface plasmon resonance. 12, 13, 55

MFD mode field diameter. ix, 34, 35, 92

Mhipis Miniature High Performance Imaging Spectrometer for Remote Sensing. 2, 82

MIBK Methyl isobutyl ketone. 22, 95

MIM metal-insulator-metal. 12, 13, 39

MZI Mach-Zehnder interferometer. 11

NA numerical aperture. 34

NASA National Aeronautics and Space Administration. 81

NFFT Nonequispaced fast Fourier transform. 109

NIR near infrared. 31, 67

NMP n-méthyl-2-pyrrolidone. 22

OPD optical path difference. xiv, 45, 51, 66, 83, 102, 106, 108, 109

OPICS Optical planar integrated cavity sensors. 2

OPT Optics & Photonics Technology. 18

PC polarization controller. 29

PECVD plasma enhanced chemical vapor deposition. ix, xi, 19, 21, 64, 68

PIC photonic integrated circuit. 12

PM polarization maintaining. ix, xi, 29, 30, 31, 34, 35, 58, 59, 60, 59, 61

PML perfectly matched layer. 36, 46

PMMA Poly(methyl methacrylate). 95

- PPSWC** periodic plasmonic slot waveguide cavity. 5
- PSW** plasmonic slot waveguide. x, 12, 38, 39, 41, 42, 43, 46, 47, 48, 51, 78
- PSWC** plasmonic slot waveguide cavity. ix, x, xi, xii, 5, 15, 17, 18, 19, 21, 22, 23, 25, 26, 27, 31, 33, 38, 43, 44, 45, 46, 47, 48, 49, 50, 51, 52, 54, 55, 69, 71, 69, 71, 73, 74, 76, 74, 77, 78, 79
- Q-factor** quality factor. 11, 45, 46, 48, 51, 54
- q-TM** quasi-transverse magnetic. x, 35, 36, 44, 78, 91
- q-TE** quasi-transverse electric. x, 12, 35, 36, 35, 36, 38, 41, 42, 43, 44, 48, 58, 69, 74, 78, 91
- RIE** reactive ion etching. ix, 19, 22, 25
- RIU** refractive index unit. 5, 54, 55, 78
- RMS** root mean square. 108
- SEM** scanning electron microscope. ix, xii, xiii, 24, 71, 76, 74, 97
- SERS** surface enhanced Raman spectroscopy. 12
- SM** single-mode. 5, 29, 31
- SNSF** Swiss National Science Foundation. 2
- SOI** silicon-on-insulator. ix, 19, 33, 36, 57, 58, 77
- SP** surface plasmon. 12, 38
- SPP** surface plasmon polariton. 5, 11, 12, 51
- SPR** surface plasmon resonance. 1, 2, 8, 11, 12
- SWIFTS** standing-wave integrated Fourier transform spectrometer. xii, xiii, 2, 81, 82, 83, 84, 85, 86, 87, 88, 90, 91, 92, 94, 95, 98, 99, 98, 100, 102, 103, 106, 112, 113
- TE** transverse electric. xii, 29, 31, 38, 59, 68
- TIR** total internal reflection. 10
- TM** transverse magnetic. 8, 29, 31, 38, 59
- TRP** Technological Research Programme. 2, 82
- UV** ultraviolet. 81, 95, 97, 98, 100
- ZPD** zero path difference. 82

1 Introduction

Nowadays, the progresses made in the field of nano-technology allow the fabrication of structures that are smaller than the micrometer with very high accuracy. It is now possible to chose their shape, their material and their exact position. In the domain of optics, the ability to perturb the light with nano-structures that are smaller than the wavelength opens many new interesting research topics. Especially in the domain of optical sensing, the ability to strongly confine the light is of great importance where the interaction between light and matter needs to be increased. Moreover, if we want to probe the local intensity of a light wave, we need to do it on a sub-wavelength scale with some nano-structures.

That apart, another domain which will play an important role in tomorrow's optical sensors is the technological advances done in semi-conductor integrated photonics. They are driven by the market of consumer electronics and opening new perspectives for cheap integrated portable optical sensors. This integration into small chips will accelerate the miniaturization of optical sensors which is one of today's biggest challenge.

This thesis investigates two different applications of sub-wavelength nano-structures excited by integrated platforms. The first study focuses on biosensing through the use of plasmonic nano-structures. The second study uses nano-structures to sample standing waves inside a waveguide with the purpose of creating a miniaturized spectrometer. Both subjects present an innovative application of sub-wavelength nano-structures and distinguish themselves from common studies by relying on the integrated waveguides for their excitation. While sharing the same fundamental mechanism, both studies bring out specific problematic and challenges.

As mentioned, our first study focused on biosensing. Today's most effective biosensors are based on optical detection methods. In the field of bio-sensing, scientists are interested in the detection of a biological component (e.g. protein) present in an analyte which is in the form of a liquid. Most of optical biosensor are sensitive to changes in refractive index upon a specific surface of the sensor. The detection of the biological component is done through a bio-linker which is grafted on the sensing surface preliminary to the detection. The bio-linker will

recognize the biological component under study present in the analyte and specifically bind to it. In protein sensing for example, this bio-linker is most often an anti-body. This is how the optical sensor will be able to specifically detect a biological component present in an analyte. In the case of an optical biosensor based on surface plasmon resonance (SPR), its sensitivity to changes in refractive index is not strictly limited to its sensing surface. An evanescent field, having its highest intensity at the surface, exponentially decays in the direction normal to the surface. The sensitivity of the SPR sensor is proportional to the strength of the interaction of this evanescent field with the analyte. Therefore, this type of optical sensors are also sensitive to changes of refractive index which are occurring further away from the surface. These unwanted interactions will result in some detection noise. Moreover, the detection of the biological component is done on large surfaces, which makes it difficult to detect single biological components present in an analyte at high concentrations.

This first study was part of a larger project ¹ aiming at developing optical planar integrated cavity sensors. It focuses specifically on the development of a integrated plasmonic slot waveguide cavity sensor excited by a single-mode silicon strip waveguide realized on an silicon-on-oxide platform. This sensor distinguishes itself by the nature of its plasmonic resonance. On one hand the plasmonic slot waveguide cavity sensor has the advantage of having an evanescent field which is, unlike the SPR sensor, in the plane of the sensing surface. On the other hand, the sub-micrometer size of the cavity could be beneficial to the detection of single biological components at high concentrations. These two benefits are combined with its potential high multiplexing capabilities resulting from its integrated implementation.

Our second study investigated the field of miniaturized spectrometers. A spectrometer is an apparatus to measure the frequency components of light. Different types of spectrometers have been developed through the years. The two most common ones are: the grating spectrometers which is based on the diffraction of light and the Fourier transform spectrometer which is based on the measurement a light wave in its spatial-domain. Common Fourier transform spectrometers which are using a free space Michelson interferometer to induce an optical path difference by scanning the mirror of one of the arms of the interferometer are large and bulky. Recently a new type of Fourier transform spectrometer called SWIFTS has been presented. They are based on the same principle of measuring the light wave in the space-domain but do not have any moving part. They rely on the measurement of the spatial intensity distribution of a standing-wave created inside an integrated waveguide. The standing-wave is probed at several positions by some nano-structures present on top of the waveguide which locally extract a small part of the light to the free space. These type of spectrometers suffer from a limited bandwidth because the latter is proportional to the spatial sampling frequency of those nano-structures.

This second study was part of a large project ² aiming at circumventing the limits imposed by

¹Optical planar integrated cavity sensors (OPICS) funded by the Swiss National Science Foundation (SNSF). Realized through the work of three PhD Students: Dr. Qing Tan, Dr. Armando Cosentino and myself.

²Miniature High Performance Imaging Spectrometer for Remote Sensing (Mhipis) project which was part of

a standard SWIFTS. Moreover it paved the way to the foreseen possibility to used the SWIFTS technology to create an imaging spectrometer.

1.1 Thesis structure

After this introduction, a second chapter will focus exclusively on the plasmonic slot waveguide cavity sensor. After introducing the basic theoretical concepts and reviewing the actual state of the art, we will present the obtained simulation results of the sensor. We will follow with the description of the method of fabrication of the sensor and the explanation the used optical characterization setup. Finally, we will disclose the characterization and measurement of the different component of the sensor as well as the measurement of refractive index sensing.

The third chapter of this manuscript will treat the standing-wave integrated Fourier transform spectrometer. It will as well introduce the basic theoretical concepts and reviewing the actual state of the art. After that, the fabrication and the assembly of the spectrometer will be described. It will be followed by the presentation of the obtained measurements including the detailed description of the necessary post-processing calibration of the raw measurements.

A final chapter will conclude the realized work and the potential of nano-structures for optical sensing.

2 Integrated and localized plasmonic refractive index sensor

This chapter is a partial adaptation of the Optics Express journal article entitled "Vertically coupled plasmonic slot waveguide cavity for localized biosensing applications" by G. Osowiecki et al. [6].

2.1 Introduction

This chapter of the thesis deals with the study of plasmonic nano-structures excited by an integrated single-mode silicon waveguide. It focuses on the fundamental understanding of the behavior of the electromagnetic (EM) field inside these plasmonic cavities. The fabrication process of the different designs and the application to sensing are parts of the project.

The work of two previous PhD students Qing Tan and Armando Cosention demonstrated the simulation, fabrication and characterization of periodic plasmonic slot waveguide cavity (PPSWC) excited by a multimode slab waveguide. The device has potential applications as a refractive index sensor in the near-infrared and obtained a sensitivity of 730 nm per refractive index unit (RIU). This chapter is the continuation of the project in which we will study the implementation of a plasmonic slot waveguide cavity (PSWC) on top of a single-mode (SM) silicon waveguide. The EM field will be strongly localized inside the slot of the PSWC, and therefore a stronger interaction with the mode of the waveguide is expected. Although the sensitivity is theoretically reduced to 370 nm/RIU for a single PSWC, the sensing volume decreases by more than an order of magnitude and the detection limit is increased by the higher contrast of the resonance dip in the spectrum.

2.1.1 Plasmon and surface plasmon

To understand what is a plasmon and a surface plasmon polariton (SPP) we need to start by briefly explaining the nature of the electronic band structure of a material. The electrons of a single atom in a box have discrete levels of energy and they occupy different atomic orbitals. If we put more atoms of the same kind in this box, more discrete levels of energy are appearing

until an energy band is formed. In metals, the atoms share some of their electrons and the energy band is filled from the bottom. As long as the energy band is not completely filled, the electrons can move easily and this allows metals to conduct electricity. For isolators, the highest energy band which is called the valence band is completely filled and the energy gap to reach the empty upper energy band is large. This energy gap is called the band gap. For semi-conductors, the band gap is small enough to be crossed by some electrons which have received additional energy, for example from heat. This is why we called these materials "semi-conductor". Now let's go back to the metals and their free electrons which can move easily. We can treat these free electrons like a liquid having a certain density: the electron density which is about 10^{23} cm^{-3} . This electron liquid is called a plasma. A plasmon is a longitudinal plasma density fluctuation which can travel through the metal. Its energy is given by $\hbar\omega_p = \hbar\sqrt{4\pi ne^2/m_0}$, where ω_p is the plasma frequency; n is the electron density; e is the charge and m_0 is the mass of an electron [7, 8, 9]. A special kind of plasmon is the SPP [10, 11, 12]. As its name suggests, the SPP is a wave bound to the interface between a metal and a dielectric material which is excited by an external EM field. In the metal, the wave is sustained by the change in electron density and in the dielectric medium the wave is sustained by the change of the EM field. It has its maximum electric field intensity at the interface and it exponentially decays perpendicular to it. The dispersion of a surface plasmon is given by equation 2.1 and its complete derivation can be found in [13].

$$k_x = \frac{\omega}{c} \left(\frac{\epsilon_1 \epsilon_2}{\epsilon_1 + \epsilon_2} \right)^{\frac{1}{2}} \quad (2.1)$$

Where $k_x = k'_x + i k''_x$ is the complex wave vector, $\epsilon_1 = \epsilon'_1 + i \epsilon''_1$ is the complex dielectric constant of the metal and ϵ_2 is the complex dielectric constant of the surrounding dielectric material which is assumed here to be real. The real part of the complex wave vector, which is also called the propagation constant (β), is given by equation 2.2. The imaginary part k''_x of the wave vector is given by equation 2.3. It describes the internal absorption and is also called the attenuation constant (α).

$$k'_x = \frac{\omega}{c} \left(\frac{\epsilon'_1 \epsilon_2}{\epsilon'_1 + \epsilon_2} \right)^{\frac{1}{2}} \quad (2.2)$$

$$k''_x = \frac{\omega}{c} \left(\frac{\epsilon'_1 \epsilon_2}{\epsilon'_1 + \epsilon_2} \right)^{\frac{3}{2}} \frac{\epsilon''_1}{2(\epsilon'_1)^2} \quad (2.3)$$

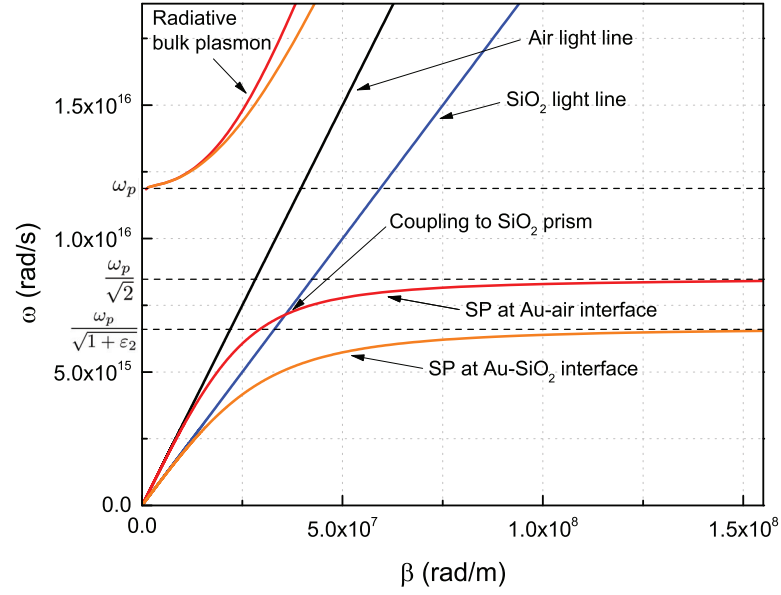


Figure 2.1 – Dispersion diagram of a surface plasmon excited at an air-gold interface. The dispersion diagram is showing the surface plasmon can be excited by using an SiO₂ prism for example.

The propagation length (intensity decreases to $1/e$) of a surface plasmon is inversely proportional to the imaginary part of the wave vector k_x'' as given by equation 2.4. It is typically a couple of tens of micrometers in the visible and can increase to a couple of hundreds of micrometers in the near infrared. It is interesting to note that on very small scales like today microelectronic chips these propagation length become relatively very large. This is why plasmons are promising candidates for future interconnects in microelectronic chips. We will discuss this topic in detail later in this section.

$$L_{sp} = (2k_x'')^{-1} \quad (2.4)$$

In Fig. 2.1, we show the dispersion diagram of a surface plasmon traveling along a gold-air interface. Its momentum is always larger than the light line of air, therefore the surface plasmon is non-radiative. For large β , the frequency value approaches a limit ω_{sp} which is given by equation 2.5. The latter can be found by replacing ϵ_1 by the free electron dielectric function $\epsilon(\omega) = 1 - \left(\frac{\omega_p}{\omega}\right)^2$ in equation 2.1.

$$\omega_{sp} = \frac{\omega_p}{\sqrt{1 + \epsilon_2}} \quad (2.5)$$

Surface plasmons can be excited by electrons [14] or by a momentum matched photon having a transverse magnetic (TM) field. In Fig. 2.1, we show the light line of SiO₂ which is crossing the dispersion line of the surface plasmon. At this intersection the photons are momentum matched and coupling is possible. This is often realized either with a grating [15] or with a prism. For the prism coupling two standard methods, commonly called Otto or Kretschmann configurations, can be used [16, 17].

2.1.2 State-of-the-art biosensors

Nowadays in biosensing applications most detection techniques which are used for cells, proteins or single-molecules are optical. These detection techniques are divided in two main branches: the labelled and the label-free techniques [18].

2.1.2.1 Labelled molecule detection

For the labelled detection techniques, most often fluorescent labels are grafted on the observed specimen. The most common one is the green fluorescent protein (GFP) which has an emission peak at 509nm when excited by wavelength of 395nm (major excitation peak) or 475nm (minor one). The strength of these fluorescent techniques is the high resolution of labeled molecules as well as their ability to be used inside living cells with low photo-toxicity. Fluorescent microscopy is able to resolve labelled single molecule (<10nm) which is way smaller than the diffraction limit of classical optical microscopes. Despite this extremely low detection limit, fluorescent based detection is suffering from the difficult labelling process which is not suited for high throughput measurements. Moreover the behaviour of biomolecules may be altered by the labels. The labels also suffer from photo-bleaching, which means that their fluorescent emission decays over time. When the concentration of labels is too high, quenching of the labels occur. Which means that labels that are too close to each others are suffering from cancellation in fluorescent emission. This is one of the reasons why label-free optical detection techniques have been widely developed these last decades in parallel with the labeled techniques.

2.1.2.2 Label free molecule detection

In label-free detection techniques, the biomolecules are detected in their natural form. Generally these detection techniques allow a quantitative and a kinetic measurement of molecular

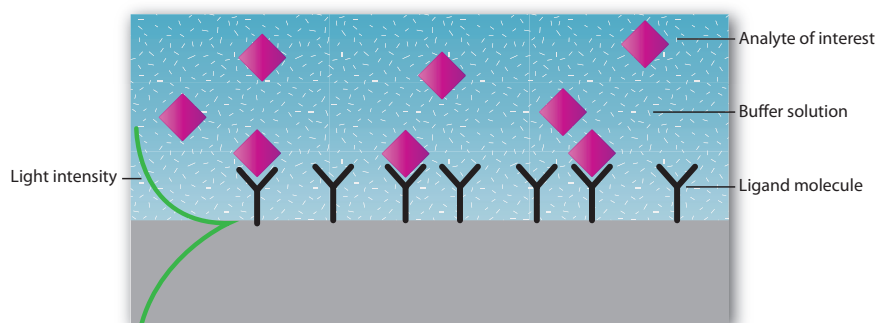


Figure 2.2 – Conceptual sketch of an optical label-free biosensor.

interaction. These sensors are measuring refractive index changes induced by molecular interaction. As the molecular interaction only happens at the sensor surface and not in the bulk of the liquid, the detection signal does not scale down with the sample volume. Most commercial label-free biosensors belong to the class of the direct immunosensors. As explained in [19], "this class of biosensor is based on selective bioaffinity interactions between an antibody and a specific compound, or antigen, or a closely related group of antigens". The antibodies strength enables the possibility to bind to the analyte of interest. Therefore, if the sensing surface is functionalized with ligand molecules and the analyte of interest binds to this surface, a layer of different refractive index will be attached to the proximity of the sensing surface inducing in a perturbation in the optical signal (Figure 2.2). Several different optical techniques are used to take advantage of this optical signal perturbation, like surface plasmon resonance (SPR) or distributed Bragg gratings, photonic crystals or ring resonators to cite only a few. An interesting article comparing commercially available sensors is written by M. Cooper [20] and an article about label free detection trends was written by J. Comley [21]. In Comley's article, we could find some interesting numbers about the requirements of today's label-free sensors. The current limitations of such sensors are the sensitivity and the throughput. They should be able to detect the binding of small molecular weight ligand of typically 200-300 daltons (Da) at a surface mass detection limit of $<5\text{pg/mm}^2$ and at 10^{-9}M concentration in the assay buffer. As reported in Comley's article, the needed throughput of such sensors is nowadays about 5000 measurements per hour which can be achieved by multiplexing the measurement on microplates having several hundreds of wells. Moreover, all this needs to be achieved at a certain cost of less than \$0.2 per measurement.

2.1.2.3 Single molecule sensing with labeled and non labeled techniques

Molecular interactions is generally described on a single molecule basis in chemistry. But these interactions where for a long time only observed on an ensemble of molecules. The first experiments to detect single molecules where started four decades ago. The detection of isolated single molecules has been successfully proven over three decades ago. Some successful methods involved in the detection of single molecules were for example the single-

ion-channel recording with patch-clamp technique [22], the visualization of single molecules with the scanning tunneling microscope [23], or more recently the fluorescence microscopy techniques like confocal fluorescent microscopy [24], stimulated-emission-depletion (STED) microscopy [25] or stochastic optical reconstruction microscopy (STORM) [26, 27].

On one hand, the detection of labeled single molecules by confocal fluorescence microscopy is limited by the concentration of analyte. Since the sensing volume is limited by the diffraction limit, a very low concentration of analyte needs to be used so that the probability of having multiple molecules in this large sensing volume is very low. Some techniques using nanofluidic systems to reduce the sensing volume have demonstrated to be useful in confocal fluorescent microscopy at higher concentrations.

In label-free single molecule detection, the change of refractive index induced by a single molecule can be detected. This has been achieved by using high quality resonators like whispering gallery modes [28, 29]. The resonance frequency is shifted every time a molecule is attaching to the surface of the resonator. In that case, the analyte concentration should be low enough so that the molecules attaches one at a time to the resonator. For these high quality factor whispering gallery modes resonators this concentration is far below the concentration of proteins found inside a living cell for example. If we want to work at higher concentration one should reduce the sensing volume. Decreasing the size of the sensing volume to attoliter volumes is possible with resonating plasmonic cavities [30]. These plasmonic cavities are of great interest for single molecule bio-molecular sensing, especially when it comes to breaking the high concentration limit of optical single molecule detection [31]. Recent work showed the possibility to use plasmonic cavities in order to realize label free single molecule detection [32]. This research field is still very new and it is important to understand the limits encountered by the bio-sensing community to focus on their needs.

2.1.2.4 Review of different types of bio-sensors

In the next paragraphs, well-known label-free optical biosensor architectures will be reviewed to give an overview on what the research has been focused on these last decades in this field. They all rely on the same change in refractive index induced by the binding of the analyte of interest to the fixed antibodies lying on the sensing surface.

Attenuated total reflectance absorption sensors Attenuated total reflectance (ATR) absorption sensors can be found in different forms like prisms, slabs, or waveguides. Evanescent field waveguide sensors [33, 34] were developed in the eighties when fibre-optic technology became affordable. These sensors are based on ATR [35]. When total internal reflection (TIR) occurs at the boundary between two materials of different refractive indices, an evanescent tail of the optical wave is located in the low index material and decays exponentially in the direction normal to the interface [36]. If the molecules adsorbed onto the surface absorbs the incoming light (for example in the mid-infrared wavelength range), the output signal intensity

decreases. As a general rule, sensitivity can be increased by enhancing the interaction length of light with the thin layer of adsorbed biomolecules. This has been done for those sensors by increasing the waveguide length in contact with the analyte [37].

Interferometers based sensors One can detect the change of the modal effective index induced by the adsorbed layer resulting in a phase change of the propagating light. This has been showed by using a silicon based integrated Mach-Zehnder interferometer (MZI) at a wavelength of 1.5 μ m [38, 39]. Other types of interferometer like Young's interferometer [40], Hartman interferometer [41], Michelson interferometer [42] were also integrated as label-free optical biosensors. They could successfully measure the protein binding on the functionalized surface of one arm of the interferometer [43].

Micro-ring resonator based sensors An emerging label-free biosensor technology is the optical micro-ring resonators [44, 45, 46, 47, 48]. Compared to the interferometric sensors, the sensitivity is no longer a function of the physical length of the sensor but rather the number of revolutions that the light is making inside the ring shaped cavity characterized by the quality factor (Q-factor) of the resonator. The effective index change of the resonating mode inside the micro-ring resonator is dependent of the amount of biomolecule adsorbed on its surface and is directly proportional to the resonant wavelength shift. Therefore a quantitative and kinetic measurement of the molecular binding can be measured. One advantage of the micro-ring resonator is its high quality factor resonance which is able to detect very small changes in refractive index. However, they suffer from external temperature fluctuations resulting in small fluctuations of the resonant mode spectral position.

Surface plasmon resonance (SPR) sensors The most versatile sensors, also used in commercial apparatuses, are SPR sensors. A nice review about these SPR sensors has been written by Homola [49]. These sensors are based on the excitation of a SPP. The term resonance corresponds to the achieved coupling of a SPP on the metallic surface of the sensor. The working principle of the mentioned sensors is to track the coupling conditions of the SPP. The coupling condition is perturbed by the absorption of the molecules onto the sensing surface. This change of coupling condition is very sensitive to any perturbation on the surface. This is because of the nature of the SPP which is a surface wave having its maximum of field at the interface itself. These sensors are easily fabricated and operated which explains also why this type of sensor succeeded in a fast transition to the commercial application. Remarkable effort has been put into providing a higher throughput by multiplexing the detection process, mainly by using microfluidic systems [50, 51]. A lot of different approaches have been tried to reduce the size of the SPR sensor, to make cheaper sensors or to make a more localized sensors like the waveguide based SPR [52]. A lot of work is also done on the surface modification and functionalization [53]. The main problem of this type of sensor is the extension of the evanescent tail of the SPP into the buffer solution. The evanescent tail can also be perturbed

by molecules which are in the solution and should not bind on the sensor surface. This contributes to the measurement and it is decreasing the signal to noise ratio. Ideally we would like to only measure the perturbation of the layer of adsorbed molecules onto the surface.

Localized SPR sensors It is important to point out other very interesting properties that surface plasmons (SPs) have. Like their ability to highly confine and guide the light in volumes smaller than the diffraction limit [54]. Thanks to these properties, recent scientific interest in SPP optoelectronics has emerged [55]. Also a whole new research field was created about enhanced detection of small molecules and surface enhanced Raman spectroscopy (SERS) by localized surface plasmon resonance (LSPR). Indeed, it has been shown that for metal films of high roughness, a strong local field enhancement was observed. This one results from the excitation of localized modes due to the surface roughness [56]. The LSPR can also be found in the bulk of metallic nanoparticles and is supported by collective oscillation of electrons [57, 58, 59]. The resonance wavelength shift of these metallic nano-particles due to the adsorption of molecules on their surface can be used as a bio-sensor. For the detection of small molecules, LSPR can excel SPR because it is more sensitive to changes in refractive index close to its surface [60]. LSPR generally provides smaller bulk sensitivity values compared to SPR but the small detection volume of the LSPR enables an easier differentiation between bulk and surface refractive index changes and thus promotes a better detection of small molecules with a reduced noise from the bulk [61]. Most of the LSPR studies are focusing on different 3D shapes of metallic nano-particles or nano-particle clusters fabricated by a bottom-up technique [62]. Another well known field which is overlapping the LSPR field is the field of plasmonic nano-antennas. The main difference here is that the aim of nano-antennas is to localize the free space radiation to a point in space (receiver configuration) or to let a localized source much better couple to far field radiation (emitter configuration). Most of the studies are exciting these nano-antennas with a plane wave and are looking at the radiation pattern and the spectrum. The geometry of these structures is very important to shape the radiation pattern of the nano-antenna [63]. These nano-antennas are fabricated by top-down techniques which is enabling a larger freedom in the shape of the nano-structure. This is why most of these plasmonic antennas are fabricated in 2D. Thanks to the freedom of fabricating different 2D shapes, a special resonance can be created by coupling different LSPR modes like for example Fano resonances [64]. These are created by putting together different metallic cavities of different shapes close together [65]. These coupled LSPR system having stronger resonances are generating strong localized field enhancement and are therefore more sensitive when they are used as a bio-sensors [66].

Plasmonic waveguides Back in 1969, Economou [67] was interested in the light propagation inside an insulating film located between two semi-infinite metal films. He derived the analytical solutions for different types of surface plasmon based multilayered films. These SPs have the specificity to have no cut-off wavelength under the surface plasmon frequency (ω_{sp}) of the metal. Different plasmonic waveguide designs based on these multilayered

films have been investigated with the aim to decrease their propagation losses (propagation length of a few tens of micrometers in the near infrared). One of the most studied plasmonic waveguide is the plasmonic slot waveguide (PSW) which is a narrow dielectric slot surrounded by metal. This comes from the fact that a PSW allows an easy integration in wafer-level micro-fabrication thanks to its planar geometry [68]. metal-insulator-metal (MIM) structures like PSWs show deep sub-wavelength localization and enhancement of EM fields [69]. More recent studies of the modal characteristics of PSWs for semi-infinite MIM films have been published [70, 71] as well as for truncated MIM films [72]. The PSWs support a fundamental quasi-transverse electric (q-TE) mode if the slot width is small enough compared to the wavelength [73]. This sudden resurgence of interest in PSW appeared because of the actual high-frequency limitations of electronic integrated circuits. The actual micro-processors are limited by an interconnect bottleneck of data transmission between the components which is limiting their performance. This interconnect bottleneck is a result of the miniaturization of the integrated circuits minimum feature size. Because of this downsizing, wires used to route the data are suffering from parasitic capacitance and signal propagation delay. Alternatives like photonic integrated circuit (PIC) are under consideration to tackle the data transmission problem since they are able to work at higher frequencies at the speed of light. Nowadays, PIC are based on relatively large silicon photonic wire waveguides (500nm). Moore's Law, like in electronic integrated circuits, imply a higher integration of PIC. Therefore, a downscaling of the silicon waveguides width is required. Photonic silicon wire waveguides can not endlessly confine optical modes in smaller volumes because of increasing propagation losses due to the loss of mode confinement. It has been shown that plasmonic waveguides are major candidates for future on-chip interconnects which should be used in parallel of silicon waveguides as they allow a dense integration with short coupling length to silicon waveguides [74, 75].

Conclusion of the literature review Most LSPR bio sensing experiments which are based on the excitation of metallic nano-particles or plasmonic nano-antennas of specific shapes are done on an ensemble of cavities by an out-off plane excitation. Here we want to point out the limitations of an out-off plane excitation of those plasmonic cavities especially if we want to spatially localize the measurement. The response of a single of those nano-particles excited with an out-off plane focused beam of light is very weak. Therefore, the average response of multiples metallic nano-particles is usually measured instead. This increases the signal to noise ration of the sensor. In the case we want spatially localize the measurement, we should excite a single plasmonic cavity by an out-off plane illumination. In that case, those metallic cavities need to be isolated on the surface. The emitted light from the nano-structure is then collected and measured in the far-field. The problem with that kind of excitation is that the plasmonic cavity can be smaller than the diffraction limited excitation spot and part of the focused excitation light will in that case not interact with the cavity but still be detected in the far-field. Moreover, some resonances cannot be excited by an out-off plane illumination, the modes of these cavities are called "dark" modes. These limitations led us investigate the integrated excitation of this type of plasmonic cavities.

We think that the integrated excitation of a truncated plasmonic waveguide acting like a resonant cavity would be more flexible [76]. These resonant plasmonic waveguide based sensors enable a significant improvement of highly multiplexed detection on an integrated silicon platform [77, 1]. Different resonating plasmonic cavities based on the MIM architecture were realized [78, 79]. A few articles were published in this unexplored and promising research field [80, 81]. In 2013, Bruck and Muskens published a paper about plasmonic nano-antennas on top of silicon waveguides playing the role of coherent perfect absorbers for modulators and all-optical switches [82]. Peyskens and al. recently published an article about the excitation of rod, gap and bow-tie plasmonic antennas excited by an integrated waveguide [83]. The scattering of a plasmonic nano-antenna embedded in a silicon waveguide has been studied by Castro-Lopez et al. [84]. Most of the actual studies of that kind of structures is focusing on applications related to photonics integrated circuits like switches, polarization controllers, filters etc. Therefore this work will be dedicated to the investigation of an integrated excitation of a plasmonic cavity used as an on-chip biosensor.

2.2 Objectives

In the present work, we want to go one step further, and create an integrated biosensor which should be compact and low cost. The former PhD students Qing Tan and Armando Cosentino have studied periodic plasmonic slot waveguide cavities excited on chip by a slab waveguide in their thesis [85, 86]. The idea behind this study was inspired by the work of Ebbesen [87] who measured an extraordinary optical transmission (EOT) through a metallic array of sub-wavelength holes. At that time, different theories were trying to explain this phenomenon. Today, we know that it is due to resonances of light coupling to surface plasmons [88]. It has been shown that the EOT through nano-hole arrays concentrate light in small volumes and that it can be used for biosensing [89]. The integration of a sensor on a chip implies that the whole sensor has to be projected in 2D on the chip. When a 2D metallic sub-wavelength hole array is projected onto a 2D surface, it becomes a metallic slit array. And the free space illumination of that hole array then becomes light guided in a waveguide. This led to the design of an integrated sensor based on the waveguide excitation of a periodic plasmonic slot waveguide cavity which is shown in Fig. 2.3(a). It has been demonstrated in the work of Qing Tan and Armando Cosentino [1, 77] that this on chip integration was successful and could be used as a refractive index sensor.

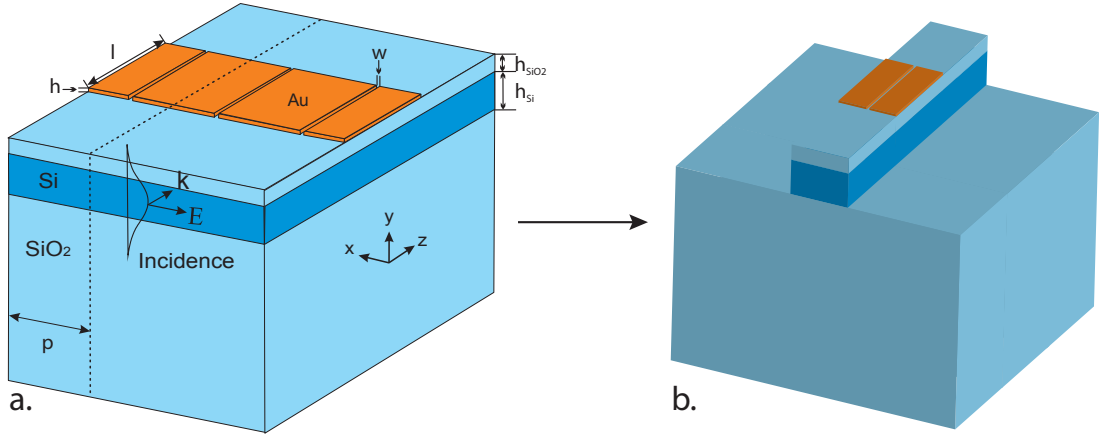


Figure 2.3 – Schematic of the periodic plasmonic slot waveguide cavity (PSWC) sensor design inspired by EOT [1].

As an extension of the previous work of Qing Tan and Armando Cosentino, the aim of the following research is to improve the localization of the measurement of refractive index changes. If the sensor interaction volume can be reduced sufficiently without losing its sensitivity, it would become possible to detect the binding of single molecules. Moreover, it would be possible to densely multiplex the sensor on a 2D surface and extract individual localized measurements of refractive index changes. To this end, our plan was to excite a single plasmonic slot waveguide cavity with a smaller waveguide as shown in Fig. 2.3(b). The lateral field confinement would then be reduced to its maximum. The limit of lateral size reduction of the silicon waveguide is determined by its propagation characteristics. The waveguide

mode confinement needs to be high enough to avoid that its propagation losses become too important. On one hand, the waveguide needs to keep its single mode behaviour over the wanted bandwidth. On the other hand, the single plasmonic slot should be as narrow as possible and all the light should be localized in it. The plasmonic slot resonance should still be excited. This also involves that it should still be possible to couple the light from the waveguide to the single plasmonic slot.

2.3 Approach, Methods and tools

2.3.1 Simulation

The majority of the simulation done in this chapter of the thesis are realized with the commercial software CST Microwave Studio (CST MWS). CST MWS is implemented with several different solvers. Two of them have been used in this work: the "transient solver" and the "frequency domain solver" [90]. In the next sections we will quickly explain the characteristics of both solvers. All the simulations of the plasmonic slot waveguide cavity (PSWC) have been realized in 3D.

2.3.1.1 Transient solver

The transient solver of CST MWS is a general purpose 3D electromagnetic (EM) simulator in the time domain. The transient solver is based on the finite-integration time-domain (FITD) method. This method has been developed by T. Weiland in 1977 [91, 92]. It is derived from the well known finite-difference time-domain (FDTD) method developed by Kane S. Yee in 1966 [93]. Instead of using the differential form of Maxwell's equations it uses the integral form of Maxwell's equations. The main advantage of this method is its compatibility with the perfect boundary approximation technique which allows accurate modeling of small and curved structures without the need for an extreme refinement of the mesh at these locations [94].

Here is how the simulation works: the 3D model is discretized into a hexahedral 3D mesh. A light source is introduced in the model. This light source is a short pulse of light which will propagate inside the structure. This short pulse of light has a certain bandwidth, which is inversely proportional to the length of the pulse. Some important relations between pulse length, mesh size and wavelengths should be satisfied to obtain reliable results. For example, the larger the bandwidth the shorter the pulse is, therefore the mesh should be small enough. A good rule of thumb is that the bandwidth should be between 90% and 110% of the central wavelength. And that the mesh size in dielectric material should be around a tenth of the central wavelength. For metals, the mesh size should be a fifth of the skin depth of the metal at the central wavelength. These rule of thumbs have been applied for all the simulations realized in this chapter. The solver also features an adaptive mesh size algorithm which runs consecutive simulations by decreasing the mesh size of the model after each run. The S-parameters of the consecutive runs are then compared. The difference between two different sets of S-parameters can be set as a criterion to stop the mesh adaptation. Two criterions are used to stop the transient simulation. The first criterion which is satisfied will stop the simulation. The criterions are, the defined simulation time and the defined amount of the light which has escaped or has been absorbed in the simulation bounding box. This light can be collected by some ports or can escape the model at open boundaries depending on the simulation parameter that the user has chosen. It is to be noted that time-domain simulations

are not well suited for the excitation of high quality factor resonating structures. The light will be trapped in the resonator and the simulation can last a very long time until the light escapes the bounding box of the simulation domain. Plasmonic cavities typically have low quality factor resonances and are therefore well suited to be simulated with the transient solver.

Frequency domain solver The frequency domain solver of CST MWS is also a 3D EM simulator. The frequency domain solver also uses the finite integration technique which uses the integral form of Maxwell's equations. When the excitation and the EM fields in the structure are assumed to be harmonically oscillating functions with a single frequency, the Maxwell's equations can be transformed into the frequency domain. The problem can be reduced to a sparse matrix which needs to be inverted. The simulation is therefore done frequency by frequency. With this solver the structure can be discretized either in hexahedral or in tetrahedral mesh. It has been used during this work several times to compare the results obtained with the transient solver. But because we work in a wide frequency range, the computational effort to find the solution of the problem is reduced with the transient solver.

2.3.2 Fabrication of the integrated PSWC

The fabrication of the device has been exclusively realized in the cleanroom of the Optics & Photonics Technology (OPT) laboratory at Ecole Polytechnique Fédérale de Lausanne (EPFL). It involved the use of several different processes available in the standard complementary metal oxide semi-conductor (CMOS) fabrication [95, 96] which is today used to fabricate microelectronics. If we had used aluminium or copper instead of gold for the PSWC, our device could have been CMOS compatible. This means that potential for low-cost mass production is conceivable.

In this subsection we will describe in detail the machines which we used to fabricate the device. Moreover we will comment on the used recipes and on their development. Generally, the more we approach the nanometer size, the more every recipe needs to be adjusted for its specific application. Therefore, a hard work of trial and error guided by a profound knowledge in the physics of the fabrication process is needed to reach the wanted precision and accuracy. It is also our wish that this chapter may help any newcomer in this field to quickly gain a broad overview of how to fabricate nano-structures.

2.3.2.1 Chip layout

The chip layout has been designed to measure the losses of the waveguides as well as the plasmonic slot waveguide cavity on the same chip. Figure 2.4 shows the layout of the designed chip. An input slab waveguide of $3\mu\text{m}$ width is used to optimized the injection losses into the chip. Then an adiabatic taper of $50\mu\text{m}$ length joins the slab waveguide to a mono-mode silicon strip waveguide. Two 90° bends of $25\mu\text{m}$ radius are shifting the input from the output

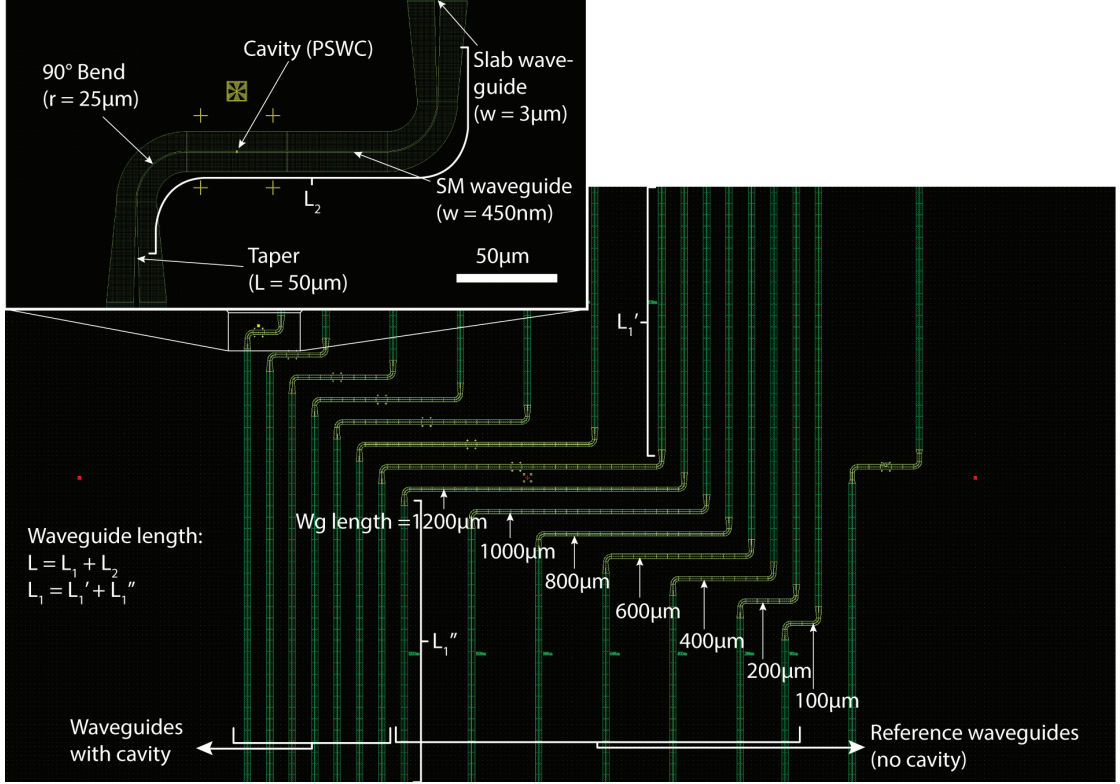


Figure 2.4 – Design of the fabricated chips.

axes to avoid the eventual measurement of excited substrate modes. On the left side of the chip, seven waveguides having a mono-mode strip waveguide length of 100, 200, 400, 600, 800, 1000, 1200 μm are prepared to be patterned with a plasmonic cavity. On the right side, the same seven waveguides of different length are prepared to be used for loss measurement. The length of the input and output slab waveguides is constant for all waveguides. Their lengths depend on the position of the cleaved facet and needs to be measured after cleaving.

The complete fabrication process is shown in Fig. 2.5 and is divided in 10 consecutive critical fabrication steps. In the following subsections we will comment on these steps and show the obtained results.

2.3.2.2 Substrate for silicon photonics

The first choice we had to make, is the substrate. A possibility could have been to start with a bare silicon wafer on top of which some layers would be deposit, like for example a wet oxide followed by an amorphous silicon layer. In that case, the amorphous silicon layer would be the device layer; the layer we would etch to define the silicon waveguides. From the experience of my former colleague Armando Cosentino, we know that the main drawback of using amorphous silicon waveguides, is their high propagation losses. Therefore we decided to use SOI substrates manufactured by Soitec instead of amorphous silicon. The SOI wafers

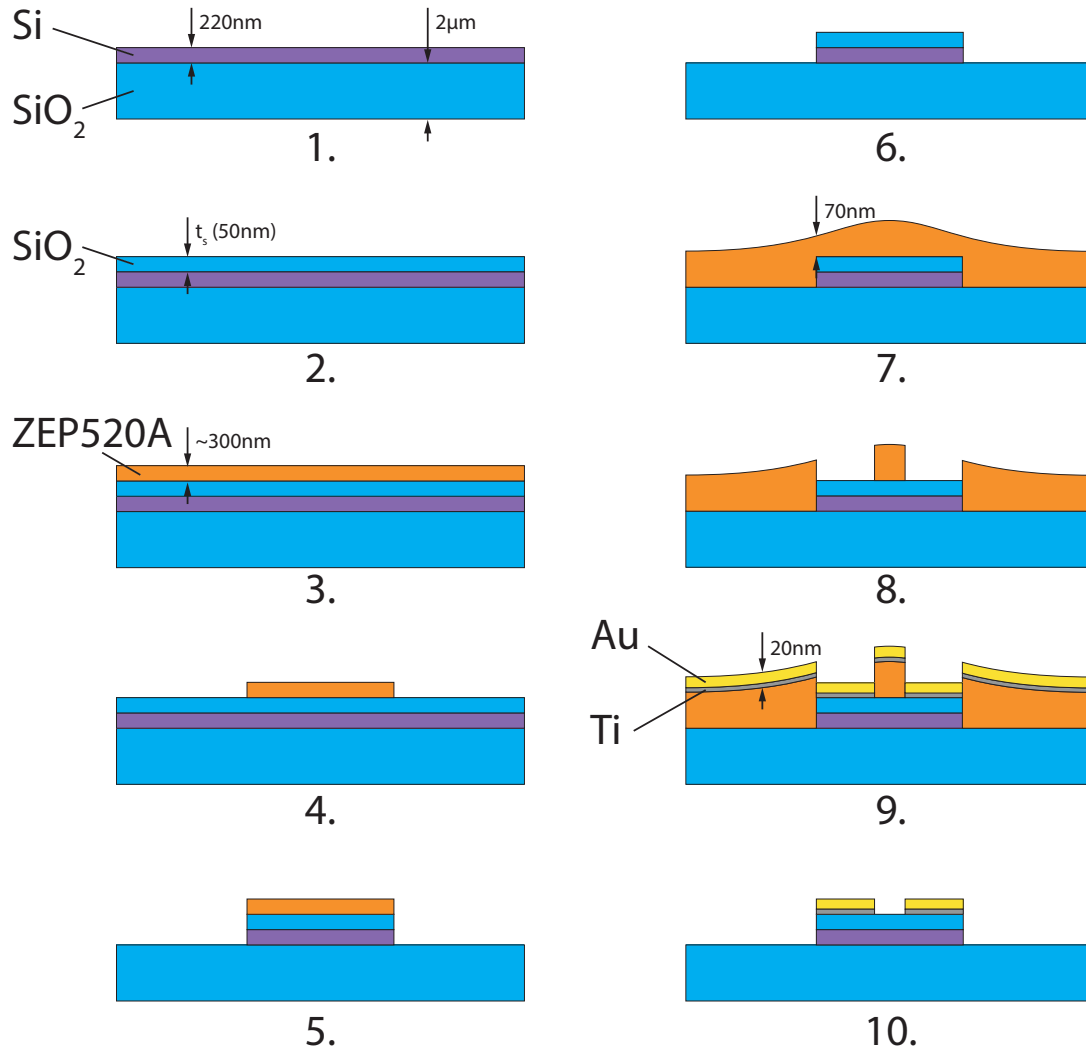


Figure 2.5 – Process flow of the fabrication of the PSWC. 1) silicon-on-insulator (SOI) substrate (handle wafer not shown). 2) Deposition of the SiO₂ spacer by plasma enhanced chemical vapor deposition (PECVD). 3) Spin-coating of ZEP520A e-beam resist. 4) Resist exposition and development. 5) reactive ion etching (RIE) with induced coupled plasma (ICP) etching of the SiO₂ spacer and the silicon waveguide. 6) O₂ plasma ashing of the ZEP520A resist and piranha cleaning. 7) Spin-coating of ZEP520A resist. 8) Exposure and development of the resist. 9) Evaporation of titanium seed layer and gold layer. 10) Metal and resist lift-off followed by a piranha cleaning.

are made out of three layers: the handle wafer, the buried oxide and the device layer. The used SOI substrates have a diameter of 200mm with a silicon handle wafer having a thickness of $725\mu\text{m}$ and a (100) crystal orientation. The buried oxide is a silicon oxide layer of $2\mu\text{m}$ thickness. And the device layer is a single crystal p-doped silicon layer with a resistivity of $10\ \Omega\cdot\text{m}$, a (100) crystal orientation and a thickness of 220nm. The notch of the wafer is oriented in the $\langle 110 \rangle$ axis. In order to be able to work with a higher flexibility, these 200mm SOI wafers are diced into 20 by 20mm square chips. Before dicing, a protection layer of $5\mu\text{m}$ of AZ1500 is spin-coated on both sides of the wafers. The dicing cuts are made along the $\langle 110 \rangle$ axis to be able to easily cleave the chips after the fabrication.

2.3.2.3 SiO_2 spacer deposition by plasma enhanced chemical vapor deposition

The first fabrication step shown in Fig. 2.5(1.) and done on the 20 by 20mm square samples is the deposition of a layer of silicon dioxide. It is made on an "Oxford Instrument PlasmaLab 80+" PECVD system. A standard recipe provided by Oxford Instruments (see Appendix A.1.1) is giving layers of silicon dioxide having a refractive index of 1.45 at $\lambda = 1500\text{nm}$ at a deposition speed of 1.06nm/s . A 50nm spacer thickness has been deposited on our samples which were previously cleaned in piranha.

2.3.2.4 E-beam lithography

Tomorrow's CMOS patterning technology will be done on wafers of 450mm of diameter with extreme ultraviolet lithography (EUVL) ($\lambda=13.5\text{nm}$), achieving resolutions smaller than 22nm. The lithography machines (called steppers) used to achieve these resolutions provide a high parallel throughput (more than 1000 exposed wafers per 24h). They cost several hundreds of millions of dollars and are not compatible with a research environment due to their extremely high cost of ownership and their low flexibility. To achieve the patterning with similar resolution, universities and research institutes often use electron beam lithography (EBL) to pattern shapes in the nanometer scale. EBL can have resolutions smaller than 20nm but is lacking the throughput of standard optical lithography as it is a scanning process [97]. The focused electron beam is scanned point by point over the electron sensitive resist. Even if the scan speed can be several tens of MHz, the exposure process is very long. For example: to pattern an area of $1 \times 1\text{cm}$ with nanometer sized patterns having a fill factor of 50%, roughly 72 hours of exposure is needed on our Raith 150 EBL system. Depending on, the required resolution, the used e-beam resist and scanning step size, the exposure process can however be accelerated.

All the patterning steps needed for the fabrication of the PSWC are produced with a Raith 150 EBL machine. The Raith 150 system has a column manufactured by Leo which is called Gemini (now bought by Zeiss) and which is specially build to have high resolution at low accelerating voltages. It can be operated between 200eV and 30keV. The Raith 150 has a 20MHz pattern generator and the possibility to use 6 different apertures. It is equipped with a laser

interferometric stage which has a travel range of 6 inches and a position accuracy down to 5nm.

In our work the acceleration voltage is always used at 20keV to have a larger depth of field. The depth of field is important when exposing thick resist as it helps getting straight walls. Depending on the exposure dose, the step size and the depth of field, 6 different apertures of following diameter can be used: 7.5 μm , 10 μm , 20 μm , 30 μm , 60 μm and 120 μm . The dose to clear your EBL resist depends on the resist and the acceleration voltage. The dose is defined by equation 2.6. Since our digital pattern generator is limited to 20MHz the dwell time cannot be smaller than 50ns. In practice it is usual to work even above 500ns of dwell time. For a fixed aperture giving a certain amount of beam current, the speed at which the system can expose the pattern is limited by the minimal area dwell time. The larger the aperture is, the more current you get in the probe and the less depth of field you will get. For large structures, large step sizes are used with large apertures to speed up the exposure and when small high resolution structures are exposed, small step sizes and small apertures are used.

$$\text{area dose} = \frac{\text{beam current} \cdot \text{area dwell time}}{(\text{area step size})^2} \quad (2.6)$$

PSWC exposure The PSWC are fabricated with a lift-off technique in which the exposed resist needs to have at least a thickness twice as high as the wanted metal thickness. Moreover the quality of the lift-off is getting better if the resist walls are exhibit and under cut profile. This can be done by two different technics: either the use of a double resist layer made out of two different resists having different molecular weights in which the bottom layer will be dissolved faster than the top layer; or the use of a single resist layer being over exposed.

In Fig. 2.6 a single layer of ZEP520A of 70nm thickness is exposed with different doses and different gap sizes. For each dose the slot width is swept from 30 to 70nm. Four different doses from 40 to 70 $\mu\text{C}/\text{cm}^2$ are tested (a. to d.). The ZEP520A layer is obtained by spin-coating a diluted ZEP520A mixture (ZEP520A : Anisol 1:2 by volume) at 2000rpm for 60sec. It is followed by a 5min pre-bake at 180°C. The exposure is done at 20keV of acceleration with the 7.5 μm aperture. The exposure step size is 5nm, and the used write field is 50 by 50 μm . The development is made in an n-amyl-acetate solution for 1min followed by a 1min rinse in a Methyl isobutyl ketone (MIBK) : Isopropyl alcohol (IPA) solution (9:1 by volume). After the development, the samples are cleaned from any resist residues in a O₂ plasma of 50W (platen) for 30sec in a STS Multiplex RIE ICP etcher (see appendix A.1.2 for more details). The samples are then coated with a 1.5nm thick titanium adhesion layer followed by a 20nm thick gold layer. The coating is made in an Edwards AUTO306 e-beam evaporator. After the coating, the unwanted metal layer is lift-off by striping the unexposed resist in a bath of n-méthyl-2-pyrrolidone (NMP) at 60°C for 10min helped afterwards by a megasonic excitation of 20sec at 600W of power.

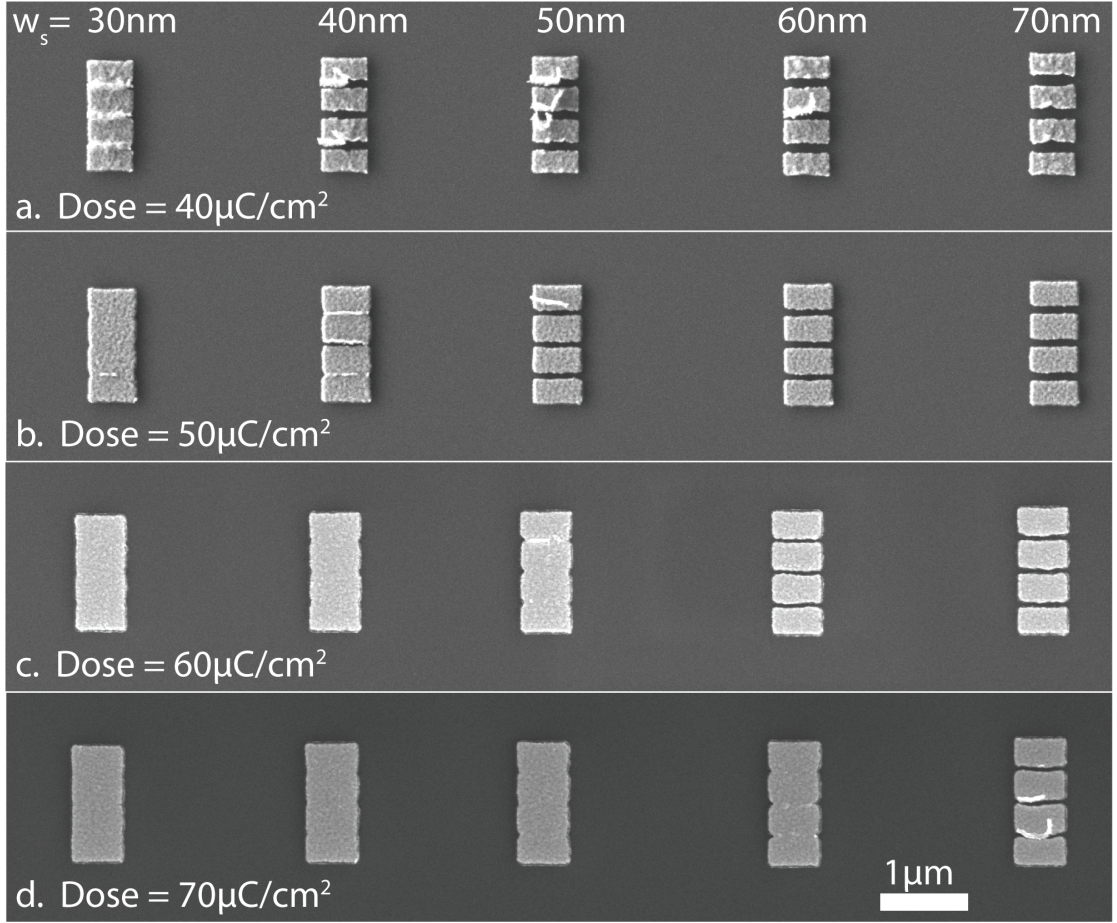


Figure 2.6 – Dose test from 40 to 70 $\mu\text{C}/\text{cm}^2$ for five PSWC with different gap sizes exposed on a 70nm thick ZEP520A resist on a silicon substrate. The gap ranges (w_s) from 30 to 70nm from left to right.

For a dose of 40 $\mu\text{C}/\text{cm}^2$ the resist is not completely cleared out after the development. It can be observed in Fig. 2.6 that the metal layer for a dose of 40 $\mu\text{C}/\text{cm}^2$ seems to be rough. This probably comes from an underlying resist layer which could not be removed during development. A short O_2 plasma could have been helpful to strip it. But we preferred to work with higher doses where the side wall roughness of the slot seemed to be of better quality. The best result in Fig. 2.6 shows that the ideal dose is 50 $\mu\text{C}/\text{cm}^2$ and the ideal gap size is 50nm.

Waveguide exposure The EBL of the silicon waveguides is a critical process to achieve low propagation losses and single mode operation. According to our simulations, the waveguides should have a width of 450nm to be single mode from $\lambda = 1200\text{nm}$ to 1700nm. To obtain a resist pattern of that width, it is not sufficient to design a layout with 450nm waveguide width. In fact, because the focused electron beam has a finite diameter, which is roughly around several nanometers, the exposed and developed pattern never correspond exactly to

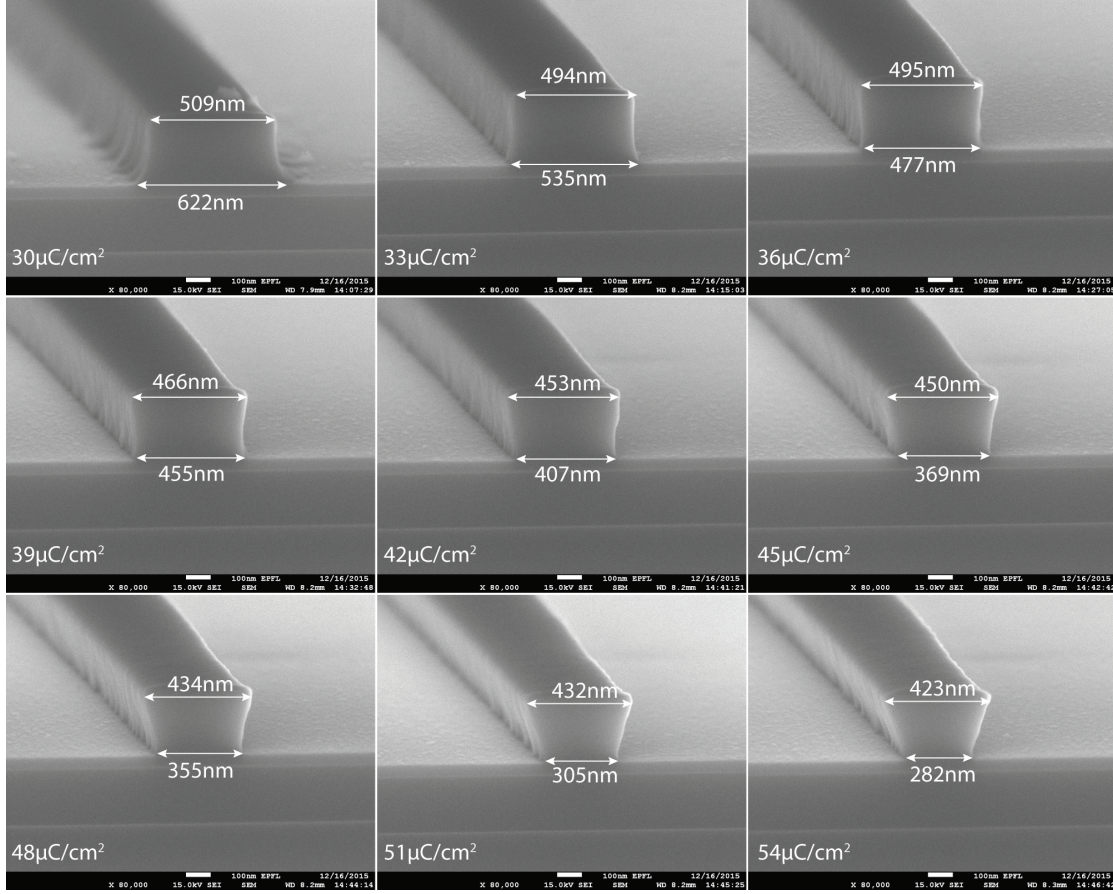


Figure 2.7 – scanning electron microscope (SEM) images showing the developed waveguides having all a width of 600nm in the layout for different exposure doses in ZEP520A resist.

the size of the designed layout. Moreover, the interaction of the electrons with the resist and the substrate is generating secondary electrons which tends to broaden the exposed area. In the practice it is possible to correct these proximity effects thanks to developed simulation tools like Monte-Carlo simulation. This is called proximity correction [98].

For the patterning, we used the positif EBL resist ZEP520A as an etch mask. It is exposed on the Raith 150 EBL tool at an acceleration of 20keV, with an aperture size of $10\mu\text{m}$. The exposure step size is set to 8nm and the write field to 50 by 50 μm . We exposed an area around each side of the waveguide of 10μ width. So every point exposed around the waveguide will slightly contribute to the exposure of its neighbor points. This can be seen in the SEM images of Fig. 2.7 where a dose test of a waveguide having a designed width of 600nm in the layout is shown. The maximum width of the waveguide for any dose is way smaller than the designed 600nm. Therefore, optimal exposure parameters and the optimal design width needs to be found to obtain the wanted 450nm. We did five dose tests for designed waveguide width of 450nm to 650nm in 50nm steps. In Fig 2.7 the dose influence on the sidewall angle can clearly be seen. The optimal dose where sidewall angle is 90° is between 33 and $36\mu\text{C}/\text{cm}^2$. We finally chose to

over-expose the resist slightly with a dose of $39\mu\text{C}/\text{cm}^2$ because it reduced the errors along the waveguide induced by the stitching error.

2.3.2.5 Dry etching of waveguides

Dry etching involves the use of an etchant gas phase combined with the generation of a plasma. In the plasma, the gas is decomposed in ions, neutral free radicals and electrons. Two etching mechanisms are involved in dry etching: Physical etching produced by the ion bombardment (sputtering) and chemical etching produced by the oxidation of free radicals which are diffusing to the substrate. Several types of dry etching reactors exist. The two most common are the parallel plate etcher in which RIE occurs and the high density plasma ICP etcher. The main difference between both is that in an ICP etcher, the plasma density is decoupled from the ion acceleration in the direction of the sample. Thus the chemical etching is decoupled from the physical etching. For further reading about dry etching we recommend the book from J.D. Plummer [99].

Based on the well known "Bosch" process used for deep RIE of silicon [100, 101], which is made out of two alternating steps of etching with SF_6 and deposition with C_4F_8 , we developed a mixed-mode etching process, which is sometimes called "pseudo Bosch process" or "continuous Bosch process" to etch our silicon waveguides [102]. This mixed-mode process uses the same gases as the standard "Bosch" process but in a single joint step. We worked with an STS Multiplex ICP etcher with a fluorinated chemistry based on SF_6 and C_3F_8 (C_4F_8 can also be used). Both gases are acting simultaneously. The SF_6 gas produces fluor radicals which are chemically etching the silicon. The C_3F_8 gas produces CF_x radicals which are polymerizing on the surface in nCF_2 form [103]. This thin polymer layer acts like an etch mask which can be etched faster vertically than laterally. In this case it is possible to have an anisotropic etching behaviour. This etching method is well suited for shallow etches of less than $4\mu\text{m}$ where sidewall roughness needs to be minimal [104]. It is therefore a perfect candidate for etching silicon waveguides.

The dry etching of the silicon waveguides is a crucial step since the quality of the etch process will significantly affect the propagation losses of the waveguide. Fig. 2.8 shows an etched waveguide obtained with our developed etching process. The process is divided in two etch steps. The first step etches the 50nm SiO_2 spacer. The second step etches the 220nm of silicon. Detailed information about the etch recipes can be found in the appendix A.1.2. After the optimization of the etching recipe, the resulting side wall roughness is mainly induced by the roughness of the exposed ZEP520A EBL resist. To reduce the side wall roughness of silicon wire waveguides different techniques were investigated [105]. One possibility was to use smaller exposure step size during EBL. Another one was to make a post-bake of the e-beam resist before etching at 150°C for 5min in an oven [106]. This would slightly reflow the ZEP520A resist and attenuate the roughness induced by the EBL. Another method, which could be investigated is the thermal annealing in hydrogen atmosphere [107].

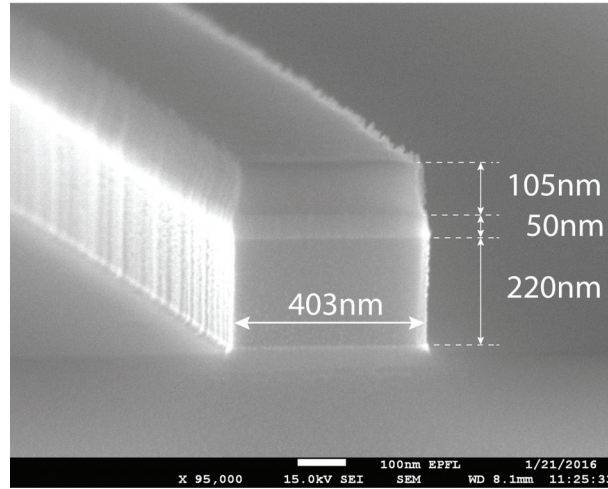


Figure 2.8 – Single mode silicon waveguide with SiO₂ spacer etched with "pseudo Bosch process".

2.3.2.6 Conformal coating of ZEP520A

In the process of creating the PSWC on top of the silicon wire waveguide, first we need to etch the waveguides and then make a lift-off process with an e-beam patterned ZEP520A layer. This ZEP520A layer needs to be spin-coated on a structured surface. We have already demonstrated that we are able to fabricate the PSWC on a blank wafer which has a perfectly flat surface. In that case, a 70nm thick layer of ZEP520A is spin-coated onto the wafer. This is enough to make a lift-off of a 20nm gold layer. But in the case where the waveguides are already etched, we should be able to coat the upper surface of the waveguides with 70nm of resist. We made some tests to know which spin-coating parameters we should use to get the right thickness. In Fig. 2.9(a) we coated the structured surface with the same recipe giving a 70nm thick layer on a non-structured surface. It appeared that the ZEP520A coating is not very conformal and that the thickness of the resist on top of the waveguide is only 17nm. This is not enough to proceed with the lift-off step of the PSWC. In Fig. 2.9(b) we changed the dilution ratio of the ZEP520A resist to 1:1 with Anisol in order to make it a bit more viscous. With the same spin-coating parameters, the coating became conformal and covered the waveguides with a resist thickness on top of the waveguides of around 70nm.

2.3.2.7 Mix & match exposure for on waveguide metal lift-off

The last fabrication step is the exposure of the PSWC on top of the etched waveguides. Since this is an EBL step which needs to be aligned on an already existing pattern, it is called a mix & match exposure. The required alignment accuracy needs to be in the order of tens of nanometers. Theoretically, our EBL tool has the required alignment accuracy. But in reality, a lot of external parameters makes the task very difficult. The PSWC was exposed with the same parameters as described in section 2.3.2.4.

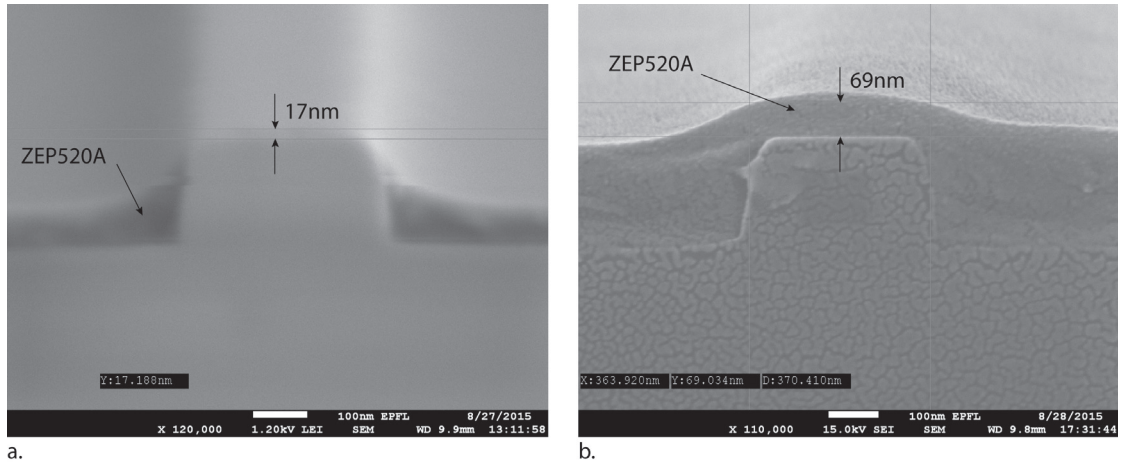


Figure 2.9 – Cross section of the etched waveguides coated with ZEP520A e-beam resist. a) ZEP520A : Anisol 1:2 dilution: Spin-coating at 1000rpm for 60sec with an acceleration of 500rpm/s. b) ZEP520A : Anisol 1:1 dilution: Spin-coating at 1000rpm with an acceleration of 500rpm/s.

During the exposure step of the waveguides, 4 alignment marks were exposed in the four cardinal points of the chip. These alignment marks are read before the second exposure to adjust the local coordinates to the one of the chip. Once this alignment is done, the interferometric stage is able to drive to the wanted position and the PSWC can be exposed on top of the waveguides. Unfortunately, during the very long exposure of the waveguides, the mechanical stage of the EBL tool drifts slightly due to temperature changes. This leads to a non-linear and unpredictable shift of several hundreds of nanometers of the waveguide position relative to the alignment marks. We reduced this drift dramatically by letting the stage stabilize in temperature after the loading of the sample in the vacuum chamber for 6 hours at least before the exposure of the waveguides. In that case, the position accuracy can be minimized to around 50nm. Another successful attempt to increase the alignment accuracy was to make other alignment marks very close to the location where the PSWC needed to be exposed. In this case, the four main alignment marks were used to locate the auxiliary alignment marks, and a second automatic alignment procedure was done on the auxiliary alignment marks to locally align the PSWC position to the waveguide. Moreover, we designed the PSWC with three slots instead of one to increase our chances to have one slot aligned on the waveguide in the case of a misalignment. In Fig. 2.10 a typical result of a good PSWC alignment is shown. We see the auxiliary alignment marks (crosses) which are located in the same write field used to expose the PSWC. Here the PSWC cavity length is 600nm and the slot width is 50nm. Thanks to the precise alignment achieved, we could, in a further fabrication step, try to expose a PSWC with only one slot.

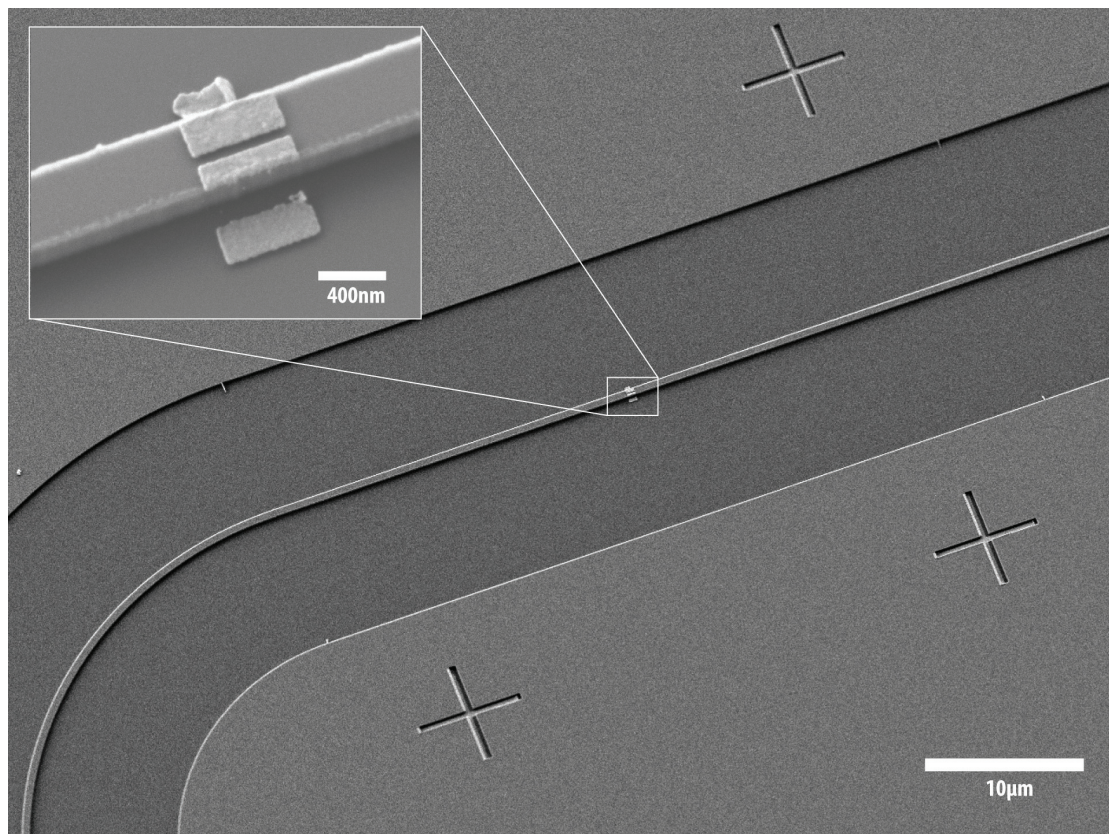


Figure 2.10 – PSWC aligned on top of a single mode silicon waveguide.

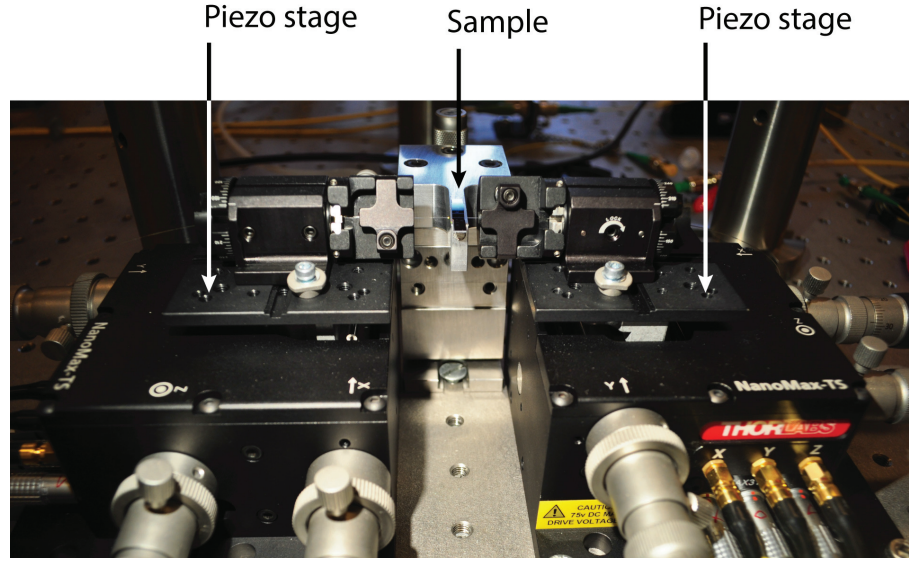


Figure 2.11 – Picture of the injection setup used to measure the waveguide transmission.

2.3.3 Experimental setup

To characterize the silicon based integrated sensor we needed to build a reliable experimental setup. This versatile experimental setup can be used to measure the sample transmission in two different ways: the wavelength interrogation method and the broadband interrogation method. Moreover, it is possible to simultaneously measure the far field scattering of the device under test (DUT). In the next sections we will comment in detail these three different measurement methods.

2.3.3.1 Waveguide injection setup

The light is coupled to the waveguide through a pair of lensed fibers from Nanonics. The injection lensed fiber is polarization maintaining (PM) and has a working distance of $6 \pm 1 \mu\text{m}$ and a spot size of $2 \pm 0.3 \mu\text{m}$. The output lensed fiber is a standard single mode fiber having a working distance of $4 \pm 1 \mu\text{m}$ and a spot size of $1.7 \pm 0.3 \mu\text{m}$. Both of these lensed fibers are clamped in on a high precision bare fiber rotator from Thorlabs so that the slow axis of the PM lensed fiber can be adjusted to the waveguide geometry. Each bare fiber rotator is then fixed onto a 3-axis closed-loop piezo nano-positioning stage from Thorlabs (NanoMax). The chip under investigation sits on a home made aluminum chip holder which can be heated or cooled with a peltier element. Two thermistors are incorporated inside the holder to measure the temperature. One is placed close to the peltier element as fast acting feedback for the temperature control and the other is placed just under the sample to measure the sample temperature. This sample holder is mounted on a manual 2-axis stage actuated by two high precision differential micrometer screws from Newport (ULTRAlign).

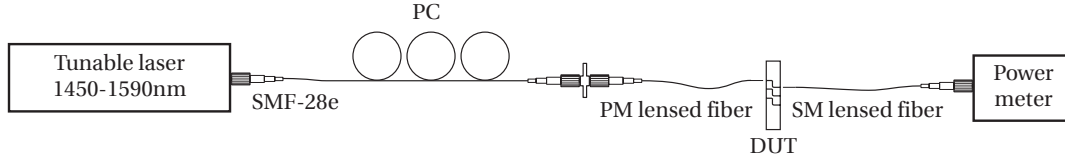


Figure 2.12 – Wavelength interrogation method optical setup.

2.3.3.2 Wavelength interrogation method

The easiest method of measuring the light propagation inside a waveguide is to measure its transmission for a single wavelength. If we want to measure the transmission over a certain wavelength range, we can do it with a tunable laser source. The transmission is consecutively measured for several wavelengths in a certain bandwidth allowed by the tunable laser source. In our case, we used a HP 8168F external cavity laser having a tunable wavelength range extending from 1450nm to 1590nm. Fig. 2.12 shows a detailed drawing of the optical setup. At the output of the tunable laser, a SMF-28e single mode fiber is launched into a manual fiber polarization controller (PC) which is then connected to the PM lensed fiber. The polarization controller is used to rotate the polarization to enable transverse electric (TE) or transverse magnetic (TM) excitation of the waveguide without realigning the lensed fiber. The light coming out of the waveguide is collected by a single-mode (SM) lensed fiber. The measurement of the transmitted output power through the waveguide is measured with a InGaAs photodiode power sensor from Thorlabs (S154C).

2.3.3.3 Broadband measurement set-up

In this method, we want to inject a continuous spectrum ranging from 1200 to 1700nm into the waveguide and measure the transmission through the waveguide with a ANDO AQ6315B spectrum analyser. The generation of a continuous spectrum can be achieved with either the combination of two super luminescent diodes or by a supercontinuum laser. We used a supercontinuum laser from NKT photonics (SuperK EXTREME EXW-12). The output spectrum of the this laser is ranging from 450nm to 2400nm and is unpolarized. We needed to build an optical setup to filter out the unwanted wavelengths and to polarize the light linearly. In Fig. 2.13 we show the optical setup to polarize, filter and inject the linearly polarized supercontinuum spectrum inside the slow-axis of a PM1300-XP PM fiber. We used two Glan-Taylor polarizers in a row to obtain a polarization extinction ratio better than 100000:1. A dichroic beam splitter plate having a long pass at 900nm is reflecting the wavelengths from 450 to 900nm and transmitting the wavelength from 900 to 2400nm. The beam containing the visible part of the spectrum is not used in our experience but can be used in case it is needed. The near infrared spectrum is then filtered again to remove the 900 to 1200nm part of the spectrum. A beam sampler is used to monitor the power of the laser with a photodiode. As the supercontinuum laser might suffer from power drifts over time, the photodiode signal is used

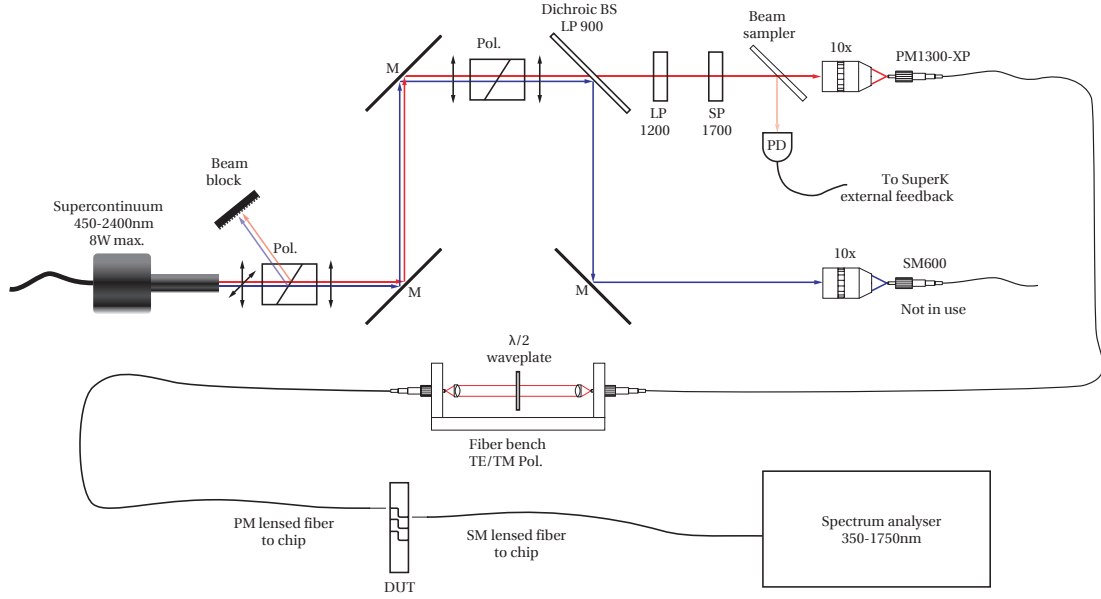


Figure 2.13 – Light management setup of the supercontinuum laser source and fiber injection.

as an external feedback signal to stabilise the output power of the laser. Finally the beam is injected into the slow-axis of the PM fiber.

Once the wanted spectrum is injected into the PM fiber, the beam is later collimated again in free space and passes through a $\lambda/2$ wave-plate to easily rotate the polarization to the fast-axis of the PM fiber. This allows us to quickly change the excitation of the waveguide from TE to TM without touching the alignment of the lensed fiber.

2.3.3.4 Far field scattering measurements

To collect the far field scattering of the resonating PSWC we built an optical setup on top of the sample. As shown in Fig. 2.14, the principle of the setup is to image the PSWC onto the core of a single mode fiber. For alignment purposes, the visible part of the spectrum should be imaged onto a charge-coupled device (CCD) camera. We used an infinitely corrected Mitutoyo M Plan Apo near infrared (NIR) 20x objective which is optically corrected for wavelengths from 400nm to 1600nm. The objective is combined with a Mitutoyo MT-L tube lens which is also corrected for the same wavelengths. Between the objective and the tube lens a dichroic beam splitter reflects the visible spectrum up to 950nm in the direction of the CCD camera. The Infrared part of the spectrum is transmitted through the beam splitter and is imaged by the tube lens onto the SMF-28e single mode fiber having a core diameter of 8.2 μ m. The magnification of the optical system is 20x and the size of the image of the PSWC is roughly the same size as the core diameter of the SM fiber. Therefore we avoid to collect light scattered from other parts of the sample. A standard achromatic doublet has been used as tube lens to image the visible

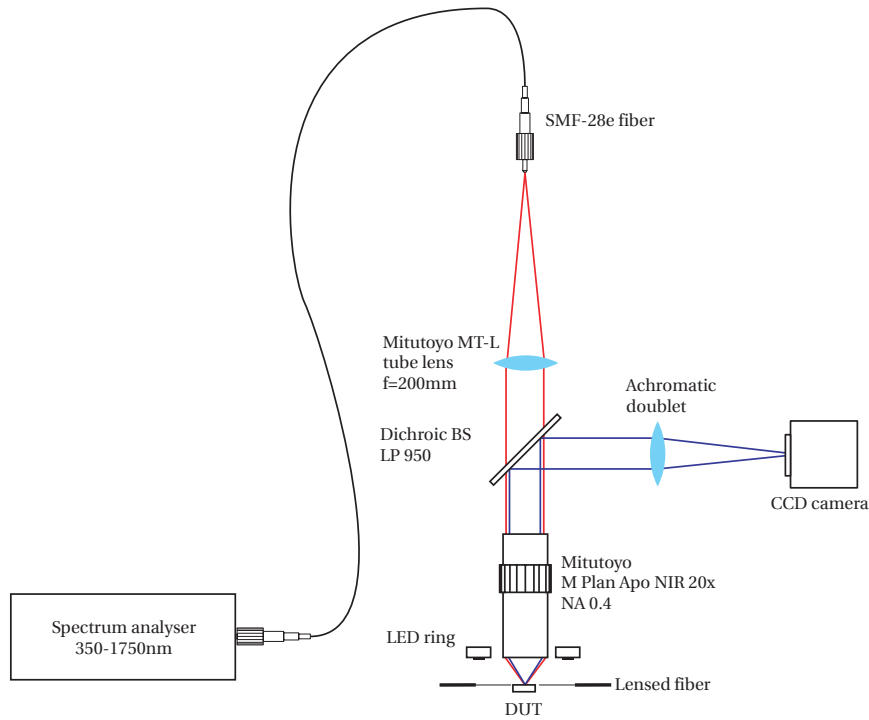


Figure 2.14 – Far field scattering optical setup.

part onto the CCD. To align the single mode fiber to the PSWC, we used a pigtailed laser diode emitting at 660nm that we connected instead of the SMF-28e SM fiber. With the image of the CCD camera we located the PSWC and placed it in the middle of the field of view. We aligned the single mode fiber connector of the laser diode to obtain a perfectly focalised spot on top of the PSWC. Then, we exchanged the laser diode connector with the SMF-28e fiber. At this point, we connected the SMF-28e fiber to a photodiode power sensor and a signal could already be detected. The SMF-28e fiber connector is then align laterally to maximize the collected signal. This alignment is very sensitive and should need a piezo positioning system to be really accurate. Nevertheless, with patience, a strong signal of several hundreds of nanowatts can be collected. When the signal is maximized, we can connect the fiber to the optical spectrum analyser and start with the measurement.

2.4 Simulation Results

Before starting with the fabrication of the chip, we made a complete theoretical study of the final device. The results shown in this section are mainly coming from finite difference method simulations done with the commercial software CST Microwave Studio (CST MWS). The device was simulated by starting with the silicon waveguides used to bring the light to the plasmonic slot waveguide cavity (PSWC). Then we simulated the guiding behavior of the plasmonic slot waveguide, followed by its coupling to the silicon waveguide. We investigated the best coupling conditions of the waveguide to the plasmonic cavity. Finally we simulated the sensing performance of the complete device under different conditions. After we finished the fabrication of the devices, we measured their performance on the optical characterization bench shown in Fig. 2.11. We measured the losses of the fabricated silicon wire waveguides with the Fabry-Pérot method. We measured the transmission spectra of the device with and without the cavity in air to make a normalization and find the resonance position. Moreover, to consolidate our results acquired through the waveguide transmission characteristics, we measured the far-field scattering of the plasmonic cavity. Finally, we measured the resonance position shift for different outer medium to calculate the sensitivity and the detection limit of our sensor.

All simulation results were obtained either with the time domain solver or the frequency domain solver of CST MWS. For broadband simulation we used the time domain solver and for single frequency we used the frequency domain solver.

2.4.1 Silicon photonics building blocks

Silicon waveguides are commonly used to guide light in densely packed areas thanks to their strong light confinement ability [108, 109]. Silicon is transparent to wavelengths from 1.1 to 5 μm . It is often used as waveguide material in the telecom bands (1260 to 1675nm) for on-chip systems. On a technological point of view, silicon waveguides emerged with the commercialization wafers having a thin single crystal silicon layer on top of micrometer sized thermal silicon oxide. The single crystal layer of silicon dramatically decreases the propagation losses in the device. This technology is called silicon-on-insulator (SOI) [110] and comes directly from the advances of silicon electronic chip manufacturing. In our case, we used SOI wafers with a "box" layer of 2 μm thickness of SiO_2 and a device layer of 220nm thickness of p-type doped silicon having a resistivity of 11.5 Ωcm and (100) orientation. This is the standard platform for integrated silicon photonics.

To bring the light to the "on-chip" PSWC, two different sizes of silicon waveguides are used as well as an adiabatic taper and two 90° bent waveguides. These building blocks are now becoming very common in silicon photonics technology to route the light on a chip. The main concern here is to minimize the propagation losses and maximize the injection from the lensed fibers over a wavelength bandwidth going from 1200-1700nm. Therefore we simulated all the different building blocks and optimized them to choose a final design which we used

for the final fabrication of the chip.

2.4.1.1 Injection optimized silicon slab waveguide

To inject the light into the silicon waveguide, several options are available like prism coupling, grating coupling, butt coupling or end-fire coupling (with a lens) [111]. As we worked with a bandwidth of 500nm corresponding to 35% of the center wavelength we couldn't use a prism or a grating coupler which both have a limited bandwidth of typically 5 to 7% of the center wavelength [112, 113, 114]. We decided to use end-fire coupling with a polarization maintaining (PM) lensed fiber. This choice has a better coupling efficiency compared to butt coupling with a cleaved fiber. Since the typical mode field diameter (MFD) of a PM1300 fiber is around $9\mu\text{m}$ which is way larger than the $2\mu\text{m}$ spot size of the PM1550 lensed fiber, most of the light can not be injected with butt-coupling. The coupling efficiency is determined by the numerical aperture (NA) match and the mode field overlap. A rough approximation of the NA of the waveguide can be found with this formula: $\text{NA} = \sqrt{n_{\text{core}}^2 - n_{\text{cladding}}^2}$. The Δn is so large that for any angle the light is injected in the silicon waveguide. Thus, we assumed a perfect NA match during the coupling. It is important to notice that even if the high refractive index of silicon has the advantage of having a high NA, it has the drawback of having large reflection at the waveguide facet. The reflection is given by the Fresnel equation which for normal incidence is equal to $R = \left(\frac{n_2 - n_1}{n_2 + n_1}\right)^2$ and gives approximately 30% of reflection in the case of a air to silicon interface.

We calculated the insertion losses versus the MFD of the excitation field into a $3\mu\text{m}$ by $0.25\mu\text{m}$ single mode silicon waveguide. The power injection losses are given by the squared overlap integral Γ^2 given by the equation 2.9. The excitation field is approximated by a gaussian radially symmetric electric field distribution and is given by equation 2.7 where w_0 is the MFD ($1/e^2$) of the fiber or the spot size in the focal point of the lensed fiber. The rectangular waveguide mode field is approximated by a gaussian X-Y mirrored symmetric electric field distribution and is given by equation 2.8 where w_x and w_y are the width and the height of the waveguide core.

$$E_1 = \exp\left(-\frac{(x^2 + y^2)}{w_0^2}\right) \quad (2.7)$$

$$E_2 = \exp\left(-\left(\frac{x^2}{w_x^2} + \frac{y^2}{w_y^2}\right)\right) \quad (2.8)$$

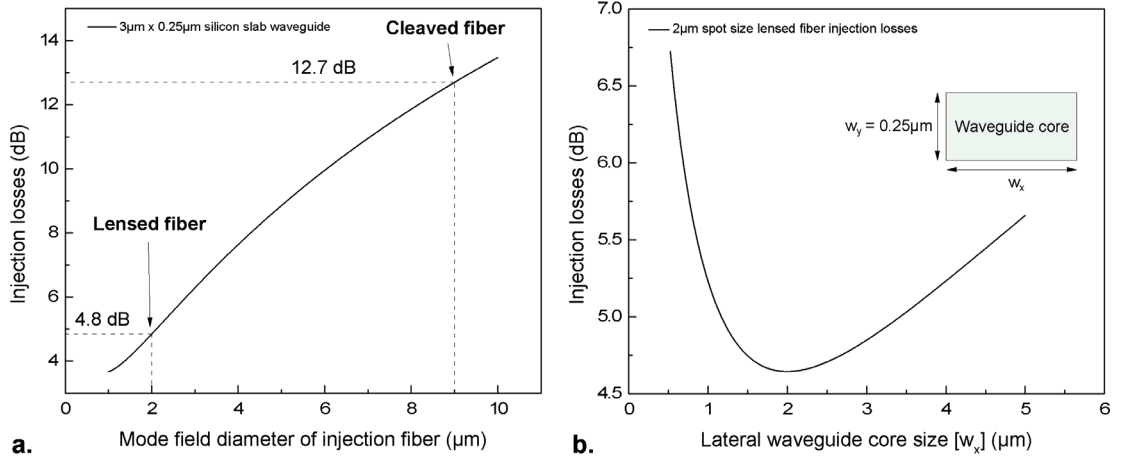


Figure 2.15 – a) Comparison of injection losses inside a $3\mu\text{m}$ by $0.25\mu\text{m}$ silicon slab waveguide between a butt coupling with a PM1300 fiber having a $9\mu\text{m}$ MFD and an end-fire coupling with a PM lensed fiber having a spot size of $2\mu\text{m}$. b) Coupling losses of a $2\mu\text{m}$ spot size lensed fiber versus the lateral size of a rectangular silicon slab waveguide having a $0.25\mu\text{m}$ height.

$$\Gamma = \frac{\int_{-\infty}^{\infty} dy \int_{-\infty}^{\infty} E_1 E_2 dx}{\left(\int_{-\infty}^{\infty} dy \int_{-\infty}^{\infty} E_1^2 dx \cdot \int_{-\infty}^{\infty} dy \int_{-\infty}^{\infty} E_2^2 dx \right)^{\frac{1}{2}}} \quad (2.9)$$

Figure 2.15(a) shows a reduction of 8dB in the injection losses when an end-fire coupling with PM lensed fiber having a $2\mu\text{m}$ spot size is used instead of a simple butt coupling with a $9\mu\text{m}$ MFD fiber. Moreover in Fig. 2.15(b) we observe a minimum coupling loss for a waveguide width having the same size as the spot size of the used lensed fiber. The losses are rapidly increasing if the waveguide size becomes smaller than the spot size of the fiber. We decided to fix the width of the injection slab waveguide to $3\mu\text{m}$ for all the upcoming experiments and simulations to minimize the coupling alignment error.

2.4.1.2 Single mode silicon wire waveguide

Silicon wire waveguides have a cross-section which is rectangular to nearly squared and can sustain a quasi-transverse electric (q-TE) mode and a quasi-transverse magnetic (q-TM) mode depending on the size of the waveguide. Because of its large Δn index contrast of 40% the total internal reflection occurs at very large angles. Thus a good rule of thumb to satisfy the single mode condition is that the size of the waveguide should be in the order of half the wavelength or smaller. In our case, the working wavelength range was 1200nm to 1700nm and the desired mode which was able to excite the plasmonic slot waveguide is the q-TE mode.

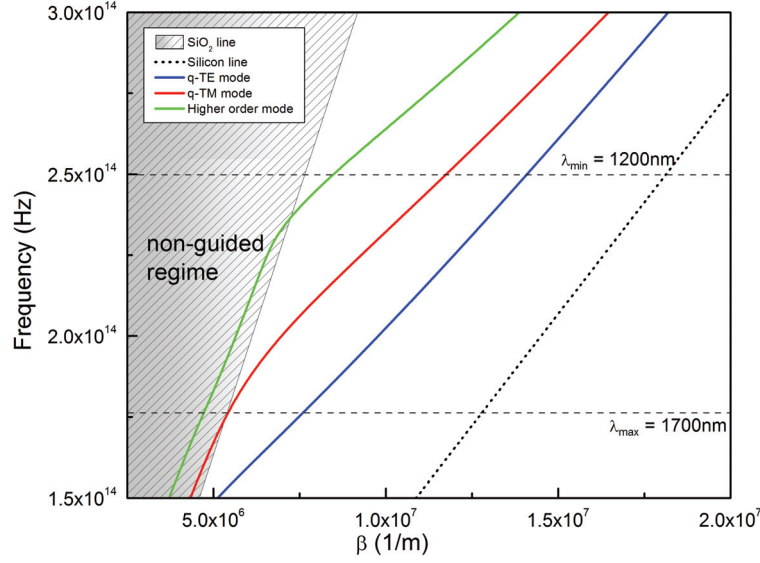


Figure 2.16 – Dispersion diagram of a silicon wire waveguide of 450nm by 220nm cross-section on top of a 2 μ m thick SiO₂ cladding and outer medium of refractive index of 1, showing the two allowed propagating modes q-TE and q-TM over the desired wavelength bandwidth from 1200nm to 1700nm.

We see in Fig.2.16 that the two fundamental modes are propagating in the waveguide in the wanted wavelength range and that the third higher order mode is located in the light cone which means that it is not fulfilling the propagation conditions. To excite only the q-TE mode, polarized light injection which is parallel to the electric field of the q-TE mode needs to be used.

The height of the silicon waveguide is given by the used SOI wafers and in our case it was 220nm as written before. Only the width of the waveguide can therefore be chosen to influence the propagation characteristics of the waveguide. It has been shown that the larger the waveguide is, the smaller the losses are. Therefore and according to the calculations we made, we chose a width of 450nm which was the largest design staying single mode over our entire bandwidth.

2.4.1.3 Silicon waveguide adiabatic taper

An adiabatic taper is simply a funnel linking the 3 μ m wide silicon slab waveguide to the 450nm wide silicon wire waveguide. Adiabatic means that there is no energy transfer between the initial state and the final state of the device. In other words, the q-TE mode of the 3 μ m large slab waveguide will be transformed to the q-TE of the silicon wire waveguide without losses. If the size of the large waveguide is reduced slowly enough, this property should be achieved. As we used a large bandwidth, broadband simulations of the transmittance of the adiabatic taper needed to be done. Fig. 2.17 shows the broadband transmission of the taper when it is excited from the 3 μ m width facet with the fundamental q-TE mode. The simulation is

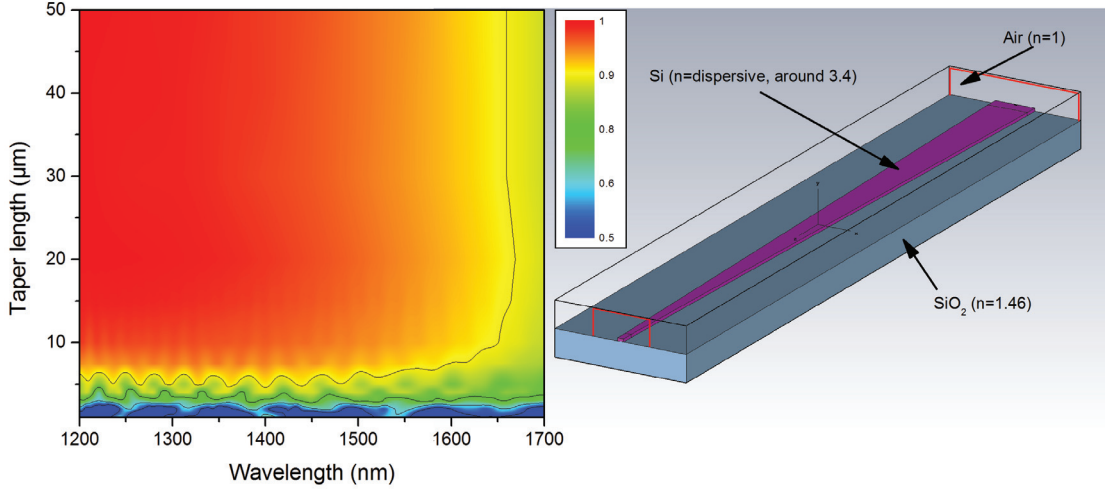


Figure 2.17 – Transmission for different taper lengths calculated with the time domain solver of CST MWS showing the losses from 1200 to 1700nm. $2\mu\text{m}$ SiO_2 substrate ($n_{\text{SiO}_2}=1.46$), $3\mu\text{m}$ by 220nm silicon slab input waveguide, 450nm by 220nm silicon wire output waveguide. The silicon material properties have been taken from D. E. Aspnes and J. B. Theeten [2]. They include material dispersion which is fitted with a second order polynomial. The top cladding above the waveguide is air.

made with the time domain solver of CST MWS. The model boundary conditions are "open" or "unbound" in each direction. They are implemented thanks to perfectly matched layer (PML) [115]. This PML layer absorbs the electromagnetic (EM) waves without reflection. The nonuniform hexahedral mesh size is material refined to $\lambda/10$ which results for the $50\mu\text{m}$ taper length in a model having 7 million mesh cells. Refractive index of SiO_2 is fixed at $n=1.46$, the surrounding upper medium is air ($n=1$) and the silicon waveguide is modeled with a dispersive refractive index taken from D. E. Aspnes and J. B. Theeten [2] which is fitted with a second order polynomial curve. The length of the taper is swept from $1\mu\text{m}$ to $50\mu\text{m}$. The results show that for tapers longer than $10\mu\text{m}$ very low losses from $1.2\mu\text{m}$ to $1450\mu\text{m}$ should be expected. For longer wavelengths the taper becomes a bit lossy. The worst transmission is expected at $1.7\mu\text{m}$ wavelength and would be around 85% (-0.7dB).

Several researchers reported higher experimental losses for taper transmission which are probably due to the side roughness of the fabricated waveguide. As our calculation did not include any side wall roughness, we opted for $50\mu\text{m}$ long tapers to be on the safe side. This roughness model adaptation can only be done once the whole fabrication process is well known and repeatable.

2.4.1.4 Silicon wire waveguide bends

Waveguide bends are prone to losses if they have a too small radius compared to their effective index of refraction. Unperturbed light travels always on a straight path, thus to bend its

propagation, one need to reflect it on a surface, for example a mirror. In a waveguide, the light should be continuously totally reflected on the waveguide core surfaces. If the waveguide is bent, it changes the angle at which the light hits the waveguide walls and for small bend radiuses it might happen that the critical angle condition is not anymore satisfied and light escapes the waveguide. An analytical formula has been developed by Marcatili and Miller [116] to express the radiation losses as function of the radius in the case of a 2D problem. In the case of silicon wire waveguides, their large Δn allows them to have a bend radius as small as $5\mu\text{m}$ without having too much losses.

Another source of radiation losses comes from the fact that the transverse electric (TE) mode profile of a straight waveguide is different from the TE mode profile in a bent waveguide. This mode profile mismatch induces that a part of the waveguide mode energy is lost in radiation modes of the structure at the interface between straight and curved waveguide. The calculation of the 2D mode profiles of a circularly bent waveguide modes can be obtained by applying a conformal transformation to the refractive index profile [117]. The refractive index profile expressed as function of the radius r will be expressed after transformation as function of u as shown in equation 2.10. The structure with its new refractive index profile given by equation 2.11 can then be solved in cartesian coordinates with an eigenmode expansion solver [118].

$$u = R \ln\left(\frac{r}{R}\right) \quad (2.10)$$

$$n_t(u) = n(r) \exp \frac{u}{R} \quad (2.11)$$

Where R is the external radius of the waveguide bend.

Another method which is more heavy in calculation time is to use the time domain solver available with CST MWS to calculate the complete propagation of the mode inside the 90° bend. In Fig.2.18 we simulated the transmission losses in a wavelength range from 1200 to 1700nm for 90° waveguide bends of different radiuses ranging from 1 to $15\mu\text{m}$. Thanks to their high Δn , silicon wire waveguides can have bend radius as small as $5\mu\text{m}$ and still having a transmission of 99%.

2.4.2 Plasmonic slot waveguide

In this section we will analyse the plasmonic slot waveguide (PSW) modal characteristic and the coupling from the silicon wire waveguide to the PSW [74]. This metallic waveguide structure is very similar to a coplanar waveguide electrical transmission line already used nowadays in microwave frequency electronic devices. The slot mode can be understood like the excitation of a surface plasmon (SP) on the two perpendicular walls of the slot. Surface

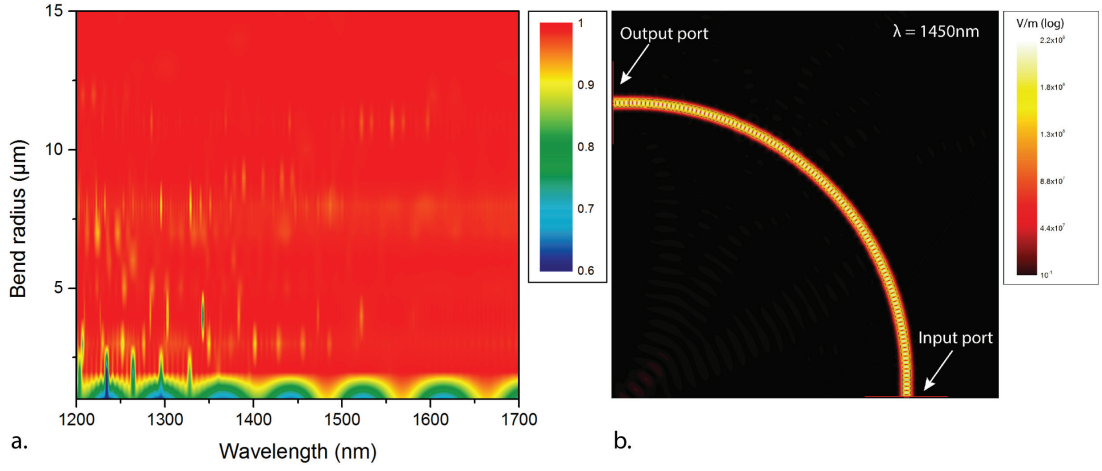


Figure 2.18 – a) Transmission from 1200nm to 1700nm of 2D silicon waveguides of 450nm width in air having bend radius from 1 to 15 μ m. b) $|E|$ -field for a 15 μ m radius bend at $\lambda=1.5\mu$ m.

plasmons can only be excited with a transverse magnetic (TM) field with respect to the excited surface. Therefore, the mode in the silicon waveguide must be transverse electric with respect to the surface of the chip. Moreover, it is desired to strongly confine and enhance the electric field in the slot that is created by the two metallic pads. As the PSWC is excited by a dielectric waveguide, we need to perform a modal analysis of the dielectric waveguide itself and of the coupled system i.e. the dielectric waveguide coupled to the plasmonic slot waveguide to optimize it. We assumed that the plasmonic cavity is excited by a single q-TE mode travelling in a silicon wire waveguide at wavelengths from 1200nm to 1700nm. Transverse electric is the case where the polarization of the electric field vector is perpendicular to the x,z-plane like in Fig. 2.22(a). From coupled-mode theory, a mode analysis of the uncoupled waveguide is studied to describe the coupled waveguide, as suggested by Berini [119]. We calculated the uncoupled and coupled modes with the 2D port mode solver of CST MWS.

2.4.2.1 Plasmonic slot waveguide modes

First, we investigated the PSW propagating mode. This mode is the 3D counterpart of the 2D metal-insulator-metal (MIM) waveguide, which was analytically derived by Economou [67]. Recently, there has been a growing interest in these type of waveguides because of their ability to confine the light in sub-wavelength volumes and to have low bending losses [75, 120]. They are good candidates for ultra dense on-chip optical data transmission. Different implementations of PSW are possible and depend on the used fabrication technology. These different plasmonic waveguides could be for example: a channel plasmonic waveguide [121], a periodic slit waveguide [122] or a plasmonic slot waveguide [73]. For planar fabrication the PSW is a good candidate allowing easy integration and also coupling to larger dielectric waveguides. As we show in Fig. 2.19, the PSW can sustain two propagating modes.

In the inset of Fig. 2.19, we can see the absolute electric field amplitude for the two propagating

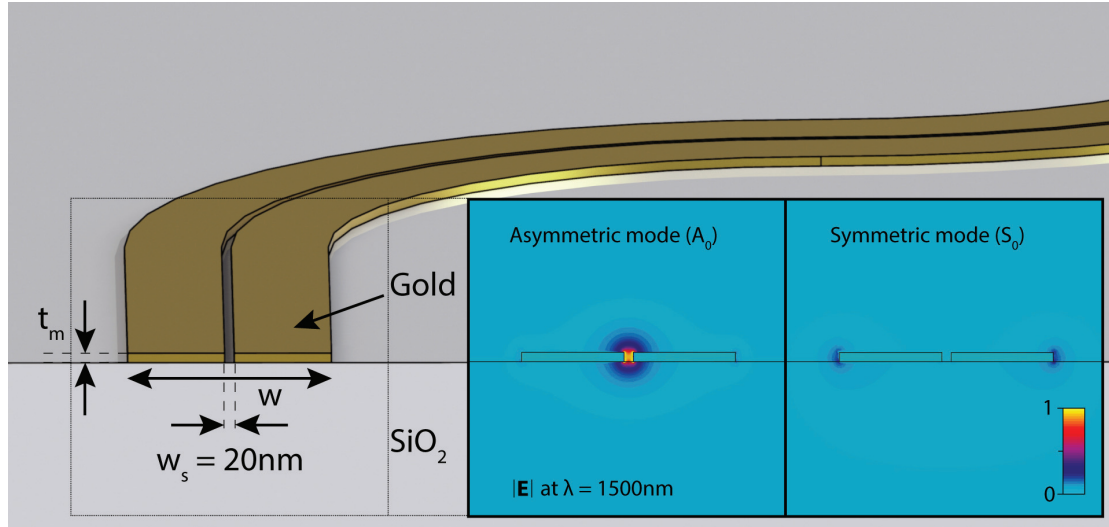


Figure 2.19 – Drawing of a typical PSW with metal thickness of 20nm (t_s), width of 450nm (w) and slot width of 20nm (w_s) lying on top of a silicon dioxide substrate and surrounded by air. The two figure insets show the absolute electric field amplitude at $\lambda = 1500\text{nm}$ of the two propagating modes A_0 and S_0 .

modes. The fundamental mode (A_0) which we call the slot mode is an asymmetric mode and its electric field is confined inside the slot which is surrounded by metal on both sides. The second mode (S_0) is a symmetric mode which is resulting from the excitation of surface plasmons on both external metal surfaces [72]. The propagation losses of the PSW modes are very different. On one hand the asymmetric mode has a shorter propagation length than the symmetric mode, but on the other hand, the asymmetric mode has a better ability to confine the electric field to nanometer sized volumes. Here, the A_0 and S_0 modes, shown in Fig. 2.20, have theoretical propagation lengths of 10 and $20\mu\text{m}$ at $\lambda = 1500\text{nm}$. Even if these propagation lengths are very small, they are sufficient for nanometer sized optical circuits. In Fig. 2.20 we show the dispersion curve of the PSW depicted in Fig. 2.19 calculated with the frequency domain port mode solver of CST MWS which is taking into account the lossy behaviour of the metal. We chose gold as the metal and we chose Johnson & Christy [3] data for its dielectric properties. We show two sets of dispersion curves, one for a slot width of 50nm and the other for a slot width of 20nm. The gold thickness is fixed at 20nm (t_s) and the PSW width is fixed at 450nm (w). We see the broadband behaviour of these plasmonic modes and the fact that the S_0 mode is not altered if the slot width is reduced from 50 to 20nm. Likewise, the A_0 mode dispersion curve is pushed away from the light line which can influence the further coupling to a silicon waveguide. Its propagation constant increases when the slot width decreases. This is directly linked with its increasing propagation losses when the slot becomes smaller. When the propagation constant increases, it means that the angle at which the light is bouncing back and forth between the two metal interfaces is becoming larger. Thus a larger part of the electric field is located inside the metal which is lossy. As there is no cut-off, we can reduce the size of the slot to the limits of today's fabrication techniques as long as the losses stay

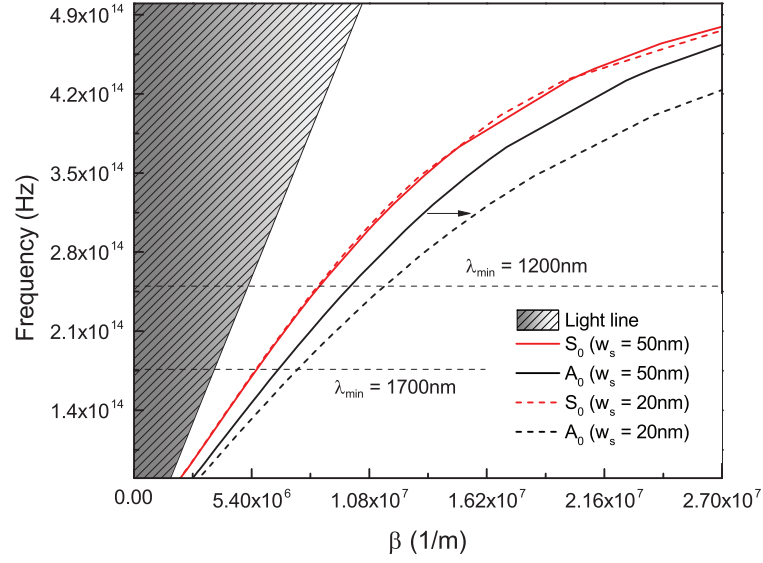


Figure 2.20 – Dispersion diagram of the PSW symmetric (S_0) and asymmetric (A_0) modes depicted in Fig. 2.19 showing the influence of the slot width reduction on the A_0 slot mode propagation constant.

acceptable.

2.4.2.2 Coupling of silicon wire waveguide to Plasmonic slot waveguide (PSW)

In Fig.2.21 we show the different dispersion curves for the silicon wire waveguide, the PSW and the two coupled hybrid modes. The dispersion curve of the silicon waveguide crosses the dispersion curve of the PSW. At this intersection, the propagation constants are equal and both guided waves are phase matched. This is a condition which needs to be satisfied in order to be able to excite one guided wave with the other one. In the coupled system, we see a splitting resulting in two hybrid modes having different propagation constants at a single frequency. Both hybrid modes are excited in the coupled system and propagates simultaneously. In Fig.2.22 we show the y-component of the electric field amplitude in a cross section of the waveguide at a wavelength of 1500nm. The amplitude scale bar is constant over all four figures. The Fig.2.22(a) is representing the q-TE mode of the silicon waveguide. The Fig.2.22(b) is representing the PSW mode with the waveguide core material replaced by SiO_2 . We see that the field is almost exclusively confined in the slot between the two metallic pads. This is the region of interest for our sensor where a change of refractive index should perturb the coupling and the resonance of the system. Figure 2.22(c) and (d) show the resulting mode field distribution of the coupled system, (c) the even hybrid mode and (d) the odd hybrid mode respectively. Another condition which needs to be satisfied for coupling is the mode field overlap. If both waveguides are separated by a too large distance, one cannot excite the other one. At least a part of the field must overlap the other field in order to excite the coupled system. This is where the SiO_2 spacer thickness comes into play. The larger the spacer is, the

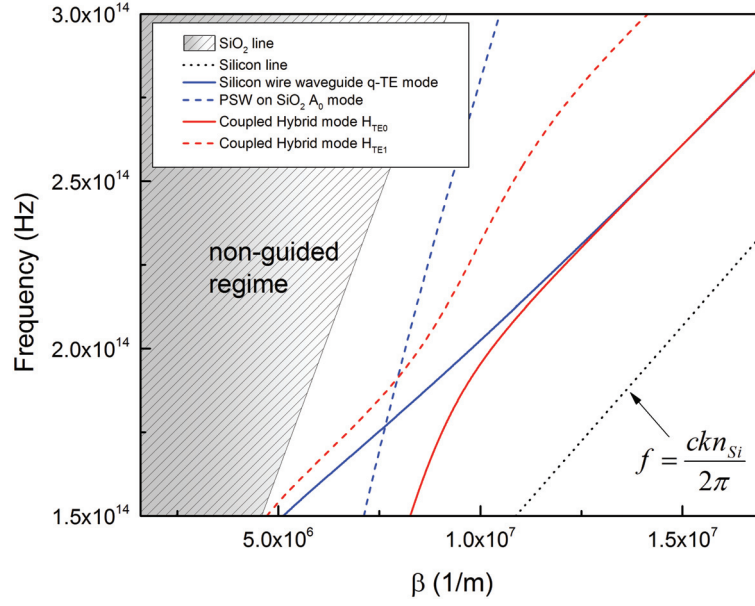


Figure 2.21 – Dispersion diagram of uncoupled and coupled q-TE mode of the silicon wire waveguide and A_0 PSW mode.

less coupled will the system be and vice versa.

2.4.2.3 Coupling length

Light coupling from the dielectric waveguide to the PSW plays an important role in the performance of our sensor. The proposed cavity is in fact a PSW with a length of only 600 nm, which is shorter than the coupling length between the silicon waveguide and the PSW. Similar to two coupled dielectric waveguides, the two hybrid modes H_{TE_0} and H_{TE_1} of the described structures have two different propagation constants $\beta_{H_{TE_0}}$ and $\beta_{H_{TE_1}}$, which lead to interferences during their propagation. Consequently for an infinitely long PSW, an alternating energy transfer from the dielectric waveguide to the PSW and vice versa is observed. The coupling length is equal to [123]:

$$L_c = \frac{\pi}{\beta_{H_{TE_0}} - \beta_{H_{TE_1}}} \quad (2.12)$$

L_c corresponds to the length where a total transfer of the energy from one waveguide to the other one occurs. For the given structure in Fig. 2.23, at $\lambda = 1.6 \mu m$ the effective index is 2.54 and 2.09 for the H_{TE_0} and H_{TE_1} modes, respectively. These values result in a coupling length of approximately $1.78 \mu m$. The coupling length of the proposed structure is more than an order of magnitude smaller than that of a conventional silicon wire waveguide directional coupler [124]. To reduce the coupling length, the difference between the propagation constants of

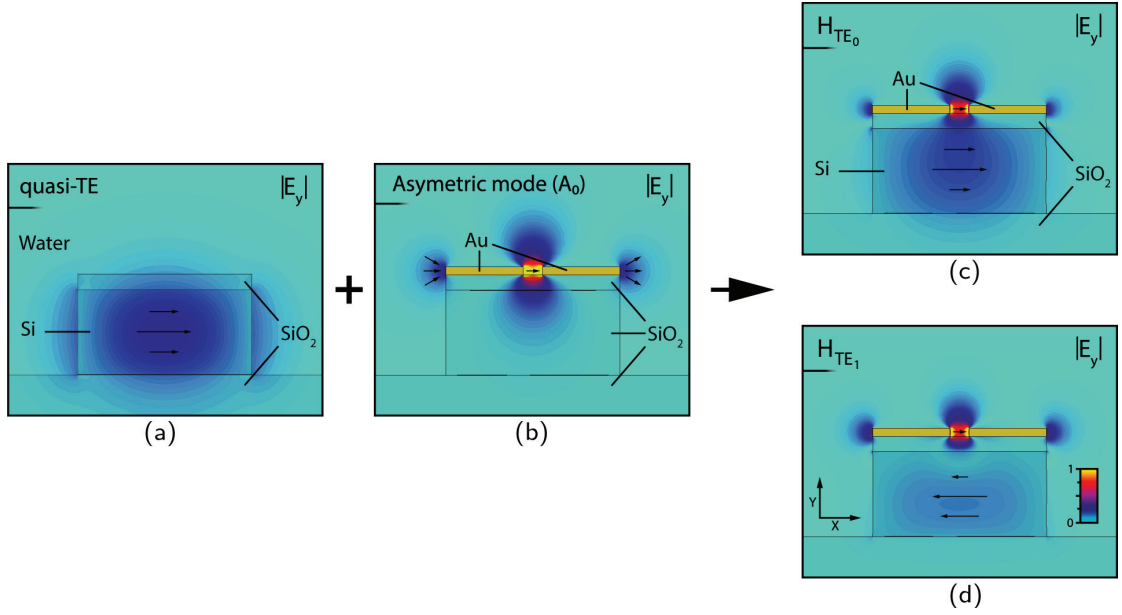


Figure 2.22 – 2D E_y -field amplitude component at $\lambda=1500\text{nm}$. a) q-TE mode of the silicon wire waveguide with an SiO_2 top layer (spacer) ($t_s = 40\text{nm}$, $w = 450\text{nm}$). b) Asymmetric mode (A_0) of the PSW with the waveguide core material replaced by SiO_2 ($t_m = 20\text{nm}$). c) Coupled hybrid even mode (H_{TE_0}) of the PSW and the silicon wire waveguide. d) Coupled hybrid odd mode (H_{TE_1}) of the PSW and the silicon wire waveguide.

both hybrid modes need to be increased. In addition to bio-sensing, this extremely short coupling length is of great interest to save as much space as possible on future photonics integrated interconnects and circuits. The propagation constants and the field distributions of the shown modes are calculated using the CST MWS 2D mode solver and the coupling length is calculated with the use of the Eq. 2.12. The coupling length depends strongly on the geometrical parameters of the structure. When increasing the spacer thickness, the interaction of the evanescent tails of both modes is reduced and thus the coupling length is increased. However, shrinking the size of the silicon wire waveguide will shorten the coupling length because the evanescent tail of the silicon wire waveguide mode will interact more with the PSW mode.

In order to confirm the coupling length calculations according to Eq. 2.12, a rigorous calculation based on the 3D frequency-domain solver of CST MWS has been done. Figure 2.23(a) shows the distribution of the E_x component of the electric field for a structure excited from the left side by the q-TE mode of the silicon waveguide at $1.6\mu\text{m}$ wavelength. After one micrometer the mode starts to couple into an infinitely long PSW. The mode of the silicon waveguide is coupled into the metallic slot after a coupling length of about $1.78\mu\text{m}$. At L_c , the modal interference between the two hybrid modes creates a constructive interference located in the plasmonic slot waveguide. At $2 \times L_c$ the constructive interference is respectively located inside the silicon waveguide. The obtained L_c value shows good agreement with the mode coupling analysis described previously. This confirms that the device works in the weak cou-

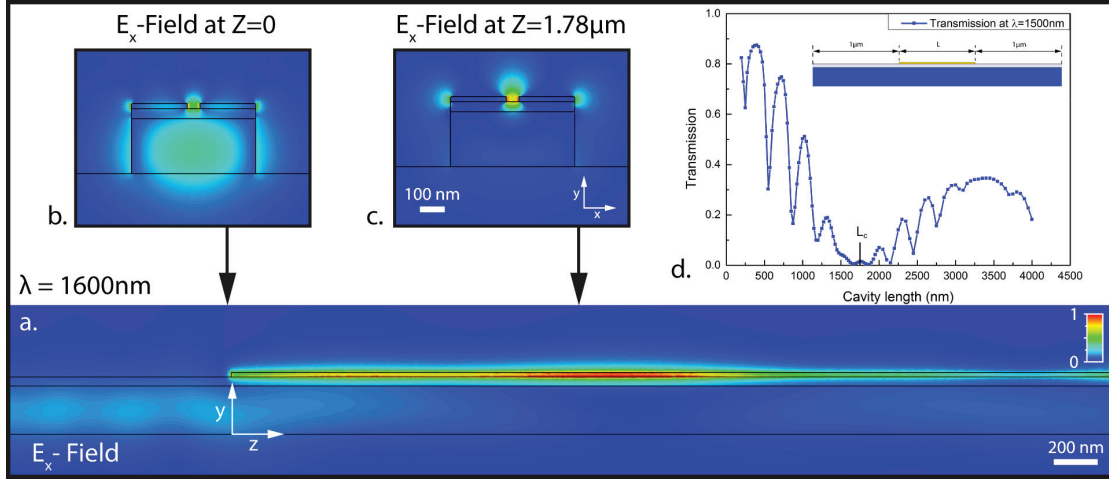


Figure 2.23 – (a): E_y -field amplitude showing the coupling between the dielectric waveguide and the metallic slot calculated with 3D frequency-domain solver of CST MWS. (b) and (c): E_y -field amplitude of the 2D mode profile at $z = 0$ and $z = 1.78 \mu\text{m}$. (d): Transmission of the excited cavity as function of the cavity length at $\lambda = 1500 \text{ nm}$.

pling regime. The inset of Figs. 2.23(b) and (c) shows the mode field distribution at $z = 0$ and $z = L_c$ respectively. At $z = 0$ light is essentially confined in the silicon core while at L_c light is confined in the sub-wavelength-sized slot. Figure 4(d) shows the transmission as a function of the cavity length at the wavelength of $1.5 \mu\text{m}$. The inset of Fig. 2.23(d) shows a sketch of the structure which is composed by an input and an output silicon waveguide of $1 \mu\text{m}$ length and the PSWC of length L in the middle. The metallic slot has a finite length L which is varied to observe its impact on transmission. Two types of oscillations appear in the transmission versus cavity length plot. The one with the shorter period corresponds to the cavity resonance due to the reflection of the light at both ends of the slot. The one with a longer period originates from the interference between the two propagating modes which have different propagation constants ($\beta_{H_{TE_0}}$ and $\beta_{H_{TE_1}}$). The coupling length of the structure can thus be retrieved from the transmission spectrum. At the coupling length, minimum of transmission occurs. In our case, L_c equals to $1.75 \mu\text{m}$ which agrees with the result of Eq. 2.12 and the rigorous simulation. Another mechanism affecting the coupling is the change of the refractive index of the outer medium. The silicon waveguide mode effective index depends on the outer medium's refractive index, thus the coupling condition to the PSWC are changing. As this coupling perturbation is relatively small it will be neglected in the next section when calculating the bulk sensitivity of the PSWC.

2.4.3 Plasmonic slot waveguide cavity resonances

Based on the latter investigations, we will describe a standard sensor geometry to which we will always refer in the following sections. The integrated plasmonic cavity is depicted in Fig. 2.24 and has a length $L = 600 \text{ nm}$, a thickness $t_m = 20 \text{ nm}$ and a slot width $w_s = 50 \text{ nm}$. It lays on

top of a silicon oxide spacer layer of thickness $t_s = 40\text{nm}$ and a silicon waveguide of thickness $t_{wg} = 220\text{nm}$. The silicon waveguide is designed in order to support only two modes in the near infrared wavelength range between 1200 nm and 1700 nm, therefore it has a width $w = 450\text{nm}$. Based on the field profiles, the fundamental q-TE mode of the silicon waveguide is the only mode being able to excite the PSWC modes A_0 and S_0 contrarily to the fundamental q-TM mode which would excite other unwanted longitudinal modes. The silicon waveguide is used to guide light from the source to the cavity and from the cavity back into the waveguide to the detector. The aim of the architecture is to be able to inject a defined spectrum in the waveguide and look for a specific signature of this spectrum after it excites the PSWC. If the PSWC is excited, the spectrum will show a resonance peak at the output waveguide. The surrounding medium is monitored by tracking this resonance. A change in refractive index of the outer medium is seen in the output spectrum as a shift of the resonance peak.

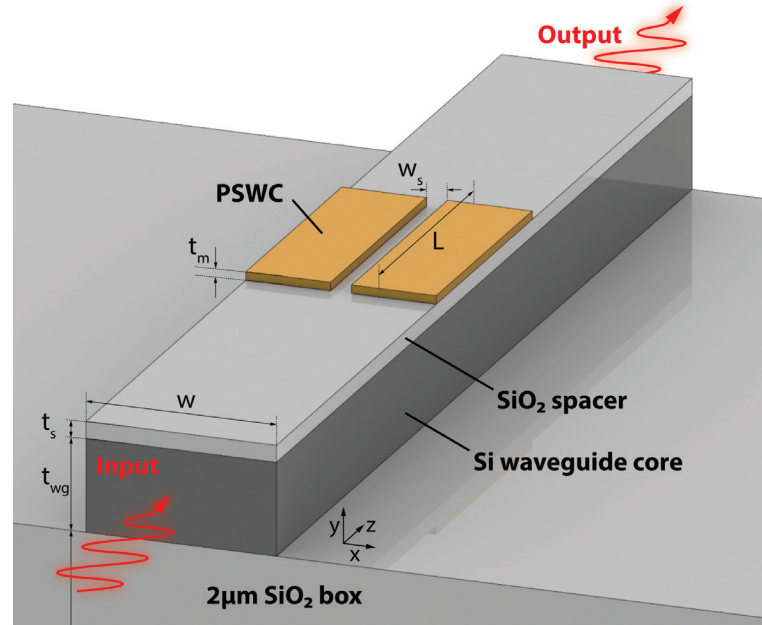


Figure 2.24 – Drawing of the hybrid photonic-plasmonic cavity. On top of a single crystal silicon waveguide there is a PSWC which is separated from it by a silicon oxide film. Invariant spatial parameters of this structure are $t_{wg} = 220\text{nm}$, $w = 450\text{nm}$ and $w_s = 50\text{nm}$. Variable spatial parameters of the PSWC are $L = 600\text{nm}$, $t_s = 40\text{nm}$ and $t_m = 20\text{nm}$.

To describe the behaviour of the PSWC we will rely on the basic model of a Fabry-Pérot resonator. Equation 2.13 expresses the quality factor (Q-factor) of a Fabry-Pérot resonator as function of the optical path difference (OPD), the finesse (\mathcal{F}) and the wavelength (λ).

$$Q = \frac{OPD}{\lambda} \mathcal{F} \quad (2.13)$$

Where $\mathcal{F} \cong \frac{\pi\sqrt{R}}{1-R}$ is the finesse for a lossless resonator and $OPD = 2n_{eff}L$ is equal to twice the effective cavity length. This equation can be used for any type of optical resonator. In the case of a lossless resonator, equation 2.13 is composed of three independent terms. The first one is the OPD which only dependent on the length of the cavity. The second one is the wavelength. And the third one is the finesse (\mathcal{F}) which is determined by the reflectivity of the mirrors and therefore independent of the cavity length (L). When absorption losses are present during the round trip of the light inside the cavity, the finesse starts to become dependent of the cavity length. In a recent article, Martin Suter and Peter Dietiker have derived the exact finesse [125]. It is here given by equation 2.14.

$$\mathcal{F} = \frac{\pi}{\alpha L - \ln R} \quad (2.14)$$

We see from equation 2.14 that it becomes less straight forward to predict the behaviour of the quality factor of a resonator, especially if the latter is based on lossy plasmonic waveguide. To have an idea of the reflectivity R and the absorption coefficient α at $\lambda = 1550\text{nm}$, we did some simulation of a PSW made out of gold and having the following parameters: $w = 450\text{nm}$, $w_s = 50\text{nm}$ and $t_m = 20\text{nm}$. In the simulation the PSW was surrounded by vacuum. Here we give some numbers, which were found from this simulations done in ideal conditions: $R \sim 0.14$ and $\alpha \sim 0.15\mu\text{m}^{-1}$ at $\lambda = 1450\text{nm}$. The resulting finesse for a 600nm long cavity calculated by using equation 2.14 is approximately 1.53. When calculating the finesse with the lossless finesse we get a lower value of 1.36. When the PSW is isolated like in this case, its effective index is equal to 1.7 at $\lambda = 1450\text{nm}$. When the PSW is coupled to the silicon waveguide, the effective index of the H_{TE_0} mode equals 2.54 and the one of the H_{TE_1} mode equals 2.09 like already reported in section 2.4.2.3 on page 42. In the following sections, we will analyse the obtained simulation results based on the latter equation since we are interested in maximizing the Q-factor of the cavity.

2.4.3.1 Influence of the cavity length and the coupling strength on the Fabry-Pérot resonance of the PSWC

The Fabry-Pérot resonance transmission spectrum is measured at the output of the silicon waveguide and depends on its geometrical parameters: the cavity length (L), the metal thickness (t_m), the spacer thickness (t_s) and the slot width (w_s), shown in Fig. 2.24. In order to have an idea of the influence of these parameters on the resonant optical properties of the device, we primarily had to calculate the transmission spectrum for different lengths of the PSWC. Then we investigated the impact of the coupling changes on the resonance properties by changing the oxide spacer thickness (t_s). We performed our numerical study with the commercial software CST MWS using frequency and time domain calculations. A non-uniform three dimensional hexahedral meshing is applied in x, y, and z directions in order to define the structure. The mesh size varies continuously between 2nm for the metallic plasmonic cavity

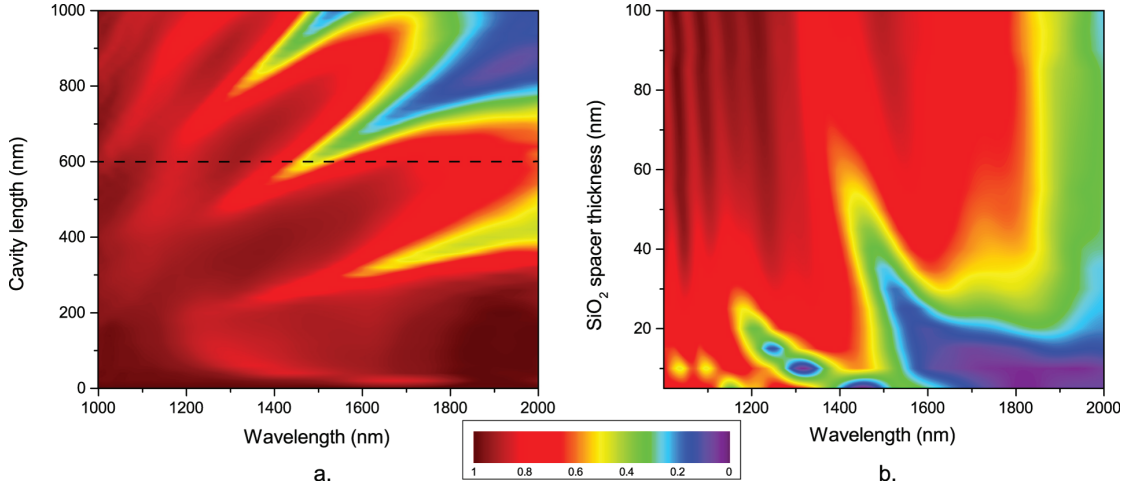


Figure 2.25 – Transmission spectra of a PSWC with standard geometrical parameters (see paragraph 2.4.3 on page 44). a) Dependence of the transmission spectra as function of the cavity length (L). b) Dependence of the transmission spectra as function of the spacer thickness (t_s). Both figures exhibit typical Fabry-Pérot resonance peaks.

and 26nm for the silicon waveguide over a bounding box of $2.3\mu\text{m}$ (X) \times $2\mu\text{m}$ (Y) \times $2.7\mu\text{m}$ (Z) containing 6 billion of mesh cells. To have good results with the time domain simulation, one must follow a rule of thumb that determines that the mesh size in metals should be at least the penetration depth divided by 5 and for dielectrics it should be at least λ over 10. The temporal step for the time domain solver is set to $4.5 \times 10^{-18}\text{s}$. We used a PML of 8 layers as an artificial absorbing boundary. The gold permittivity is described by a 4th-order polynomial fit of Johnson and Christy data [3]. To reduce computation time, we used a distributed computing feature of the software package.

Fig. 2.25(a) demonstrates transmission versus the cavity length (L). It shows multiple transmission peaks that appear at wavelengths corresponding to the longitudinal Fabry-Pérot resonances of the cavity. As expected, the resonance positions strongly depend on the cavity length. The resonance peaks shift to a larger wavelength (red shift) as the cavity length increases. In the bandwidth from $\lambda = 1200\text{nm}$ to 1700nm , the fundamental resonance disappears for cavity lengths smaller than 250 nm. This is due to phase-matching which cannot be obtained for cavity lengths smaller than $\lambda_{eff}/2$, where λ_{eff} is the effective wavelength of the fundamental guided mode inside the PSW. Moreover, below 1200nm the silicon waveguide becomes multi-mode and the resonance starts to be affected by other modes. Fig. 2.25(a) shows that higher order resonances appear for longer cavities. The dashed black line corresponds to the cavity length where the first harmonic of the resonance is located at around $\lambda = 1.5\mu\text{m}$. This is the targeted resonance position which is convenient for future experimental measurements.

Fig. 2.25(b) represents the transmission as function of the silicon oxide spacer thickness. The resonant wavelength position of the first harmonic occurs at around $\lambda = 1550\text{ nm}$ and

remains almost independent of the spacer thickness changes. The spacer thickness, which separates the PSWC and the waveguide, affects the coupling efficiency between the mode of the waveguide and the cavity mode. When the system is less coupled, the effective refractive index of the H_{TE_0} mode will decrease. The resonance position will therefore be blue shifted to satisfy the phase-matching at resonance. It is also to be noted that due to the presence of the spacer all along the silicon waveguide, changing the spacer thickness affects slightly the effective index of the guided mode present in the silicon waveguide which will then affect the coupling strength. Nevertheless, this perturbation is minimal in comparison to the change of effective index of the coupled hybrid mode.

Due to fabrication restrictions, a slot width of $w_s = 50\text{nm}$ was chosen for our design. From these calculations, we opted for the following parameters: $t_m = 20\text{nm}$, $t_s = 50\text{nm}$ and $L = 600\text{nm}$. Using the latter geometrical parameters the first harmonic resonance was excited at the wavelength of around $\lambda = 1.5\mu\text{m}$ and had a high extinction ratio of about 3 which made the resonance position measurable.

2.4.3.2 Influence of the slot width and the gold thickness on the resonance of the PSWC

As discussed in paragraph 2.4.2.1 on page 39, the propagation length of the PSW is changing with the slot width. If the propagation length changes, this means that the waveguide becomes more or less lossy. We expected this to influence the Q-factor of the Fabry-Pérot resonance of the coupled PSWC. However, when the propagation constant increases, the impedance of the slot mode is decreasing, this will increase the reflectance at the slot extremities and increase the Q-factor of our cavity [126]. Both behaviours are counter acting against each other. It is thus very difficult to forecast a result. If one looks only at the coupling, when the slot width is reduced, the mode overlap with the silicon waveguide mode is decreasing, leading to weaker coupling. We simulated these effects on a coupled PSWC of standard dimension (see paragraph 2.4.3 on page 44).

In Fig. 2.26(a) we simulated the transmission spectra for a slot width ranging from 4 to 100nm. The results show that for a slot width larger than 30nm the resonance position stays located at the same wavelength. Only the maximum attenuation at resonance position changes. For a slot width below 30nm the resonance position is red-shifting and at slot width of 10nm, a second resonance can be seen around 1200nm. As it is very difficult to fabricate slots which are smaller than 40nm, we fixed the slot width of our design at 50nm. This also gives us a better repeatability in the measurement of our device.

In Fig. 2.26(b) we simulated the transmission spectra for a slot width of 50nm and a thickness of the gold layer ranging from 10 to 50nm. We clearly saw that above a gold layer thickness of 25nm the silicon waveguide is not able to couple to the cavity anymore and the resonance is lost. Thus we used a thickness of 20nm to fabricate our device.

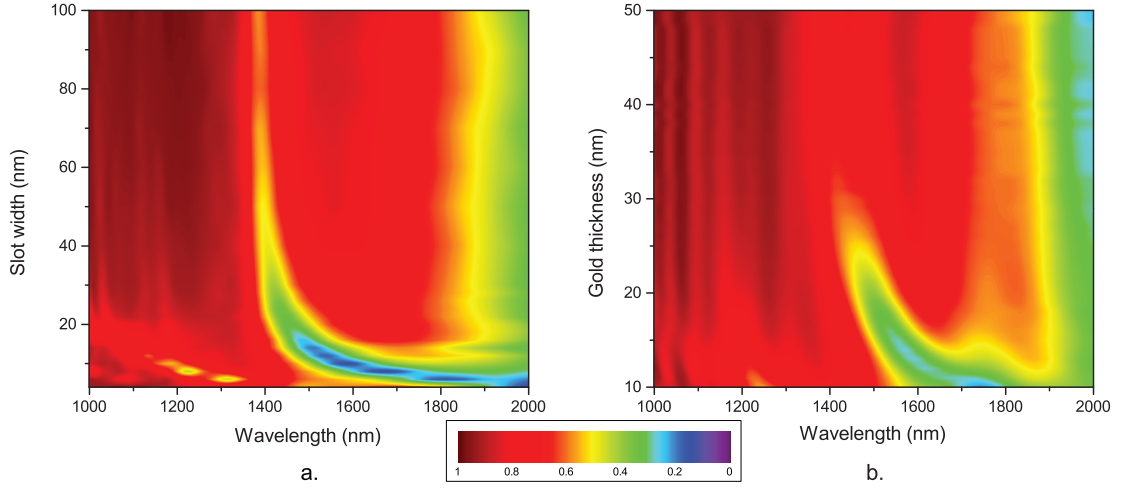


Figure 2.26 – Transmission spectra of a PSWC with standard geometrical parameters (see paragraph 2.4.3 on page 44). a) Dependence of the transmission spectra as function of the slot width (w_s). b) Dependence of the transmission spectra as function of the gold thickness (t_s). Both figures exhibit typical Fabry-Pérot resonance peaks.

2.4.3.3 Influence of the slot lateral position with regard to the silicon waveguide

Due to doubts about the future alignment accuracy in the fabrication process, we needed to know if the resonance would be affected if the PSWC was not perfectly aligned to the silicon waveguide. In the case of misalignment of the cavity, the mode overlap between the q-TE mode of the silicon waveguide and the H_{TE_0} slot mode would be different. In Fig. 2.27 we show the influence of the slot lateral misalignment on the transmission spectrum. We see that a stronger resonance appears when the slot is slightly misaligned from its central position. It is not the behaviour we expected. As we observed the evolution of the field in the time domain, we saw that the two fundamental modes of the PSWC were excited. As we showed in section 2.4.2 on page 38 the asymmetric (A_0) and the symmetric (S_0) mode have different propagation constants. It is therefore possible to change the propagation constants of the S_0 mode in order to match the one of the A_0 mode so that both enter in resonance for the same cavity shape. This is partially happening when the slot is misaligned and this explains why we see a stronger resonance with a misaligned cavity.

2.4.4 Field enhancement in the slot of the PSWC

The ability to detect small molecules in the vicinity of the PSWC is proportional to its field confinement and thus enhancement. Equation 2.15 expresses the average normalized electric field intensity enhancement due to the presence of the PSWC. It is obtained by the ratio of — the integration of $|\mathbf{E}|^2$ over a volume V including the PSWC — over the same integration calculated in the same volume but without the effect of the metallic cavity. The integration volume V is a box centered on the PSWC with dimensions: $[t_m + 40\text{nm}] (X) \times [w + 40\text{nm}] (Y) \times$

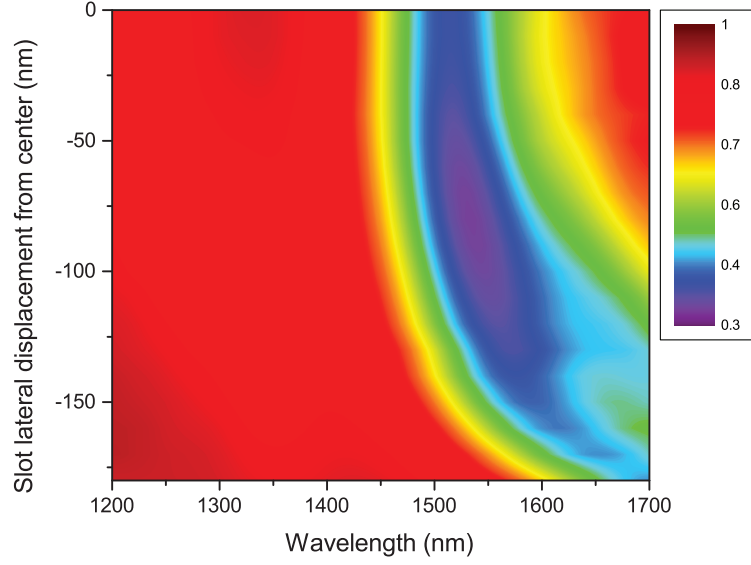


Figure 2.27 – Transmission spectra dependence upon different slot lateral misalignments for a PSWC with standard geometrical parameters (see paragraph 2.4.3 on page 44). A stronger resonance for a 75nm misalignment can be observed.

$[L + 40nm](Z)$ (see Fig. 2.24). We used the 3D time domain solver to obtain the following results. The solver and structure parameters are identical as the one described in the last paragraph.

$$FE = \frac{\iiint_V |\mathbf{E}_{cav}|^2 dx dy dz}{\iiint_V |\mathbf{E}_{wg}|^2 dx dy dz} \quad (2.15)$$

In Fig. 2.28(a), we display the averaged field enhancement of a gold PSWC of 600 nm length (in red) as a function of the wavelength compared to its transmission spectrum (in blue). The maximum field intensity enhancement occurs at the longitudinal resonance of the H_{TE_0} guided mode. In Fig. 2.28(b) the spatial electric field intensity enhancement is shown on a plane cutting the PSWC at half of its thickness. The excitations mode of the silicon wire waveguide travels along the z-axis (from negative to positive values). It is observed that light is essentially confined between the two metallic interfaces. This is due to the excitation of a guided plasmonic slot mode inside the cavity. Nevertheless, one can see some higher field intensities at the outer side of the cavity, which are mainly due to the presence of the H_{TE_1} mode which is not in resonance at this wavelength. The maximum local field enhancement observed is around 8000 which is of course way larger than the averaged field enhancement. We see that the standing wave inside the slot is terminated by anti-nodes (maximum of field magnitude) at the slot waveguide ends. We would normally expect a node of the standing wave (minimum of field magnitude) at the mirror surface for a classical Fabry-Pérot resonator

made out of two metallic or dielectric parallel mirrors. This is because the effective index of the resonator medium is larger than the effective index outside of the cavity. The same behaviour is observed in wind musical instruments for pressure waves[127].

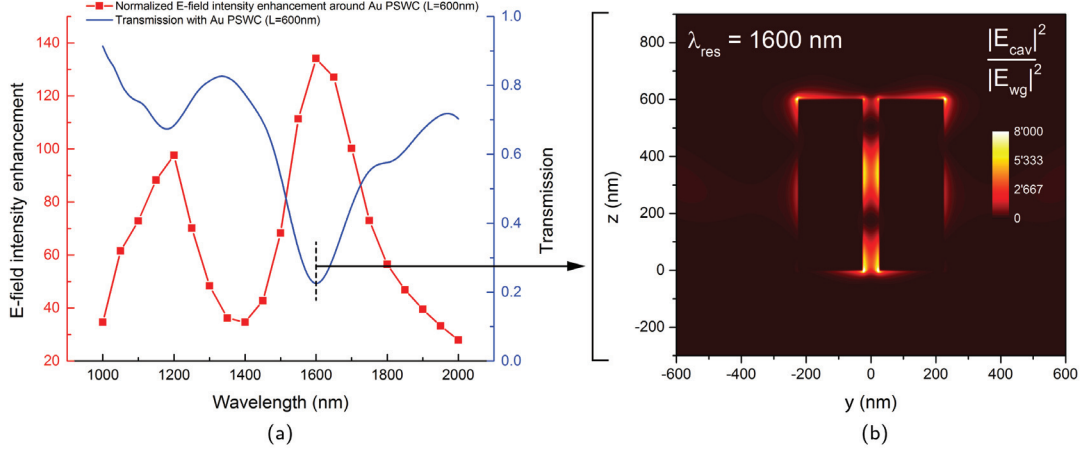


Figure 2.28 – a) Transmission spectrum compared to the averaged electric field enhancement around a gold PSWC ($t_s = 40$ nm, $w = 450$ nm, $t_m = 20$ nm, $w_s = 50$ nm, $L = 600$ nm). b) 2D normalized $|E|^2$ -field distribution at half the metal thickness of the plasmonic cavity at resonance frequency.

2.4.4.1 Influence of different metals and different cavity lengths on the PSWC resonance

As explained in the section 2.1.1 on page 5, the main problem of plasmons is their lossy behaviour. Using plasmonic waveguides to make a Fabry-Pérot resonator is certainly not an optimal way to achieve a high Q-factor of the resonance. The Q-factor of a resonator is the ratio of the stored energy divided by the energy loss per cycle. It can also be expressed as the frequency (ν_r) to bandwidth ($\Delta\nu$) ratio of the resonance spectrum $Q = \nu_r / \Delta\nu$, and is directly proportional to the losses per unit length of the travelling wave inside the resonator and to coupling. [128]. It is therefore possible to enhance the Q-factor by choosing a metal with a smaller imaginary part of its dielectric constant to excite surface plasmons. In this section, we will show simulated resonance spectra for 300 nm and 600 nm long cavities made out of three different metals – silver, gold and aluminium – sustaining surface plasmon polaritons (SPPs) in the used wavelength range between 1200 and 1700 nm. Fig. 2.29 shows the real and imaginary parts of the wavelength dependent dielectric function of the three investigated metals taken from Johnson [3] and Palik [4].

In Fig. 2.30(a) we can see the transmission spectra for a "standard" PSWC of 300 nm length. The first thing to point out is the Q-factor of each resonance. As expected, the silver which has the lowest losses exhibit the highest Q-factor. When comparing the corresponding field enhancement shown in Fig. 2.30(c), we first see that the maximum field enhancement is located at the resonance wavelength which makes sense as light is stored in the cavity. We can

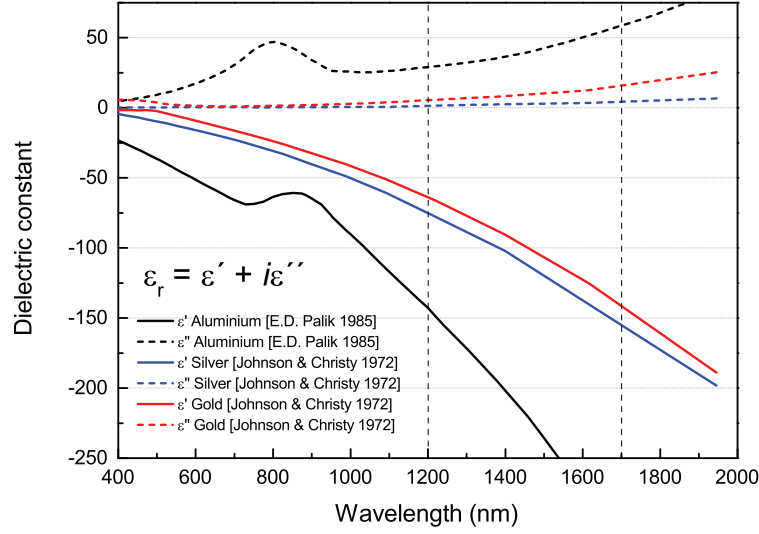


Figure 2.29 – Real and imaginary parts of the dielectric function of silver [3], gold [3] and silver[4].

also see that the maximum field enhancement is inversely proportional to the metal losses. For the longer cavity of 600nm length, we see in Fig. 2.30(b) that the Q-factor of the resonance is higher for all three metals. If referring to equation 2.13, we can explain this as follows. The finesse is reduced because of the longer length of the cavity but the OPD is twice larger. In that case, the increase in OPD is larger than the decrease of the finesse. Logically, we see the field enhancement in Fig. 2.30(d) increasing as well. We note that the positions of the resonances in Fig. 2.30(a) and (b) are not exactly at the same position. This is an effect coming from the strongly dispersive behaviour of the PSW.

2.4.5 Sensitivity to refractive index of the coupled system

The PSWC is meant to be a spatially localized refractive index sensor which could be multiplexed on a 2D surface. We therefore performed a sensitivity study of the structure with the three different metals used previously to find the relation between near-field intensity enhancement and detection of localized changes of refractive index. The bulk refractive index sensitivity is achieved by simulating the resonance peak shift ($\Delta\lambda$) obtained by the change of refractive index (Δn) of the whole medium around the PSWC. The sensitivity is defined as $S = \Delta\lambda/\Delta n$. To calculate the bulk sensitivity, two time domain simulations were performed with refractive index of the outer medium changing from 1.32 (water at 1500 nm) to 1.35 (acetone at 1500 nm). Likewise, the local sensitivity was obtained by simulating a change of the refractive index of only a thin layer of a couple of nanometer wrapped around the PSWC. It was shown in paragraph 2.4.3.1 on page 46 that changing the spacer thickness does not vary the resonant wavelength but significantly modifies the coupling between the waveguide and the plasmonic cavity. In order to keep the cavity as small as possible, we studied the sensitivity of the PSWC as a function of the spacer thickness for the three different metals: aluminium,

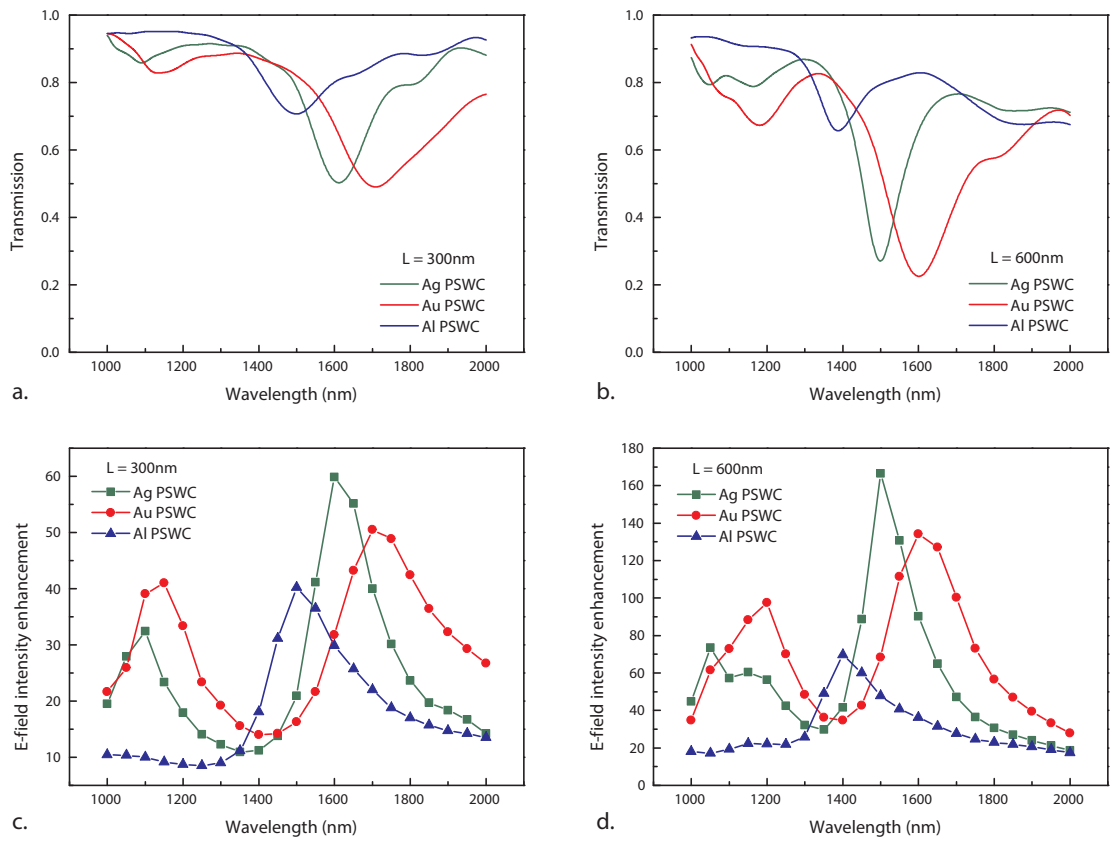


Figure 2.30 – a) and b) Transmission spectra for PSWC of 300nm and 600nm length (L) made out of silver, gold and aluminium. c) and d) Averaged electric field amplitude enhancement over a volume including the PSWC.

gold and silver. The dispersion of the different metals is described in Fig. 2.29.

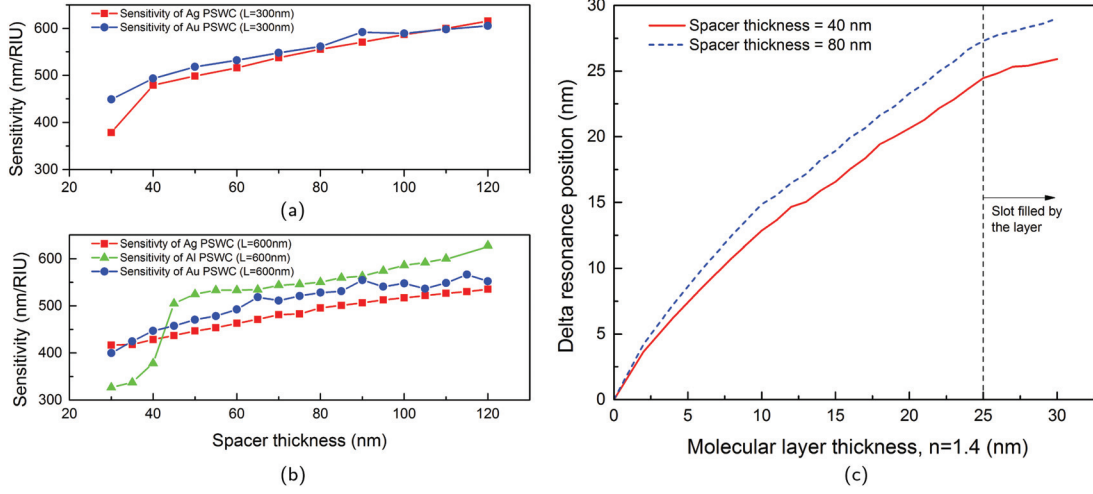


Figure 2.31 – (a): Bulk sensitivity for silver and gold PSWC of 300 nm length as function of the spacer thickness. (b): Bulk sensitivity for silver, gold and aluminium PSWC of 600 nm length as function of the spacer thickness. (c): Resonance wavelength shift of a 600 nm (L) long gold PSWC as a function of the thickness of a molecular layer of refractive index of 1.4 deposited on it.

Fig. 2.31(a) shows the bulk sensitivity as function of the spacer thickness for a 300nm long PSWC made out of silver or gold. Fig. 2.31(b) shows a similar result for a 600nm long PSWC made out of silver, gold or aluminium. The resonant wavelength of the PSWC on Figs. 2.31(a) and (b) are both around $\lambda_{res} = 1500\text{nm}$; thus the fundamental resonance is excited for the 300nm long PSWC, and the first harmonic is excited for the 600nm long PSWC. We note that on Fig. 2.31(a) the aluminium PSWC sensitivity is missing because the extinction ratio of the resonance is too small. On Figs. 2.31(a) and (b) we observe a general increase of the bulk sensitivity for all the three metals for increasing spacer thicknesses. For the silver PSWC in Fig. 2.31(a), the bulk sensitivity reaches up to 615nm/refractive index unit (RIU) for a spacer thickness of 120nm and a cavity length of 300nm. It shows that the fundamental resonance has a higher bulk sensitivity than the first-order resonance. Moreover, when using the fundamental resonance, the detection volume becomes smaller which is better for single molecule sensing at high concentration [30]. With increasing spacer thicknesses the fundamental resonance extinction ratio decreases and the tracking of the resonance becomes more difficult. The results of Figs. 2.31(a) and (b) show that the less coupled the system is, the stronger the resonance wavelength will be perturbed by a certain refractive index change of the bulk. However, for aluminum, even if the bulk sensitivity is higher, the Q-factor and the extinction ratio are smaller because of the high amount of loss in the aluminum; this strongly affects the detection limit of the sensor. Using silver for the cavity provides the highest Q-factor and thus the highest photon life time in the cavity and the highest local field enhancement.

The bulk sensitivity values obtained by our simulations are only 40% lower than the result

shown in [77] where a periodic array of PSWC is used on top of a slab waveguide which also has a 30 times larger interaction volume.

As the goal of this sensor is to detect the binding of small molecules to its surface, a high bulk sensitivity might create a lot of noise to the detection e.g. temperature fluctuations. It is therefore important to study how surface sensitive this sensor is [129]. In order to investigate surface or local sensitivity, we performed a resonance position tracking for different thicknesses of a molecular layer of refractive index equal to 1.4 around the gold PSWC. In Fig. 2.31(c), the shift of the resonant wavelength is shown for a molecular layer thickness growing from 0 to 30 nm for a gold PSWC with the same geometrical parameters as the one shown on Fig. 2.28. When changing the spacer thickness from 40 nm to 80 nm an increase in the local sensitivity is observed. For thin layers the sensitivity is extremely high, since it is related to the field intensity located in the slot of the cavity. Both field intensities and local sensitivities decrease the further we are from the metal surface. We believe that the high local sensitivity combined to the unique excitation of this plasmonic sensor can rival single particle localized surface plasmon resonances (LSPRs) and be more easily multiplexed.

The performance of the sensor can be benchmarked by a figure of merit (FOM) expressed by the ratio of the sensitivity over the full width at half maximum (FWHM) of the resonance. In the case of LSPR the best FOM is around 3 and the sensitivity ranges around 200 nm/RIU [130]. With a FOM of 4.1 for a spacer thickness of 40 nm, our sensor outperforms LSPR sensors.

2.5 Experimental Results

2.5.1 Silicon waveguide propagation losses

The measurement of the propagation losses of integrated waveguides fabricated by a top down approach provides an important information which validates the used fabrication technology and the design rules. Different fabrication technologies are used for the fabrication of silicon waveguides and their respective propagation losses can be easily compared with results found in the literature [131]. Several loss mechanisms are found in silicon waveguides: absorption losses, radiation losses and scattering losses.

A mode propagating in a waveguide with an initial light intensity I_{in} will be attenuated by a loss factor α along its propagation direction z as:

$$I_{\text{out}}(z) = I_{\text{in}} \exp^{-\alpha z} \quad (2.16)$$

The loss factor alpha includes the absorption losses, the radiation losses and the scattering losses.

Losses are often expressed in dB which is the ratio of the transmitted intensity to the initial

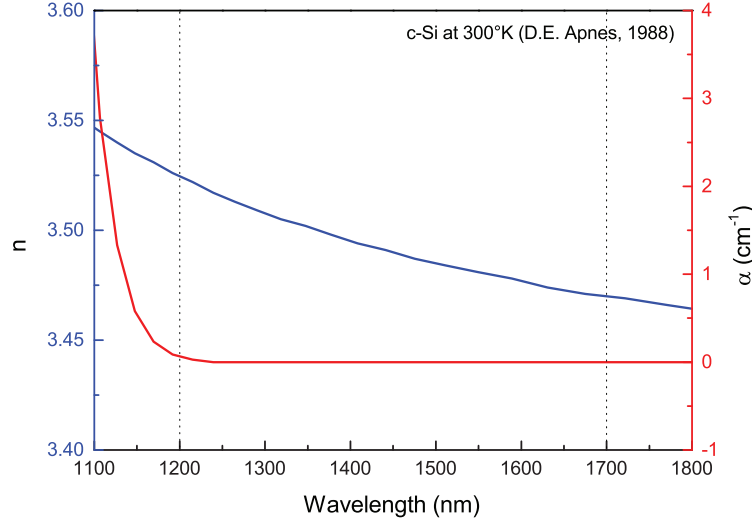


Figure 2.32 – Refractive index and absorption coefficient of crystalline silicon at 300°K reproduced from [5].

intensity. It is define as:

$$\text{losses[dB]} = 10 \log \left(\frac{I_{\text{out}}(z)}{I_{\text{in}}} \right) = 10 \frac{\ln(\exp(-\alpha z))}{\ln(10)} = -\frac{10}{\ln(10)} \alpha z \quad (2.17)$$

And the propagation losses in dB/cm are expressed by:

$$\alpha_{\text{dB}}[\text{dB/cm}] = -\frac{10}{\ln(10)} \alpha = -10 \log(e) \alpha \simeq -4.34 \alpha \quad (2.18)$$

2.5.1.1 Absorption losses in silicon

Single crystal silicon has a band-gap energy of 1.12eV which corresponds roughly to a wavelength of 1100nm. Band-edge absorption occurs when the light having a wavelength bellow 1100nm is absorbed because its energy is high enough to excite an electron from the valence band to the conduction band. For light having a wavelength above 1100nm silicon should be transparent. The transition of the absorption is not abrupt at 1100nm as it can be seen in Fig. 2.32 which shows the refractive index and the absorption coefficient for crystalline silicon [5].

As shown in Fig. 2.32, pure undoped silicon is transparent from 1200nm to the mid-infrared. In doped silicon, the injection (ΔN) or removal ($-\Delta N$) of free carriers by impurities changes the silicon absorption coefficient, which is directly related to the imaginary part of the refractive index as $k = \alpha \lambda / 4\pi$. Therefore by using Kramer-Kronig dispersion relation one can also relate its change of the real part of refractive index [132]. These changes are only significant for high doping levels above 10^{17} . For highly doped silicon, the absorption coefficient as well as the refractive index change is quadratic with the increase of wavelength. Equations 2.20 and 2.19

can give an approximation of the changes in absorption coefficient and refractive index [133].

$$\Delta n = - \left(\frac{e^2 \lambda^2}{8\pi^2 c^2 \epsilon_0 n} \right) \left[\frac{\Delta N_e}{m_{ce}^*} + \frac{\Delta N_h}{m_{ch}^*} \right] \quad (2.19)$$

$$\Delta \alpha = - \left(\frac{e^3 \lambda^2}{4\pi^2 c^3 \epsilon_0 n} \right) \left[\frac{\Delta N_e}{m_{ce}^{*2} \mu_e} + \frac{\Delta N_h}{m_{ch}^{*2} \mu_h} \right] \quad (2.20)$$

Changes of absorption coefficient and refractive index can also be induced by an external electric field applied to the material. This electrooptical effect is well known under the name of the Franz-Keldysh effect. This effect is used in state of the art electrooptical modulators to induce a phase change [134].

The silicon device layer of the silicon-on-insulator (SOI) wafers used to fabricate our waveguides is slightly p-doped with a boron concentration of around 10^{15} , therefore we are not expecting any absorption losses in the used bandwidth of 1200nm to 1700nm.

2.5.1.2 Surface scattering losses

Surface scattering losses are mainly due to the vertical side wall roughness of the waveguide. These can be induced during the lithography step, in the form of roughness of the patterned photo-resist or during the transfer of the photo-resist shape into the underlying film by the dry etching process. In the case of using e-beam lithography to define the waveguides, stitching errors between successive write-field alignment also lead to scattering losses. A simple model which is widely used to understand the behaviour of the scattering losses has been developed by P.K. Tien [135]. It is based on the Rayleigh smooth-surface criterion reported by Lord Rayleigh, 1903, in his work about sound wave reflection on rough surfaces [136]. The term $K^2 \cos^2 \theta_m$ of equation 2.21 is the total integrated scatter intensity per unit area for smooth surfaces ($\sigma \ll \lambda$) found by Davies [137] and based on Rayleigh's work. For further reading about modeling the scattering of rough surfaces one could read the following references: [138, 139, 140]. In his work, P.K. Tien used Davies's simple formula to express the waveguide propagation losses due to scattering. It shows that the propagation loss α for a slab waveguide having rough side walls is defined as:

$$\alpha_s = K^2 \left(\frac{1}{2} \frac{\cos^3 \theta_m}{\sin \theta_m} \right) \left(\frac{1}{w + \frac{2}{k_{\perp}}} \right) \quad (2.21)$$

Where,

$$k_{\perp} = \sqrt{\beta^2 - n_{out}^2 k_0^2} \quad (2.22)$$

and

$$K = \frac{4\pi n_{core}\sigma}{\lambda_0} \quad (2.23)$$

Where σ is the variance of the surface roughness; θ_m the incident angle of the bounded wave on the waveguide side wall boundary; n_{out} the index outside of the waveguide; n_{core} the index of the waveguide core; w the width of the waveguide core, λ_0 the free space wavelength; k_0 the free space wave vector; β the propagation constant of the waveguide mode which is the parallel component of the wave vector inside the core and ik_\perp the value of the perpendicular component of the wave vector in the evanescent field (k imaginary). The model shows that the losses increase quadratically with σ and that they increase with decreasing waveguide width. Therefore, it is important to fabricate the wanted waveguide as large as possible. For higher order modes which have a larger propagation constant and thus a larger angle θ_m the losses are also increasing drastically. The higher losses from the higher order modes also comes from the fact that the mode profile is confined closer to the side walls of the waveguide and therefore it is interacting stronger with them.

2.5.1.3 Radiation losses

Radiation losses in waveguides arise from the coupling of the evanescent tail of the guided mode to the outer medium beyond the cladding. In silicon waveguides, radiation losses can arise from a too thin silicon dioxide box layer thickness of the SOI wafer. In that case, for longer wavelength (i.e. >1700nm) the quasi-transverse electric (q-TE)₀ mode tends to loose its confinement in the core and the evanescent tail might extend several microns into the bottom silicon dioxide layer. If a significant overlap between the evanescent tail and the silicon substrate exist, then the mode might experience some radiation losses. Another case where radiation losses can be seen in guided modes is in the waveguide bends when the bending radius becomes too small. In that case, the condition of total internal reflection might not be satisfied anymore, and part of the guided mode can leak to radiative air modes. The same phenomenon appears in waveguide adiabatic tapers if they are too short. In our case, the design of the waveguides has been done to minimize the radiation losses to almost zero.

2.5.2 Measurement of the propagation losses

According to the three loss mechanism treated in the earlier sections, we expect the side wall scattering losses to be the dominant ones in our fabricated waveguides. The measure of the propagation losses of our silicon strip waveguides is the first characterization step needed before any measurement of the plasmonic slot cavity. Three different known techniques which are commonly used will be evaluated. The cut-back method, the Fabry-Pérot fringe contrast method and the Fabry-Pérot Fourier analysis method will be briefly explained in the next paragraphs.

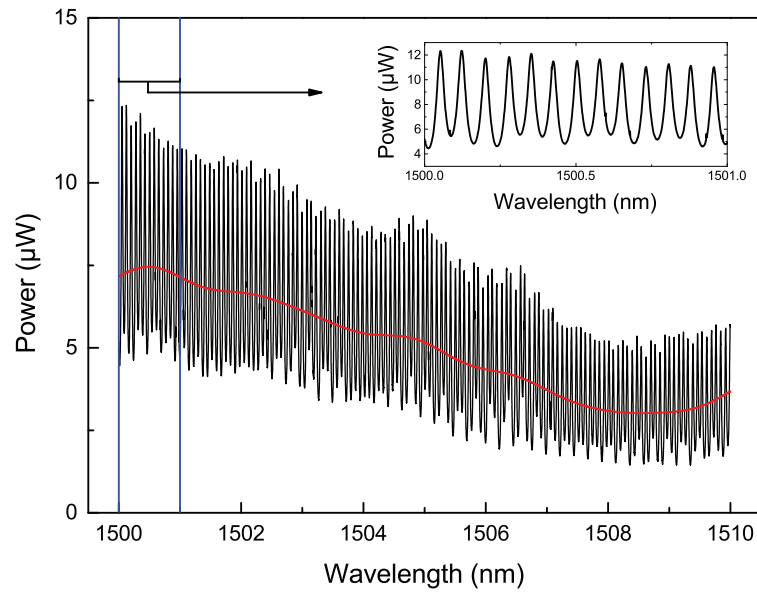


Figure 2.33 – Typical transmission spectrum acquired by sweeping a tunable laser from 1500-1510nm in 1pm steps. The spectrum shows high contrast Fabry-Pérot fringes. A bad alignment stability is shown here by the DC power (Fourier filtered signal) shown in red which drops over time due to injection misalignment.

For all these measurements, the waveguides of different chips coming from different fabrication batches will be excited with an external cavity tunable laser (HP 81682A). The excitation wavelength will be swept from 1500nm to 1510nm in 1pm steps and the transmitted intensity will be recorded by a photodiode power sensor (Thorlabs S150C). The wavelength sweep of 10000 samples takes around two hours to complete, therefore the alignment stability during this time is critical. The alignment of the input and output polarization maintaining (PM) lensed fibers is done by two 3-axis piezo stages very precisely. But even with the 3-axis piezo stage, we see that the temperature change in the room is affecting the coupling efficiency over hours. In Fig. 2.33 we show a typical spectrum acquired during a wavelength sweep of 10nm bandwidth. The spectrum shows high contrast Fabry-Pérot fringes, which as we will see later can be useful for the loss measurement of the waveguide. The spectrum has been Fourier filtered to remove all high frequency components (cut-off at 0.83) and reveal the DC power. This has been done to highlight the stability of the injection. In this case, the position of the lensed PM fibers are slowly shifting away from the maximum coupling position. As the alignment is not active in our setup, lots of care must be taken to avoid any heat induced perturbations which would create some linear expansion of the metallic parts of the stage. For example, one should avoid touching the metallic stage with the hands.

During all the measurements, the tunable laser power has been set to 2mW of output power. The laser was connected to a PM-1300 XP patch cord of 2m length and then connected to a PM lensed fiber for injection into the chip. The light at the output of the waveguide is collected by a lensed fiber (not PM) which is connected to a 2m long patch cord of PM-1300 XP and

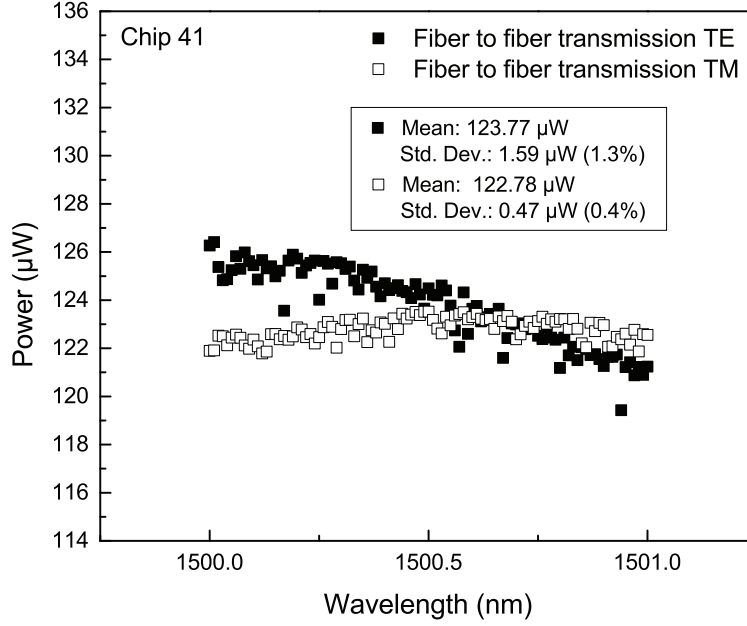


Figure 2.34 – Transmission measurement without a chip; from PM lensed fiber to lensed fiber.

then inserted in front of the photodiode power sensor. In Fig. 2.34 we see a transmission measurement of 1nm bandwidth at 1500nm between the input and output lensed fiber. One dataset is for the input PM lensed fiber rotated for transverse electric (TE) polarization and the other dataset for the fiber rotated by 90° for transverse magnetic (TM) polarization. From this measurement we can extract the input power for the next propagation loss measurements.

2.5.2.1 Cut-back method loss measurement

The cut-back method is the simplest loss measurement method. It consist of measuring the intensity transmitted through similar waveguides of different length. We can plot the transmitted power with a natural logarithmic scale as function of the waveguide length and make a linear fit of the obtained points. The slope of this line will give us the loss coefficient α as described in equation 2.24.

$$\alpha = \frac{\ln(I_1/I_2)}{z_1 - z_2} \quad \text{for } z_2 > z_1 \quad (2.24)$$

The cut-back method has one main disadvantage. It assumes that the coupling loss is consistent between each measurement. To measure the transmitted intensity through a waveguide, different injection techniques can be used and they will have different advantages and disadvantages as we have discussed in section 2.4.1.1 on page 34. The three main injection methods are: end-fire coupling, prism coupling and grating coupling.

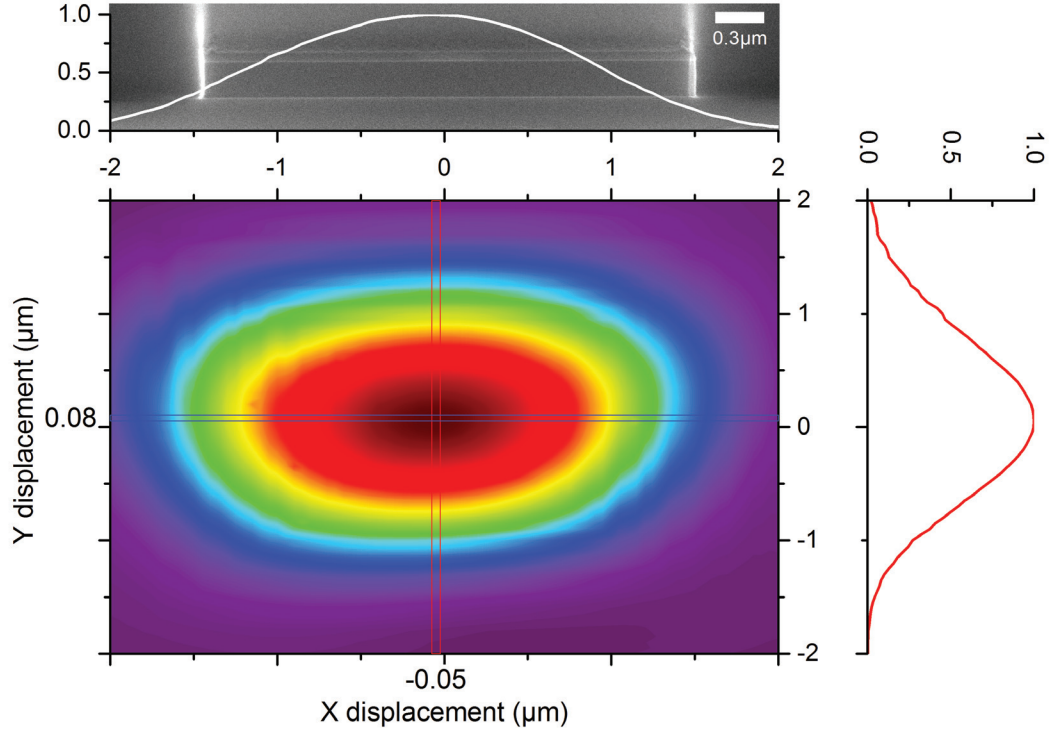


Figure 2.35 – Measurement of the normalized coupling efficiency as function of the PM lensed fiber misalignment (2 μm spot size) for a 3 μm by 0.22 μm silicon slab waveguide covered with a 50 nm thick SiO₂ layer.

The end-fire coupling has the advantage of not being restricted in the bandwidth that we want to inject. Therefore we chose this technique. With this technique it is not possible to distinguish the losses of different modes inside the waveguide. Moreover, for high refractive index materials like silicon, the facet reflection can be very high and Fabry-Pérot resonances can perturb cut-back measurements at a single wavelength. In the case of end-fire coupling, the injection alignment needs to be consistent between the measurement of each different waveguide. In Fig. 2.35 we measured the normalized coupling sensitivity as function of the position of the lensed fiber. This measurement has been done thanks to the use of a 3-axis closed loop piezo positioning stage. One can see that a misalignment of less than 1 μm already leads to a coupling loss of more than 3 dB. Thanks to the high resolution of the piezo stage, the alignment reproducibility in our setup is assumed to be excellent. The consistency of the quality of the end-facet is therefore the main source of error in a cut-back measurement done with end-fire coupling. Thus we systematically inspected the waveguide facets of all our samples with the scanning electron microscope before measuring them.

Two different ways of preparing a sample for an end-fire cut-back loss measurement exist. One can take a very long waveguide, measure its transmission and then cleave the chip to reduce its length and repeat this several times. In that case, we have the advantage of measuring always the same waveguide but the facet condition can be different at each cleave. One can

also fabricate a chip with several waveguides of different lengths and measure the transmitted power for each waveguide consecutively. In that case the advantage is that if the cleaving is good for one waveguide, the chance that it is also good for all the others is relatively high. But the drawback, is that for each measurement, a different waveguide is measured. In our case, the samples are too small to be cleaved consecutively to different sizes, therefore we fabricated different waveguides of different sizes on the same chip.

2.5.2.2 Fabry-Pérot resonator losses measurement

The waveguide can be considered as a Fabry-Pérot resonator [141] of length L . The losses can then be calculated by measuring the transmission through the waveguide for different phase changes. These phase changes can either be induced by sweeping the wavelength of a monochromatic source or by changing the cavity length L for example by heating. The transmission as function of the wavelength will have a typical form of Fabry-Pérot fringes in the spectrum. We will see that the propagation losses can be extracted from measurement of the maxima and minima of the transmission spectrum (I_{max} and I_{min}).

In the following paragraphs, we will detail how the losses can be extracted from the Fabry-Pérot theory. The transmitted intensity I_t of the Fabry-Pérot resonator (the waveguide) for both mirrors having the same reflectivity (R) is given by equation 2.25 where I_i is the incident intensity [142]. The equation 2.25 is also often written in the form given by equation 2.26.

$$I_t = \frac{T}{1 + R^2 - 2R \cos \phi} I_i \quad (2.25)$$

Using the trigonometric identity $\cos \phi = 1 - 2 \sin^2 \frac{\phi}{2}$ equation 2.25 can also be written like :

$$I_t = \left(\frac{T}{1 - R} \right)^2 \frac{1}{1 + F \sin^2 \left(\frac{\phi}{2} \right)} I_i = \left(\frac{T}{1 - R} \right)^2 \frac{1}{1 + \left(\frac{2\mathcal{F}}{\pi} \right)^2 \sin^2 \left(\frac{\phi}{2} \right)} I_i \quad (2.26)$$

Where $F = \frac{4R}{(1-R)^2}$ is the coefficient of finesse, and \mathcal{F} is the finesse ($\mathcal{F} = \frac{\pi\sqrt{R}}{1-R}$). If we assume that there are no losses during reflection or transmission at the waveguide facets, then $R + T = 1$. We can then simplify equation 2.26 in the form of equation 2.27.

$$I_t = \frac{1}{1 + F \sin^2 \left(\frac{\phi}{2} \right)} I_i \quad (2.27)$$

The transmitted intensity only depends on the phase change $\phi = \frac{4\pi L n_g}{\lambda_0}$. In the latter definition of the phase change, the group index is used instead of the commonly used effective index because of the waveguide dispersion.

We can take into account the propagation losses in the resonator (the waveguide) by assuming that for each reflection, the light has to travel a distance L (cavity length). The propagation losses occurring during a distance L is expressed as $\exp(-\alpha L)$, where α is the loss coefficient. This loss term can be included in equation 2.27 by applying the following substitution : $R \rightarrow R \exp(-\alpha L)$ [128].

$$I_t = \frac{1}{1 + \frac{4R \exp(-\alpha L)}{(1 - R \exp(-\alpha L))^2} \sin^2\left(\frac{\phi}{2}\right)} I_i \quad (2.28)$$

By measuring the minima and maxima of the transmitted intensity of the fringes, we can find the propagation losses. The maximum transmitted intensity $(I_t)_{max}$ occurs when $\sin^2\left(\frac{\phi}{2}\right) = 0$ and the minimum transmitted intensity occurs when $\sin^2\left(\frac{\phi}{2}\right) = 1$. The fringe contrast is therefore given by equation 2.29 and is not anymore dependent on the input power I_i .

$$\frac{I_{max}}{I_{min}} = \frac{(I_t)_{max}}{(I_t)_{min}} = \frac{1 + 2R \exp(-\alpha L) + R^2 \exp(-2\alpha L)}{1 - 2R \exp(-\alpha L) + R^2 \exp(-2\alpha L)} \quad (2.29)$$

The equation can be rewritten to express the propagation losses :

$$\alpha L [\text{dB}] = -10 \log(e) \ln \left(\frac{1}{R} \frac{\sqrt{\frac{I_{max}}{I_{min}}} - 1}{\sqrt{\frac{I_{max}}{I_{min}}} + 1} \right) \quad (2.30)$$

The facet reflection R is needed in order to obtain the result. The latter one can be approximated by the Fresnel reflection at normal incidence given in equation 2.31 by using the refractive index of the waveguide core n_{core} and the refractive index of the outer medium n_{out} . This approximation might not be really accurate for the case of a strongly confined mode like for our silicon waveguides. The reflectance for $n_{core} = 3.48$, which is silicon's refractive index at 1500nm, is equal to $R_{Fresnel} = 0.306$ by using the Fresnel reflection. It is recommended to simulate the reflection directly in 3D with the time domain solver of CST Microwave Studio (CST MWS). This gave us a reflection of $R_{CST} = 0.378$ at 1500nm for a slab waveguide of $3\mu\text{m}$

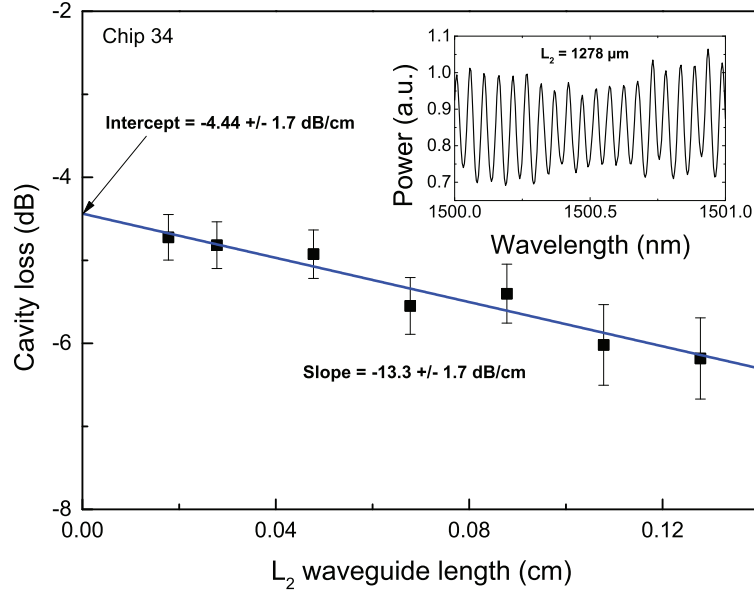


Figure 2.36 – Propagation losses of silicon waveguides of 450nm width and 220nm height with and additional 50nm of SiO₂ deposited by plasma enhanced chemical vapor deposition (PECVD) at $\lambda_0 = 1500\text{nm}$ measured by fringe contrast method. (Chip 34).

width and excited with the q-TE₀ mode.

$$R = \left(\frac{n_{out} - n_{core}}{n_{out} + n_{core}} \right)^2 \quad (2.31)$$

The fabricated waveguides of different length were measured in transmission for wavelengths ranging from 1500 to 1501nm in steps of 0.04nm. Seven waveguides of different length were fabricated on the same chip for the loss measurement, as shown in Fig. 2.4 on page 19. One waveguide is composed of different sections having different propagation constants. The first section is a slab waveguide which has a silicon cross-section of $3 \times 0.22\mu\text{m}$ with a 50nm thick top layer of SiO₂. The second section is the silicon wire waveguide which have a silicon core cross-section of $450 \times 220\text{nm}$ and an additional 50nm thick top layer of SiO₂. They are interconnected by a $50\mu\text{m}$ long adiabatic taper and a 90° bend of $25\mu\text{m}$ radius on each side. The length of the slab waveguide (L_1) is defined by the cleaving of the sample and is constant for all the waveguides on the same chip. The length of the silicon wire waveguide (L_2), which is including the two waveguide bends, is varied across the different waveguides on the chip. The fringe contrast difference is therefore induced by the increasing propagation loss of the silicon wire waveguides of increasing length. In the inset of Fig. 2.36 we show a typical spectrum measured from a waveguide having an L_2 length equal to $1278\mu\text{m}$ ($78\mu\text{m}$ is the length of the two bends). By linearly fitting the cavity losses as function of the L_2 waveguide length, one can extract the slope of the line which is giving us a propagation losses of 13.3dB/cm, see

Fig. 2.36. The intersection of the line with the y-axis is giving the constant losses across the different waveguides. These losses are including the propagation losses of the slab waveguide, the taper losses as well as the the bend losses. In Fig. 2.36, these losses are equal to 4.54dB. Unfortunately, there is no exact way to figure out the repartition of these constant losses, but one can make some approximations. It is rather safe to make the hypothesis that the slab waveguide loss are negligible in these 4.54dB and that the main contribution to these losses is coming from the tapers and the bends. We should therefore investigate a design change for the tapers and the bends in the future to reduce these to the maximum. This can be done easily by fabricating some new samples having for example an increasing number of bends per waveguide or an increasing number of tapers par waveguide. Then the measurement and the result interpretation would be similar to the work done here for the silicon wire waveguides losses.

2.5.2.3 Fourier analysis of the Fabry-Pérot resonator

As explained in the previous paragraph, it is difficult to extract the losses of individual lumped elements inside a resonator by only measuring the fringe contrast of the transmitted intensity. Multiple Fabry-Pérot cavities are formed inside the resonator induced by some lumped elements that are perturbing the light propagation. This results in the superposition of multiple beat frequencies in the transmitted spectrum. In the inset of Fig. 2.36 if we look at the envelop of the spectrum, we can already notice a beating of lower frequency which is affecting the fringe contrast. The Fourier analysis of the spectrum can reveal all the perturbations inside the cavity and helps to locate them. In the next paragraphs, we will explain briefly how to make such an analysis.

The equation 2.28, which is commonly called the Airy function, can be Fourier transformed has shown by Hofstetter and Thornton [143]. But the result is complicated and not easy to relate to the losses of the cavity. Instead, one can show that the equation 2.28 can be expressed as an infinite superposition of Lorentzian functions with a constant separation. It can be expressed as a convolution of an infinite series of δ function with a Lorentzian function. Its Fourier transform results in the product of the infinite δ series with the transform of the Lorentzian function, which is a symmetric exponential decay function. This has been mathematically derived by Hofstetter and Thornton [144].

For an easier lecture of the Fourier transformed spectrum, the transmission spectrum is expressed in wavenumber ($k = \frac{2\pi}{\lambda_0}$) instead of wavelength. In that case the conjugate variables are wavenumber (k) and optical path length (d). In the transmission spectrum expressed in wavenumber, the free spectral range is expressed as $\Delta k = \frac{\pi}{n_g L}$. The peak position in the Fourier transformed spectrum is therefore expressed as $d = \frac{n_g L}{\pi}$.

$$HAR = R \cdot e^{-\alpha L} \quad (2.32)$$

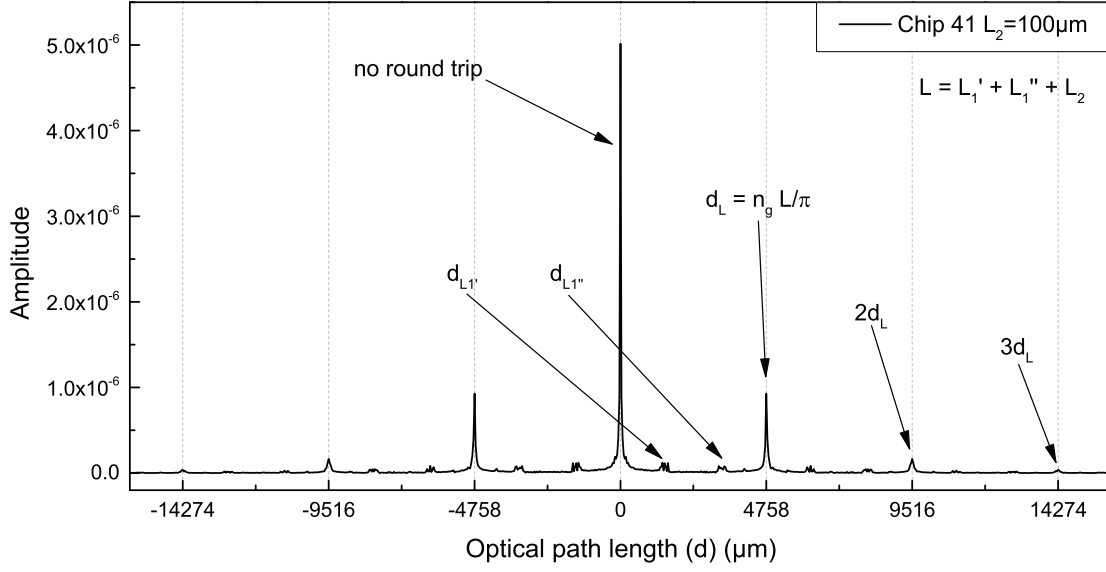


Figure 2.37 – Fourier transform of the transmission spectrum of a waveguide with $L_2 = 100\mu\text{m}$. The spectrum is showing the different cavities formed in the waveguide because of the tapers and the bends.

$$\alpha L[\text{dB}] = -10 \log(e) \ln \left(\frac{\text{HAR}}{R} \right) \quad (2.33)$$

The main result here is that the harmonic amplitude ratio (HAR) is a simple function expressed by equation 2.32. The amplitude of the peak at optical path difference (OPD) = 0 represent the light intensity which passed through the cavity without any reflection and the peak at d_L represents the light intensity due to one round trip inside the cavity. The following peaks represent light which has made additional round trips inside the cavity. This is shown clearly in Fig. 2.37. Moreover, the Fourier transform of the transmission spectrum will bring out the other cavities created because of localized perturbations that are present in the waveguide. In the case of the measurement of the waveguide $L_2=100\mu\text{m}$ of chip 41 shown in Fig. 2.37, the cavities formed inside the slab waveguide between the facet and the taper (L_1' and L_1'') are appearing between 0 optical path difference and the main peak L .

The propagation losses of a waveguide can be found by measuring the HAR of the main peak L in the Fourier transformed transmission spectrum. Once the HAR is measured, one can plot the HAR similarly as for the fringe contrast method by plotting $\alpha L[\text{dB}]$ given by equation 2.33 as function of the different length L_2 of the photonic wire waveguide. The loss coefficient is then given by the slope of the fitted line. If the losses are not too important, it is more precise to measure the HAR between the peak d_L and $2d_L$ because the fundamental peak also includes the power of the other cavities. On the contrary, if the losses are high like shown in Fig. 2.38, it is better to measure the HAR on peak 0 and 1.

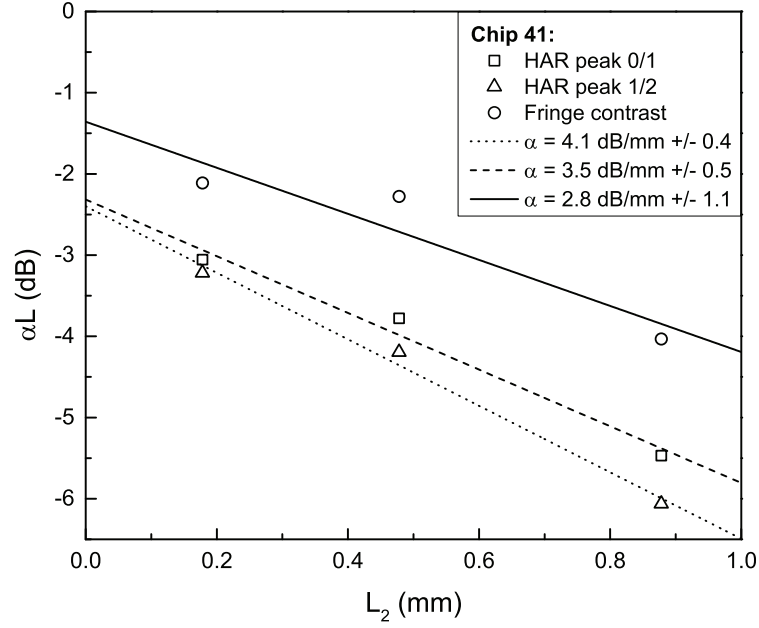


Figure 2.38 – Propagation losses calculated with three different methods: the fringe contrast method, the HAR of peak 0 and 1 and the HAR of peak 1 and 2.

We show a little comparison of the different loss measurement methods in Fig. 2.38. We can see that we have some discrepancy in the results obtained from the different methods. This is because each method has there pros and cons.

The fringe contrast method is very efficient if the measured waveguides are straight and uniform so that only one Fabry-Pérot cavity formed by the two end facets is present in the waveguide. In that case, the transmission spectrum should look like an infinite superposition of Lorentzian functions with a constant separation without any additional low frequency modulation. This helps in reducing the error of the measurement of I_{max} and I_{min} .

The Fourier analysis method is very useful when the waveguide is made out of different sections which have some reflections at their interfaces. This is the case for example in our waveguide where we have an interface between the slab waveguide and the photonic wire waveguide which exhibit some non negligible reflections.

Here we want to point out that the losses of the chip 41 shown in Fig. 2.38 are much higher that the losses measured for the chip 34 shown in Fig. 2.36. This is due to different etching recipes used during fabrication. The chip 41 has been etched with a low selectivity etch recipe and its top SiO_2 layer has been etched several nanometers. The resulting surface roughness of the top SiO_2 surface is therefore altered which increases the propagation losses on that sample.

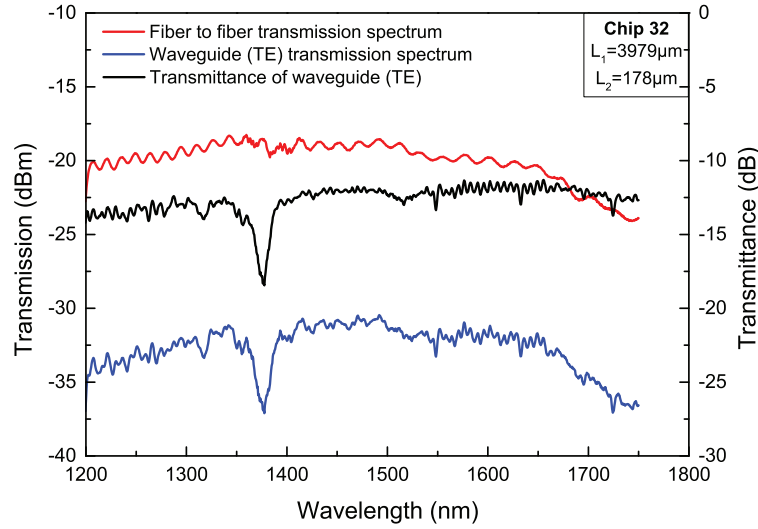


Figure 2.39 – Normalized transmission measurements in dB of a waveguide (TE mode) with a 178 μm long strip waveguide section. The fiber-to-fiber measurement as well as the raw waveguide transmission spectrum is shown for clarity.

2.5.3 Broadband transmission measurements of the integrated PSWC

After the measurement of the losses of the waveguide, we measured the broadband transmission of the waveguides from 1200nm to 1700nm with a super continuum laser source (NKT SuperK Extrem EXW-12). Before each measurement set with the super continuum laser a polarization alignment and a calibration procedure needs to be done. First the output of the lensed fiber needs to be imaged with a near infrared (NIR) camera and with the help of a broadband wire grid polarizer the lensed fiber is rotated to align the polarization to the wanted angle.

To obtain the transmittance of the samples a calibration of the transmission through the "empty" optical system is done by measuring the transmission spectrum when both lensed fibers put against each other. The transmittance spectrum of a waveguide is then obtained by dividing the transmission spectrum of the optical system including the waveguide by the transmission spectrum of the "empty" optical system. In Fig. 2.39 we show a typical result of such a procedure.

As shown in Fig. 2.39, the transmission spectra of bare waveguides showed an increasing propagation loss at shorter wavelengths below 1400nm. For these shorter wavelengths, the side wall roughness of the waveguides creates more scattering as discussed in section 2.5.1.2 on page 57. Moreover, an absorption dip can be systematically seen at around 1385nm on the transmission spectra of the waveguides having an SiO_2 top layer. This absorption peak is well known and comes from the excitation of -OH chemical bonds. It is well known that the humidity of the environment is creating a thin film of water molecules on all solid surface in contact with it. As we did all the measurements in air, we first thought that this absorption peak

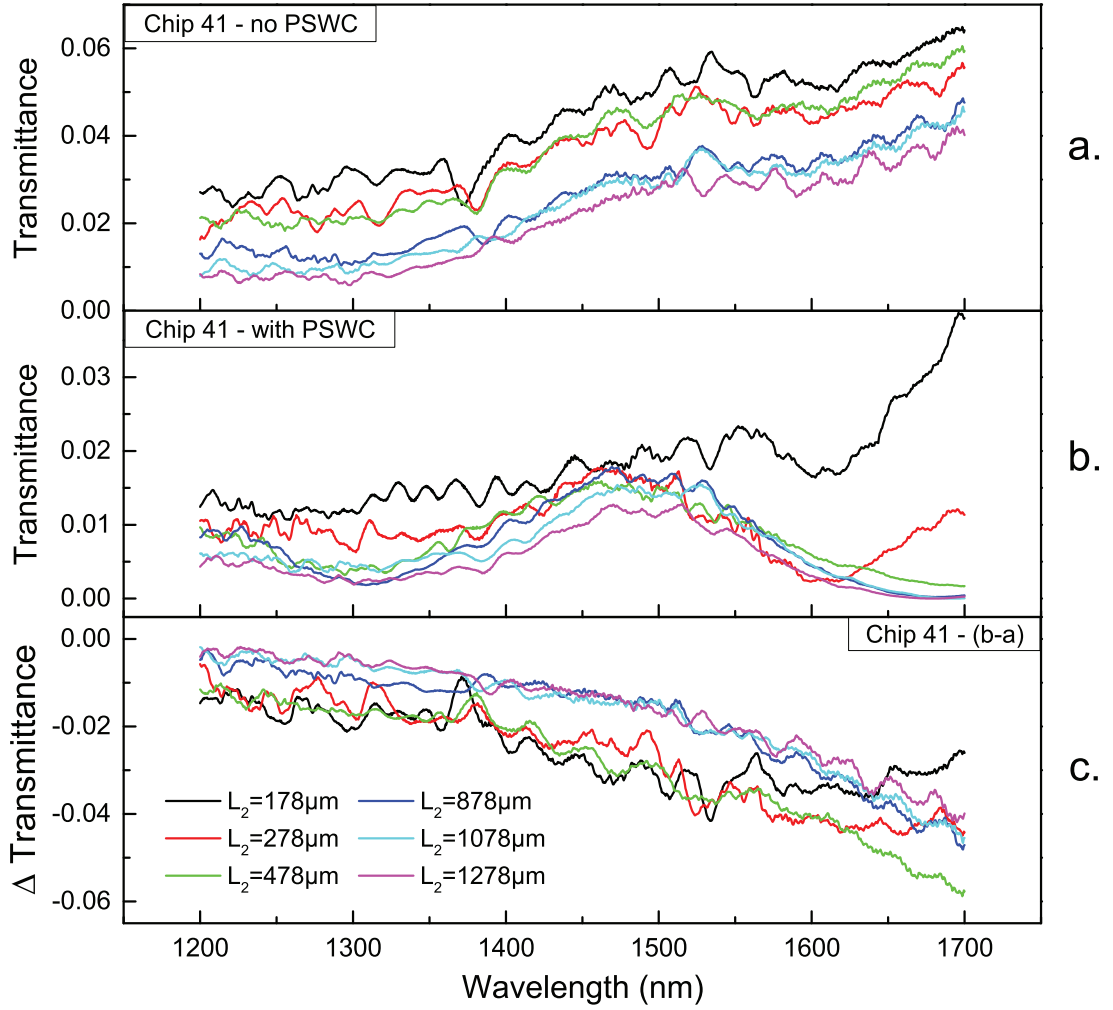


Figure 2.40 – Transmittance of chip 41 waveguides (a.) without and (b.) with plasmonic slot waveguide cavity (PSWC). (c.) Δ transmittance between waveguide with and without PSWC.

was due to this water film. But when we measured the transmission spectrum of waveguide without the top SiO_2 layer, the absorption peak disappeared. Therefore, we concluded that the PECVD deposited SiO_2 layer was containing some hydrogen. This hydrogen comes from the silane (SiH_4) gas used as precursor during the SiO_2 deposition. To get rid of this absorption peak, we should use another deposition technique like evaporation.

To locate the resonance position of the PSWC excited by the waveguide, we decided to measure the delta of transmittance between a waveguide without a PSWC and an identical waveguide with a PSWC. By using a reference waveguide without a PSWC we should get rid of all the waveguide specific losses and resonances assuming that both waveguides are identical. In Fig. 2.40 a first attempt to measure the PSWC response is shown. This measurement has been done on chip 41 which came out of fabrication with an out-of-specification SiO_2 layer thickness. Instead of having an SiO_2 layer thickness of 50nm, we measured a thickness of

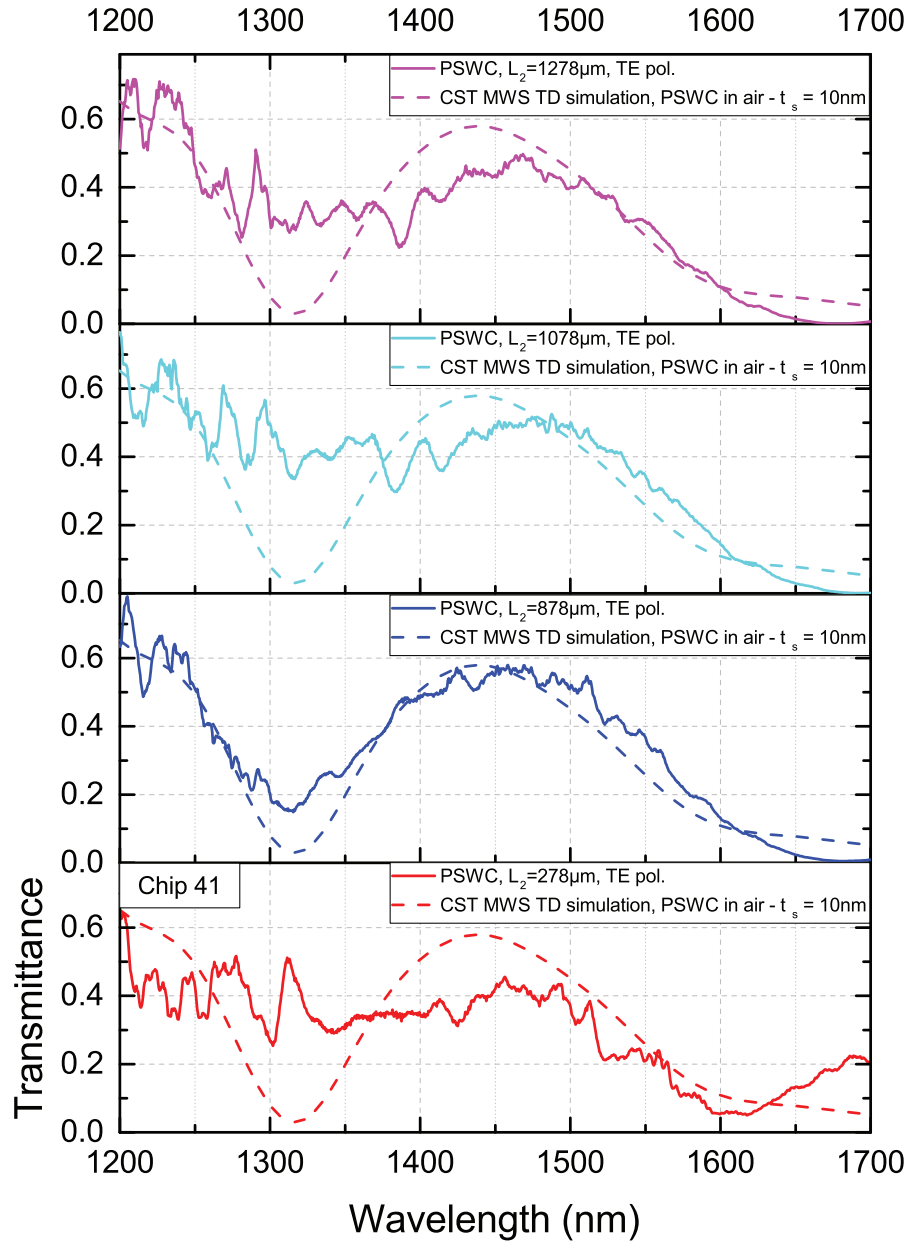


Figure 2.41 – Normalized transmittance spectra of waveguides having different lengths but all exciting the same PSWC with a spacer thickness (t_s) off 10nm . The transmission spectra have been normalized by the spectra of identical waveguides having no PSWC.

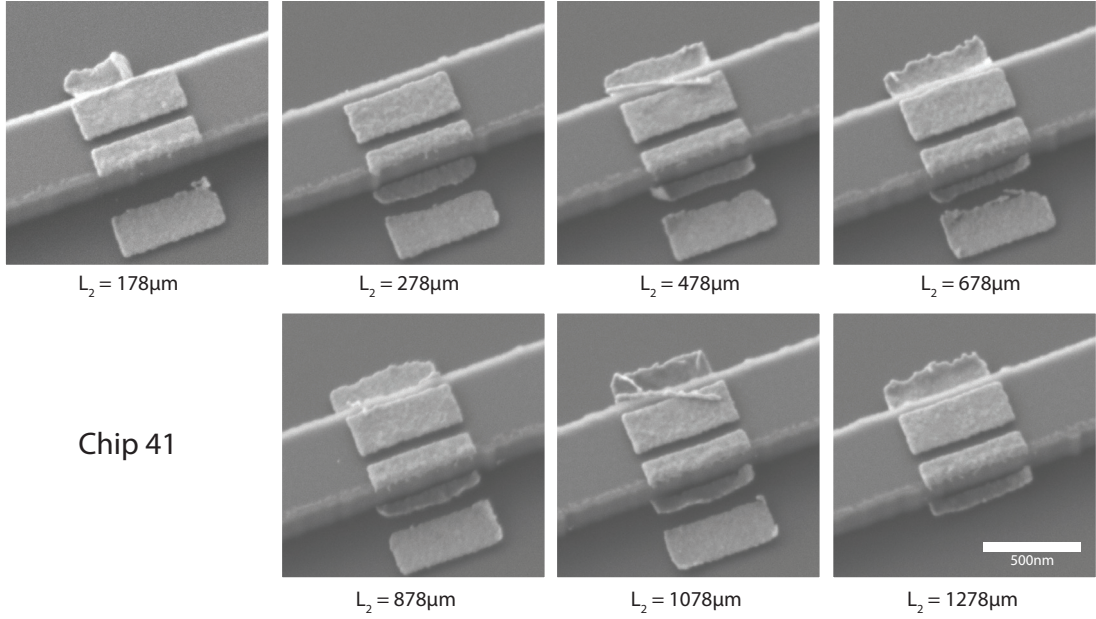


Figure 2.42 – Scanning electron microscope (SEM) images showing the PSWC on top of each different waveguide of chip 41.

18nm. The reason is that during the etching of the waveguide, the photoresist mask has been over etched and a part of the SiO_2 layer has been etched away. Unfortunately, we could not see any pronounced resonance dip in the measured delta transmittance results. The reason for this is that the PSWC cavity is scattering a lot of light out of the waveguide because the SiO_2 layer is not thick enough. It can be seen that the delta transmittance spectra are increasing in the negative direction, which means that more light is lost for longer wavelengths, because of the presence of the PSWC. This result agrees with the fact that the interaction of the q-TE mode with the PSWC becomes larger for longer wavelengths at which the mode is less confined in the waveguide. Because of the strong scattering, the information about the resonance is lost in the scattering as it can be seen in Fig. 2.40.

To overcome the problem of the masking of the resonance by scattering, we tried another approach of normalization. We assumed that the spectrum of the light inside the waveguide arriving just in front of the PSWC would be similar to the one exiting the waveguide on which there would be no PSWC. Therefore, we divided the spectrum acquired from the waveguide with a PSWC by the spectrum of the identical waveguide without PSWC. This normalization is not really correct because it does include the losses of the second part of the waveguide located after the PSWC. Nevertheless, like shown in Fig. 2.41, a resonance dip can be seen in the normalized spectra for some of the cavities around 1300nm. The dashed curve in Fig. 2.41 which is superposed onto the different measured data is the transmittance of the PSWC obtained by simulation with CST MWS. The measured transmittance for the waveguide with $L_2 = 878\mu\text{m}$, perfectly fits with the simulation.

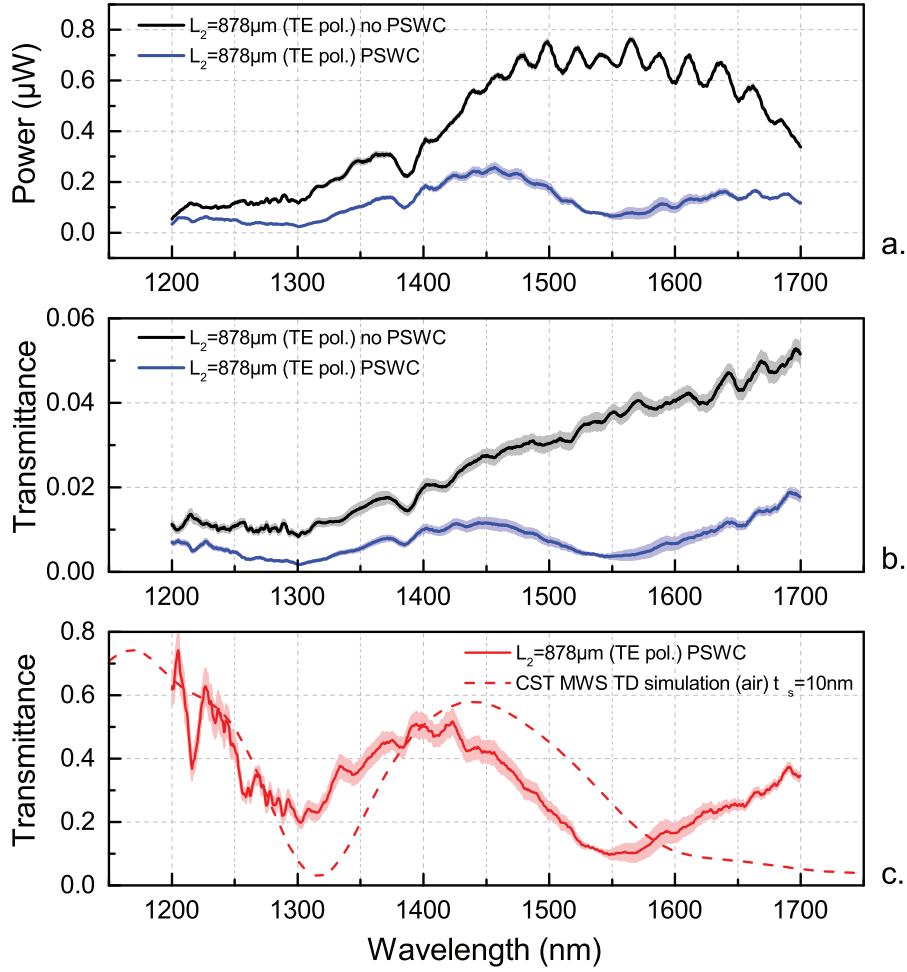


Figure 2.43 – (a.) shows the raw spectrum measured with the optical spectrum analyzer at the output of the waveguide, once with and once without a PSWC. The standard deviation is shown based on 5 repetitive measurements for which a new alignment of the fibers is done each time. (b.) shows the transmittance of the waveguide with and without the PSWC normalized by the fiber-to-fiber transmission. (c.) shows the transmittance of the PSWC obtained by dividing the transmittance of the curve in (b.) with a PSWC by the one without a PSWC. The curve is exhibiting the plasmonic resonance located at around $\lambda = 1300\text{nm}$. The dashed curve in (c.) is the transmittance obtained by simulation with CST MWS in which the spacer thickness (t_s) was set to 10nm.

We can see that both curves are fitting very well. For the other waveguides of different lengths, the fit of the simulation data is less accurate. This can arise from the fact that each fabricated PSWC is not aligned on the waveguide with the same precision and that the PSWC fabrication quality varies a lot from waveguide to waveguide. Figure 2.42 shows the SEM images of the PSWC fabricated on top of each different waveguide of the chip 41. It can be seen that the resolution of lateral alignment of the PSWC is within $\sim 100\text{nm}$ for this chip. The alignment procedure during the e-beam exposure can still be optimized to reduce it to around 40nm . In that case, it would become interesting to deposit a single PSWC instead of three next to each other. In the SEM images we also noticed that the gold deposited on the sides of the waveguide tend to detach sometimes. This comes from the fact that the electron beam is focused on the top of the waveguide and that the exposure dose on the sides of the waveguide is not enough to clear the resist. The gold is then deposited on a thin resist layer which can sometimes be dissolved during the lift-off procedure.

After having analysed the results of the transmittance spectrum of the different PSWC shown in Fig. 2.41, we did some new measurements on the PSWC having the more pronounced resonance dip. The best result was chosen to be the PSWC sitting on the waveguide having a length $L_2 = 878\mu\text{m}$. The latter PSWC has also the best fit to the simulation result. In the following measurement, for every transmission spectrum that was measured, we did five consecutive measurements between which we realigned the lensed fibers. All measurements were done in a row as fast as possible in the same day to avoid for some environmental changes like humidity or temperature. These measurements are shown in Fig. 2.43. In the upper graph of Fig. 2.43 we show the raw transmission spectrum as measured by the spectrum analyser for the waveguide with and without the PSWC. In the graph, the curve of the transmission spectrum is the averaged curve extrapolated from the five consecutive measurements. The continuous light colored area above and below the curve of the averaged spectrum corresponds to \pm its standard deviation. In the graph of the middle of Fig. 2.43, we show the transmittance of the waveguide with and without the PSWC. This one is obtained by the division of the two spectra of the upper graph by the optical response of the system, i.e. the transmission from fiber to fiber. Similarly to the spectra shown in Fig. 2.40, both transmittances are showing the strong effect of the sidewall scattering which is inversely proportional to the wavelength. In the graph of the middle, the transmittance of the waveguide having a PSWC is already showing some absorption dips. In the bottom graph of Fig. 2.43, we show the PSWC transmittance which is obtained by dividing the transmission spectrum of the waveguide having a PSWC by the transmission spectrum of the same waveguide having no PSWC. The red dashed curve shows a result obtained by the time domain solver of CST MWS. The PSWC transmittance now clearly shows two resonance dips, separated by a free spectral range of 250nm . Compared to the previously obtained result showed in Fig. 2.41, we observe a slight blue shift of the resonance dip. As both measurement are done on the same cavity, it is possible that the plasmonic cavity made out of gold might have suffered from previous measurements. It would be interesting to calculate the light induced heat at the cavity position, which might effect the shape of the gold PSWC.

2.5.4 Far field scattering measurements of the excited PSWC

To confirm the results obtained by the measurements in transmission through the waveguides, we measured the far field scattering of the PSWC. This is done by collecting the light scattered by the cavity by a microscope objective and imaging it onto a single mode fiber. We used a Mitutoyo M Plan Apo NIR 20x objective which is chromatically corrected for the near infrared and having a numerical aperture of 0.4. This microscope objective is infinity corrected, therefore we used a tube lens to create the image onto the fiber core. The used tube lens was a Mitutoyo MT-L which has a magnification of 1x and which is also corrected for the near infrared. It is important that all the used optics is corrected for the infrared because we want to image the PSWC onto the core of a SMF-28e single mode fiber for all wavelength ranging from 1200 to 1700nm. The fiber has a core diameter of $8.2\mu\text{m}$ and a numerical aperture of 0.14. As the magnification of the optical system is 20x the size of the PSWC imaged onto the core of the single mode fiber should be roughly $12\mu\text{m}$. This will avoid collecting the scattering coming from other parts of the waveguide next to the PSWC. The total power collected by the single mode fiber is around hundreds of nanowatts. The spectrum is then measured with an optical spectrum analyser.

In Fig. 2.44 we show the results obtained from the scattering of the PSWC integrated onto the waveguide of length $L_2 = 878\mu\text{m}$ of chip 41. The scattering curve has been normalized by the transmission spectrum obtained by putting each lensed fiber in front of each other. In Fig. 2.44 we can observe that a peak of scattering is superposed onto the transmittance dip of the waveguide. Therefore we can conclude that the transmittance dip shown in the previous results is coming from the excitation of the plasmonic cavity.

2.5.5 PSWC sensitivity measurement

Since we validated the presence of the resonance dip in the transmission spectrum, we did a measurement of the resonance position shift as function of the refractive index change of the surrounding medium. On chip 41, we measured the transmittance of the PSWC sitting on top of the waveguide having a length of $L_2 = 878\mu\text{m}$ with deionised water as surrounding medium. To realized this experiment, we poured a $20\mu\text{L}$ drop of water onto the chip. This water droplet was just large enough to cover the whole chip from facet to facet. Unfortunately like shown in Fig. 2.45 no transmission dip could be seen anymore when water was surrounding the waveguide and the PSWC. When the spacer thickness is too small, the cavity is exposed to a stronger electric field resulting from the mode of the waveguide. Accordingly, the reason might be that because the spacer thickness of the chip 41 was only 10nm, the scattering of the PSWC became too large in water. The mode size of the silicon wire waveguide increases when the delta of refractive index between the core and the cladding decreases. Thus, the interaction between the PSWC and the q-TE waveguide mode is too strong, and the majority of the light is just scattered out of the waveguide without exciting the cavity.

Our aim was to make additional measurements with liquids of different refractive indices to

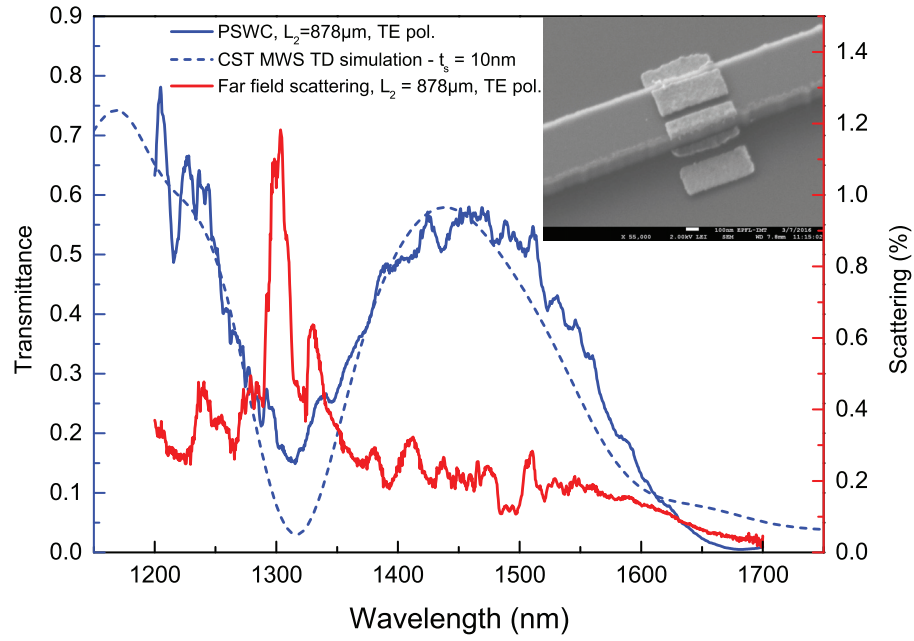


Figure 2.44 – Far field scattering of the PSWC compared with the measured transmittance of the PSWC through the waveguide and the CST MWS TD simulation.

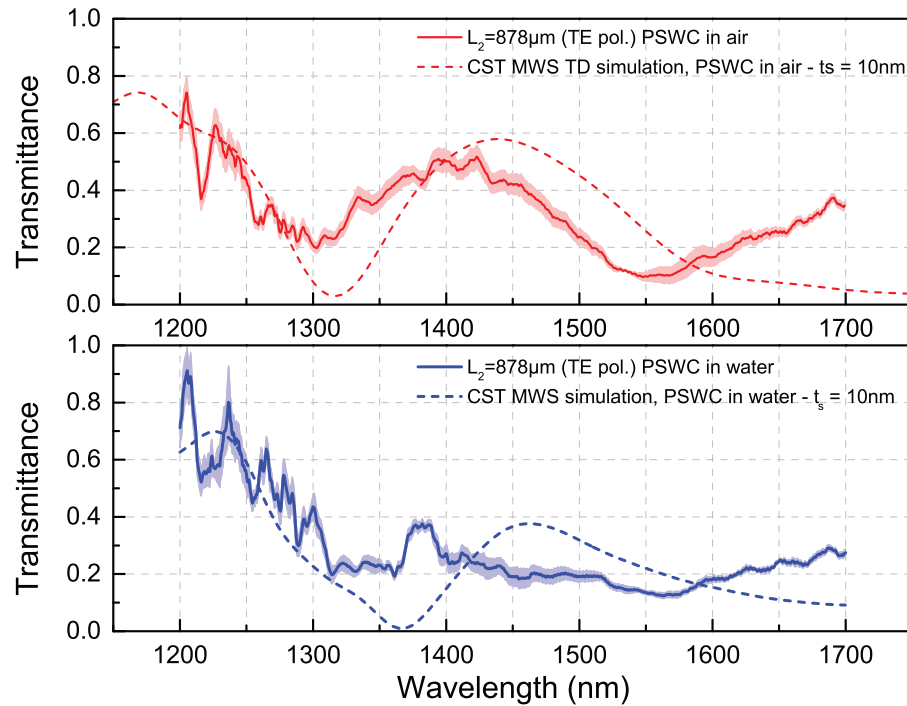


Figure 2.45 – Measured transmittance of the PSWC of Chip 41 and waveguide of length $L_2 = 878\mu\text{m}$ in air and in water. Simulation results obtained with the time domain solver of CST MWS are superposed on the measurements.

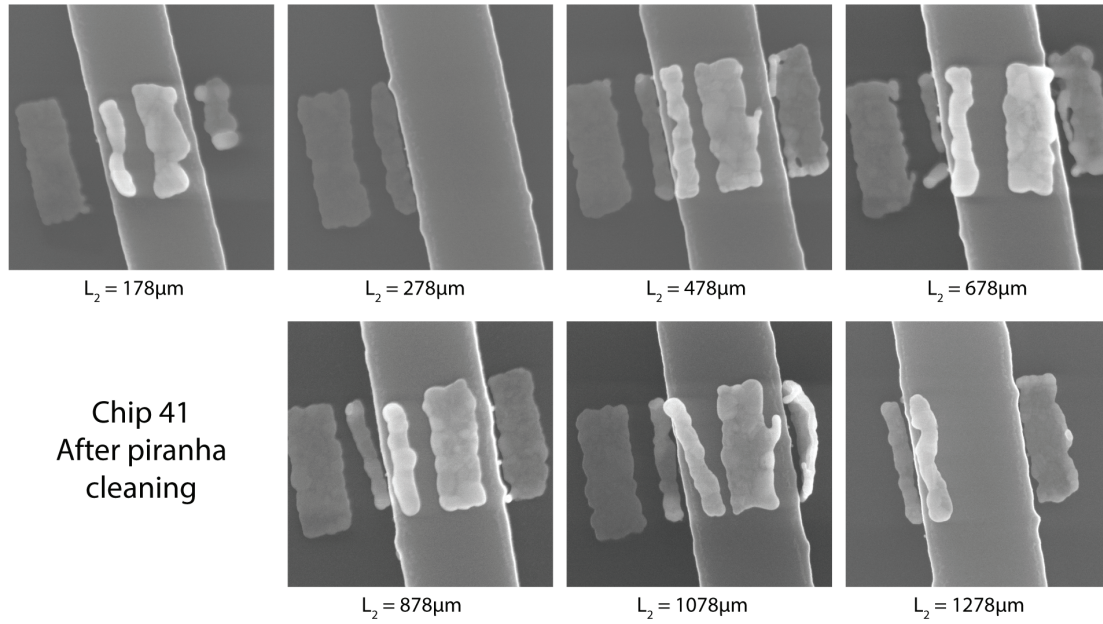


Figure 2.46 – SEM image of the deformed PSWC after a piranha cleaning. Rapid grain growth of the gold layer occurred due to elevated temperature in the piranha bath.

measure the sensitivity of the sensor to refractive index change expressed by $S = \frac{\Delta\lambda}{\Delta n}$. Unfortunately, after the first measurements with the water the chip 41 was dirty. The water droplet evaporates quickly from the surface of the sample and leaves a layer of contamination onto the sample which alters the transmittance of the waveguide. We tried to remove that contamination layer in acetone and isopropanol without success. Thus, we did a piranha cleaning of the sample. After the piranha cleaning, we observed the PSWC with the SEM again to see if the cavities were intact. Unfortunately, the cavities were destroyed by the heat generated by the exothermic chemical reaction taking place in the piranha bath. As can be seen in Fig. 2.46, the gold PSWC suffered from a rapid grain growth due to the elevated temperature of the piranha bath. The PSWC were completely deformed and not anymore usable for measurements. Due to a lack of time, we could not fabricate new samples for further characterization of the sensitivity and resolution of the PSWC based sensor.

Moreover, we showed in the simulation results of section 2.4.5 that the highest sensitivity could be obtained with larger spacer thicknesses. More measurement should therefore be done with spacer thicknesses of 50 to 80nm in the future.

2.6 Future perspectives and developments

Through the experimentation and because of our lack in knowledge at the beginning of the project, a lot of time has been spent on the fabrication and optimization of the silicon waveguides. We could finally achieve the fabrication of silicon waveguides based on silicon-on-insulator (SOI) substrates which had acceptable propagation losses. This knowhow gives us a new platform which is now ready to excite any kind of plasmonic cavity.

The fabrication of the plasmonic slot waveguide cavity (PSWC) could be realized with a really good quality but their alignment on top of the waveguides has not been optimized enough. Therefore, we needed to design a triple slot cavity which would eventually be aligned in a way to have one of the three slots in the middle of the waveguide. With the help of additional alignment marks closer to the waveguide it would be possible to align a single PSWC on top of the waveguide with an accuracy of 40nm.

The experimental setup could be complete with an InGaAs camera. This camera could be useful to image the losses and the defects of the waveguide. Additionally, this camera would help us to align the microscope onto the PSWC to collect its far field scattering. The camera would also help a lot in a better alignment of the optical setup and in the verification of the focal shift induced by possible chromatic aberrations.

To pursue the measurements of the PSWC, different coupling conditions have to be studied. The results obtained from simulation are showing a strong dependence of the resonance as function of the SiO₂ spacer thickness. In the future we should fabricate and measure more samples with different spacer thicknesses. It needs to be pointed out that the chip 41 which we used in our last measurement, had a spacer thickness of only 10nm. In this configuration the PSWC is too strongly coupled to the waveguide and too much light is scattered out of the waveguide. Better results are expected with spacer thicknesses of 80nm. Especially for the measurements of refractive index changes which were not successful in our case.

The sensor could also be very interesting for single molecule fluorescent detection thanks to the very small excitation volume of the plasmonic cavity. Moreover, the fact that the excitation is done in plane, and that the far field radiation of the cavity in the direction normal to the plane is low would help to increase the signal to noise ratio of the fluorescent signal emitted by an excited molecule.

We have seen in our attempt to measure the shift of the resonance position that a microfluidic cell is needed to have reproducible results. The fact that drops of liquid poured onto the chip are evaporating is perturbing the transmission spectrum too much. For future samples exhibiting a nicer resonance, a calibration curve of the sensor should be measured and saved. This can be done by using different reference liquids with calibrated refractive indices. Additionally a sensogram of the adsorption of a specific molecule could be done. This would request the specific functionalization of the gold surface with a thiol chemistry.

2.7 Conclusion

We started this project with the idea to develop a bio-sensor based on a nano-sized plasmonic cavity which would be excited by an integrated waveguide. This in-plane excitation of the plasmonic cavity was meant to address the problem of exciting and measuring a single nano-cavity in a densely packed area. We believe that the ability to highly multiplex the measurement on an integrated platform could also lead to smaller biosensors. Moreover, we paved the way to label free single molecule detection at high concentrations. It is relevant to say that a lot of research areas which are not focused on bio-sensing might benefit from our results.

In the first part of this chapter we analysed the silicon photonics platform which is used to excite the plasmonic cavity. We numerically approximated the insertion losses in the silicon slab waveguides by end-fire coupling with lensed fibers as well as its sensitivity to alignment errors. We simulated the modes of the slab and the single-mode silicon waveguide. We showed their dispersion diagram and designed the single-mode waveguide to be able to sustain the fundamental quasi-transverse electric (q-TE) mode over the large wavelength range of 1200 to 1700nm. We also showed that the quasi-transverse magnetic (q-TM) mode for the chosen waveguide geometry has a cut-off frequency around 1650nm. The losses for 90° waveguide bends have been calculated in the used wavelength range for different bending radii. The adiabatic tapers losses have also been calculated for different taper lengths in the wanted wavelength range.

After the complete analysis of the waveguide platform needed for the plasmonic slot waveguide cavity (PSWC) excitation, we investigated the characteristic behaviour of a PSWC by analysing it numerically. A modal analysis of the plasmonic slot waveguide (PSW) has been realized which explained the different resonances appearing during the excitation of the cavity. The coupling between the silicon waveguide mode and the PSW has been explained. The modes of the coupled structure which is also called hybrid plasmonic waveguide have been investigated. The coupling length of the structure has been extracted and the Fabry-Pérot like resonance of the PSWC has been explained. The influence of several geometrical parameters of the cavity on the transmittance spectrum has been numerically calculated. A special interest has been shown about the geometrical parameters which could influence the fabrication of the sensor. Moreover, the field enhancement resulting from the excitation of the PSWC has been analysed for different cavity lengths and different metals. It has been found that the coupling strength, which can be changed by the thickness of the SiO₂ spacer layer, can significantly change the sensitivity of the resonance to changes in refractive index of the surrounding medium. A bulk sensitivity of up to 600nm per refractive index unit (RIU) can be achieved with a spacer thickness of 120nm of SiO₂. Moreover, we investigated the change of refractive index induced by a thin layer of varying thickness coated around the PSWC. This calculation was done to simulate the attachment of proteins onto a functionalized PSWC. These results showed to advantage of using the PSWC to detect changes of refractive index in the near field of the cavity.

In the second part of this chapter we fabricated the silicon waveguides patterned by electron beam lithography and etched them with induced coupled plasma reactive ion etching. Then we fabricated the gold PSWC and aligned them on top of the previously fabricated silicon waveguides. Several fabricated samples with different geometries were measured by using a wavelength interrogation method. In a first place, we measured the losses of the silicon waveguides with three different techniques: the cut-back method, the Fabry-Pérot fringe contrast method and the Fabry-Pérot Fourier analysis method. Thanks to the Fabry-Pérot Fourier analysis method we could identify significant losses at the taper interfaces as well as at the 90° bends in the fabricated chips. The propagation losses of the fabricated silicon strip waveguides were measured to be around 13dB/cm. These propagation losses were acceptable for the excitation and the transmittance measurement of the PSWC.

We measured the resonance position of the fabricated PSWC first by calculating the delta of transmittance between the reference waveguide (without PSWC) and the waveguide with a PSWC. The resonance could not be found in these results because of the too strong far-field scattering of the PSWC. Then we analysed the transmittance of the PSWC by normalizing the transmission of the waveguide with a PSWC by the reference waveguide of the same length. In these normalized results we could clearly see the resonance which showed good agreements with the simulated results. We also measured the far-field scattering of the cavity which exhibited a peak at the same resonance wavelength as the transmittance measurements. Finally we measured the resonance position shift induced by the presence of water around the PSWC instead of the air. Because of the fast evaporation of the water droplet, we concluded that a micro-fluidic device should be fabricated on top of the waveguide to perform repeatable and robust measurements of resonance position shifts.

3 Standing wave integrated Fourier transform spectrometer

This chapter is a partial adaptation of the SPIE conference proceeding entitled "Standing wave integrated Fourier transform spectrometer for imaging spectrometry in the near infrared" by G. Osowiecki et al. [145].

3.1 Introduction

Imaging spectrometry is a way of taking pictures with a lot more information than detected in the usual visible wavelength range that our eyes can see. The simple camera on your smartphone, which is based on silicon photodiodes, is recording the intensities of three different colors, the green (50%), the red (25%) and the blue (25%). From the information of only three colors, a color space is reconstructed by interpolation to give the final color of pixels. This has been developed in accordance with the characteristics of the human eye. The human eye is seeing "colors" that are not comparable to spectral data which can provide more detailed information about the light and its origin. An imaging spectrometer will record a full spectrum for each pixel of the image. The image containing all the spectral information is then called a hyperspectral cube. Moreover imaging spectrometers are often recording spectral data in other regions than the visible spectrum. The ultraviolet (UV) or infrared (IR) region can reveal new information of great interest about the type of material from which light is coming. Imaging spectrometers are mostly used for remote sensing applications. The National Aeronautics and Space Administration (NASA) and the European Spatial Agency (ESA) have developed several imaging spectrometers like [146, 147, 148]: "Landsat-8", "AVIRIS", "Hyperion", "ALICE", "MERIS" and "VIRTIS" to cite only some of them, having different missions of inspecting the broad electro-magnetic spectrum from UV to IR. Most of these imaging spectrometers are taking a lot of space and weight, which results in expensive loads in satellites to be launched in space.

In this chapter we present a new architecture of a miniaturized scanning imaging spectrometers based on a standing-wave integrated Fourier transform spectrometer (SWIFTS). SWIFTS spectrometers are based on the recording of a standing wave created by the interference of

two waves [149]. The first attempts to record such a standing wave were made by Gabriel Lippmann who won the Nobel Prize in 1908. He used a thin photographic emulsion with sub-wavelength silver halide grains laying on top of a liquid mercury mirror to permanently record the standing waves created by the different wavelengths of the light coming from a scene [150, 151]. In 1995, inspired by Gabriel Lippmann, Connes and le Coarer presented the potential of this technique to be applied for a 3D spectrometer [152]. The realization of that dream only became reality in 2007 when le Coarer et al. published their results about the first SWIFTS device [153]. Two patents have also been deposited at that time [154, 155]. Different concepts of Fourier spectrometers based on the retrieval of a standing wave have been published by Sasaki et al. [156] as well as Knipp et al. [157]. Nevertheless, the latter concepts do not use the same concept as proposed by le Coarer. They are based on a partly transparent thin-film detector in combination with a tunable silicon micromachined mirror. Their resolution limited by the maximal travel of the MEMS mirror is low compared to a SWIFTS. In the concept of le Coarer, the standing wave will be confined in a single-mode waveguide. The standing wave will be measured by probing its evanescent field at different locations along the waveguide. The concept will be discussed more in detail in the next section. Since 2007 several different studies have explored varying designs and implementations of the SWIFTS. In 2010, J. Ferrand completed a PhD thesis directed by le Coarer in which he modeled a SWIFTS device including all sort of errors needed to be compensated [158]. Very recently researchers from the Photonics Research Group from Uni Ghent have published results about SWIFTS and are adapting it on photonic integrated chips based on silicon or silicon-nitride [159, 160].

This work focuses on the potential of parallelization and miniaturization of the SWIFTS. Moreover, a new mechanism will be investigated which should greatly increase the achievable measurement bandwidth of the spectrometer.

The work shown in this chapter of the thesis resulted from an ESA Technological Research Programme (TRP) (Contract No: 4000104975/11/NL/NA) called Miniature High Performance Imaging Spectrometer for Remote Sensing (Mhipis). The project has been managed by Micos GmbH. The project was a partnership between Micos, Swiss Center for Electronics and Microtechnology (CSEM), Swiss Federal Laboratories for Materials Science and Technology (EMPA).

3.1.1 Standing wave integrated Fourier transform spectrometer principle

The principle of SWIFTS is based on the creation of a standing wave inside a single-mode waveguide. Under ideal conditions, the standing wave results from the interference between two identical superposed waves. The resulting electromagnetic field of that superposition is obtained by the summation of the electric and the magnetic field of both waves. As shown in Fig. 3.1, it can be created in two different manners. It can be either obtained by only one wave which is back reflected by a mirror at the end of the waveguide or the superposition of two

counter propagating waves. The first configuration is called the "Lippmann SWIFTS" named after the Nobel price winner Gabriel Lippmann who invented a way to record colors in a special photographic plate. The second configuration is named the "Gabor SWIFTS" named after the Nobel price winner Dennis Gabor for his invention of holography [161]. For coherent light, the standing wave will result in a sinusoidal light intensity distribution inside the waveguide. For non-coherent light, the interference pattern will only be visible in a length scale comparable to the coherence length measured from a zero path difference (ZPD) position. The resulting interference is called an interferogram.

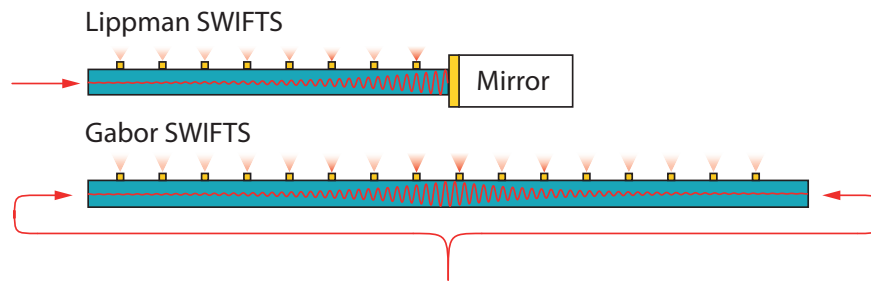


Figure 3.1 – Schematic representations of the Gabor and Lippmann type SWIFTS

We will investigate the first configuration, which is called Lippmann configuration. For this configuration, the optical path difference (OPD) is equal to zero at the mirror surface. Thus if a broad spectrum is injected in the waveguide the center of the interferogram is located at the mirror surface and quickly decays as the OPD increases. Equally spaced nano-samplers in the vicinity of the waveguide will enable the measurement of the interferogram. The nano-samplers will weakly perturb the evanescent wave of the single-mode waveguide and a certain amount of the light will be scattered out of the waveguide. The light scattered out of the waveguide will be proportional to the local intensity of the interferogram at the nano-sampler position. Therefore, by recording the amount of scattered light by all the nano-samplers, we measure a spatially under-sampled interferogram. Ideally the nano-sampler should be infinitely small in the direction of the light propagation. If their size is finite, the light they scatter out of the waveguide will be the averaged intensity of the interferogram over their size. The nano-samplers can be of any kind of material having a different refractive index than the waveguide. But metallic nano-sampler will have a stronger scattering-cross section than dielectric at identical size.

3.1.1.1 Interference fringes in Lippmann SWIFTS

Because of the high frequency of light, the interference resulting from the superposition of two plane waves can only be detected by the intensity of the light at a given point. This intensity is

proportional to the square of the averaged amplitude of the wave [142].

$$I = \frac{c}{4\pi} \sqrt{\frac{\epsilon}{\mu}} \langle \mathbf{E}^2 \rangle \propto \langle \mathbf{E}^2 \rangle \quad (3.1)$$

The modelling of the SWIFTS which takes into account the scattered light of each nano-sampler can be based on the conservation of energy as shown by J.Ferrand in his thesis [158]. In that case, for each nano-sampler, a part of an incident wave will be scattered out of the waveguide and the transmitted wave energy will be reduced.

$$\langle \mathbf{E}_i^2 \rangle = \langle \mathbf{E}_s^2 \rangle + \langle \mathbf{E}_t^2 \rangle \quad (3.2)$$

Where \mathbf{E}_i is the incident wave, \mathbf{E}_s is the scattered wave and \mathbf{E}_t is the transmitted wave.

In that case, the scattering cross-section of one nano-sampler is equal to:

$$\eta = \frac{\mathbf{E}_s}{\mathbf{E}_i} \quad (3.3)$$

We can apply this for a Lippmann SWIFTS having a waveguide of length L and having N equidistant nano-sampler on it. The position of the m^{th} nano-sampler can be found using equation 3.4.

$$x_{ns_m} = x_{ns_1} + (m - 1)\Delta x_{ns} \quad (3.4)$$

Where x_{ns_1} is the position of the first nano-sampler, Δx_{ns} is the distance between two nano-samplers.

The transmitted wave for one nano-sampler can therefore be written in equation 3.6 and the transmitted wave for the m^{th} nano-sampler can be written as in equation 3.8 :

$$\mathbf{E}_t(1, t) = \sqrt{1 - \eta} \mathbf{E}_i(1, t) \quad (3.5)$$

$$\mathbf{E}_t(2, t) = \sqrt{1 - \eta} \mathbf{E}_i(2, t) = \sqrt{1 - \eta} \sqrt{1 - \eta} \mathbf{E}_i(1, t) \quad (3.6)$$

$$\dots = \dots \quad (3.7)$$

$$\mathbf{E}_t(m, t) = (1 - \eta)^{m/2} \mathbf{E}_i(t) \quad (3.8)$$

For a Lippmann SWIFTS, the interfering waves are the initial incident wave coming from the left which we call \mathbf{E}_{left} and the virtual wave coming from the right (from the mirror) which we call \mathbf{E}_{right} . The virtual wave coming from the right has already been attenuated by N nano-samplers.

$$\mathbf{E}_{left}(m, t) = (1 - \eta)^{m/2} E_i e^{i(-\omega t + k(x_{ns_m}) + \varphi_l)} = (1 - \eta)^{m/2} A_L e^{i(\omega t + \varphi_l)} \quad (3.9)$$

$$\mathbf{E}_{right}(m, t) = (1 - \eta)^{(N - \frac{m}{2})} E_i e^{i(\omega t + k(2L - x_{ns_m}) + \varphi_r)} = (1 - \eta)^{(N - \frac{m}{2})} A_R e^{i(\omega t + \varphi_r)} \quad (3.10)$$

With k being the wave-number, φ_l being the phase constant of the incoming wave, φ_r being the phase constant due to the reflection on the mirror, E_i being the electric field amplitude of the incoming wave and L being the length of the waveguide defined by $L = x_{ns_1} + N\Delta x_{ns}$.

The resulting sampled interferogram is equal to :

$$I(m) = \frac{1}{2} A_L^2 (1 - \eta)^m + \frac{1}{2} A_R^2 (1 - \eta)^{2N - m} - A_L A_R (1 - \eta)^N \cos(k(2(L - x_{ns_m})) + \varphi_l - \varphi_r) \quad (3.11)$$

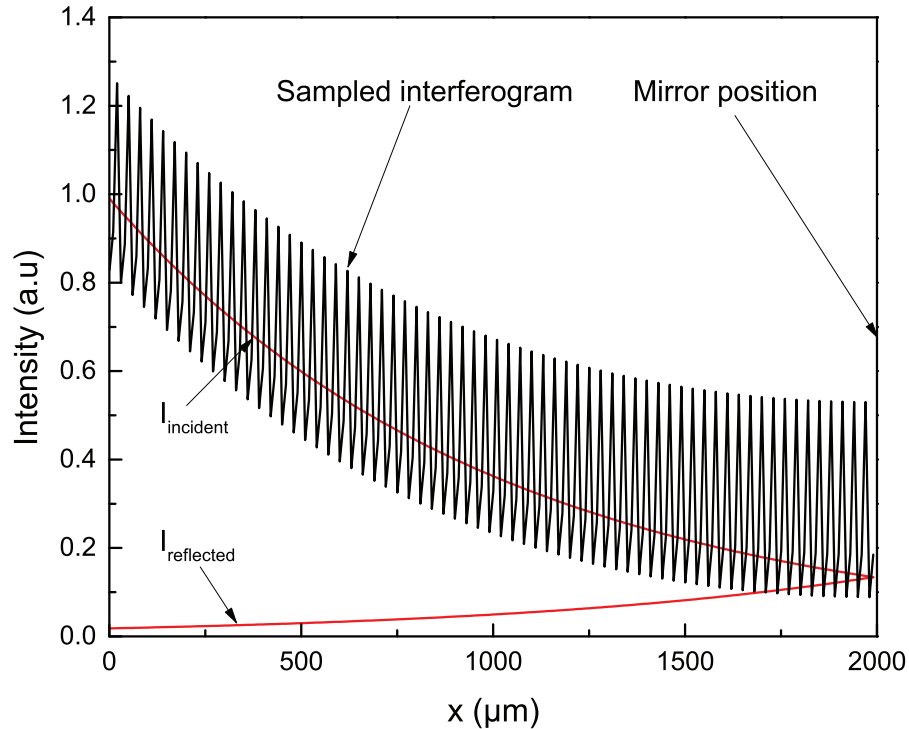


Figure 3.2 – Sampled interferogram of an ideal Lippmann SWIFTS described by equation 3.11. $N = 200$, $\Delta x = 10\mu\text{m}$, $\eta = 0.01$ and $\lambda = 750\text{nm}$. The two decaying red curves are the two first terms expressing the loss of intensity due to the nano-sampler scattering.

We observe that the interference term by itself gives a constant amplitude modulated by the cosinus and that the two first terms are expressing the losses of the light due to the scattering at the nano-sampler. In Fig. 3.2 we show the sampled interferogram obtained by equation 3.11 for an incident amplitude of 1. We set the different constants to the values which will be used later in the experimental results: $N = 200$, $\Delta x_{ns} = 10\mu\text{m}$, $\eta = 0.01$ and $\lambda = 750\text{nm}$. The two first terms of equation 3.11 are plotted in red and show the decay of light intensity during forward and backward propagation due to the scattering at the nano-samplers.

3.1.1.2 Ideal nano-sampler scattering cross-section

The amplitude of the interference term of the standing wave is a function of η . When the scattering cross-section of the nano-samplers becomes too large to few light reaches the mirror, the back reflected light is weak and the interference of the standing wave will vanish. Therefore we might think that the smaller the scattering cross-section is, the better the contrast would be. This is not true because the measured intensity of the light scattered out of the waveguide is equal to $\eta I(m)$. The amplitude of the interference term of $I(m)$ is therefore given by equation 3.12.

$$C(\eta) = 2A_i^2 \eta (1 - \eta)^N \quad (3.12)$$

As shown in Fig. 3.3, this function has a maximum which is located at :

$$\eta_0 = \frac{1}{N + 1} \quad (3.13)$$

This is the ideal scattering cross-section which is maximizing the measured interferogram contrast in the case of a Lippmann SWIFTS. In the example above with $N = 200$, we find $\eta_0 = \frac{1}{201} = 0.005$.

3.1.1.3 Bandwidth and resolution

As we have seen in the previous section, every nano-sampler will scatter a portion of the light to the outside of the waveguide. Therefore, the intensity of the light inside the waveguide will decrease along the propagation path. There will be a trade-off between the intensity of the detected scattered light and the sampling frequency of the interferogram. The spectrum of the light can be recovered by calculating the Fourier transform of the sampled interferogram. In the Fourier domain, the spatial sampling of the interferogram reflects as the attainable spectral bandwidth, while the length of the waveguide reflects as the attainable spectral resolution. The main problem is to measure the standing wave with a high spatial sampling frequency, which

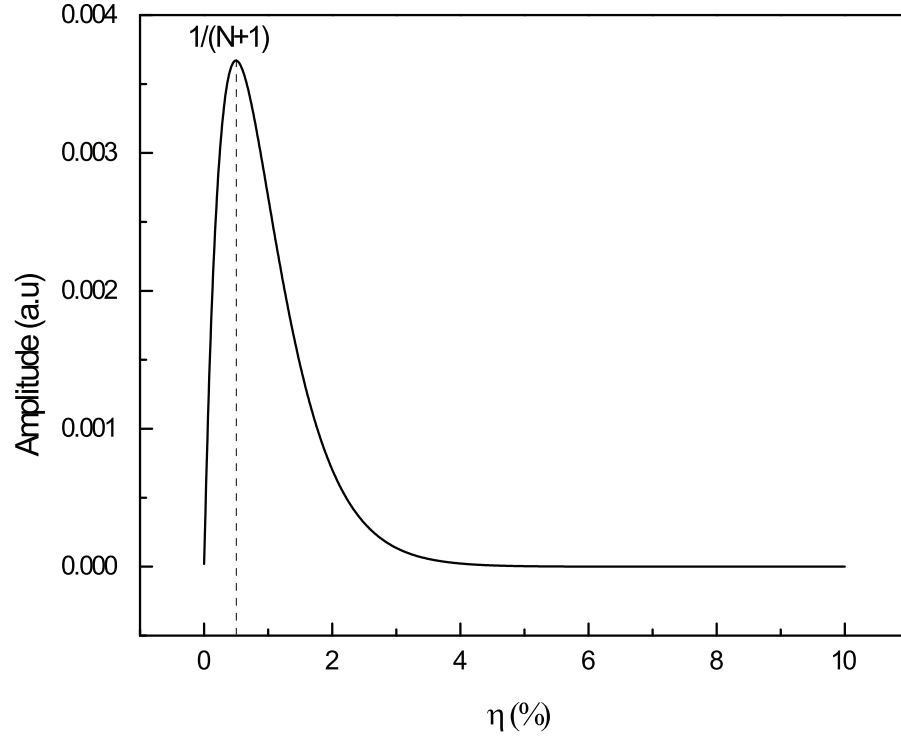


Figure 3.3 – Amplitude of the measured interference term as function of the nano-sampler scattering cross-section.

respects the Nyquist-Shannon sampling theorem. This comes from technical limitations of being able to measure the signal scattered by nano-samplers having a sub-micrometer pitch and also the fabrication of the nano-samplers themselves. Some limiting factors can be the diffraction limit of optical systems or the minimal detector size. Therefore, the standing wave is under-sampled. This leads to a limited bandwidth given by equation 3.14 [158].

$$\Delta\lambda \cong \frac{\lambda}{4n_{eff}\Delta x_{ns}} \quad (3.14)$$

The resolution of the SWIFTS is proportional to the length of the sampled interferogram as shown in equation 3.15 [162]. It also depends on the different apodization used during the Fourier transform [158].

$$\delta\lambda \cong \frac{\lambda^2}{2n_{eff}(N-1)\Delta x_{ns}} \quad (3.15)$$

With currently available technologies, the attainable bandwidth is limited to few nanometers,

while users are generally interested in adopting imaging spectrometers with larger bandwidth. Our research topic in the SWIFTS domain will investigate a solution to overcome this spectral bandwidth limitation. It will be explained in the next section.

3.1.2 Calibration of the non-ideal SWIFTS

In the above sections we described the case of an ideal SWIFTS. In practice, several fabrication errors are leading to a non-ideal behaviour of the SWIFTS. This topic will be treated later in the result section.

3.1.3 The scanning SWIFTS

As discussed in the last section, the measured interferogram will be locally under-sampled, enabling a bandwidth limited to only a few nanometers. This limitation can be overcome by replacing the fixed mirror with a scanning mirror. As shown in Fig. 3.4, by shifting the position of the mirror that back reflects the incoming wave, the interferogram is physically moved with respect to the scattering samplers, thus leading to an increase of the interferogram sampling [163]. The mirror, shown in Fig. 3.4, is moved by a piezo actuator in small nanometric steps for which an image is recorded each time. Thanks to this, we can merge the multiple images acquired during the mirror movement and achieve a much higher sampling frequency of the interferogram and thus extending the bandwidth of the spectrometer. In Fig. 3.4 (right) we show how the sampled interferogram is reconstructed. The obtained interferogram is then post-processed to ensure the proper calibration of the device. Finally, we take the Fourier transform of the post-processed interferogram to show the measured spectrum.

An issue with this approach is to couple enough light back into the waveguide after the reflection at the mirror. Because of diffraction, the divergence of the light beam exiting the waveguide facet leads to a loss of back coupling which is dependent of the mirror's position. That's why a careful calibration needs to be done for each mirror step.

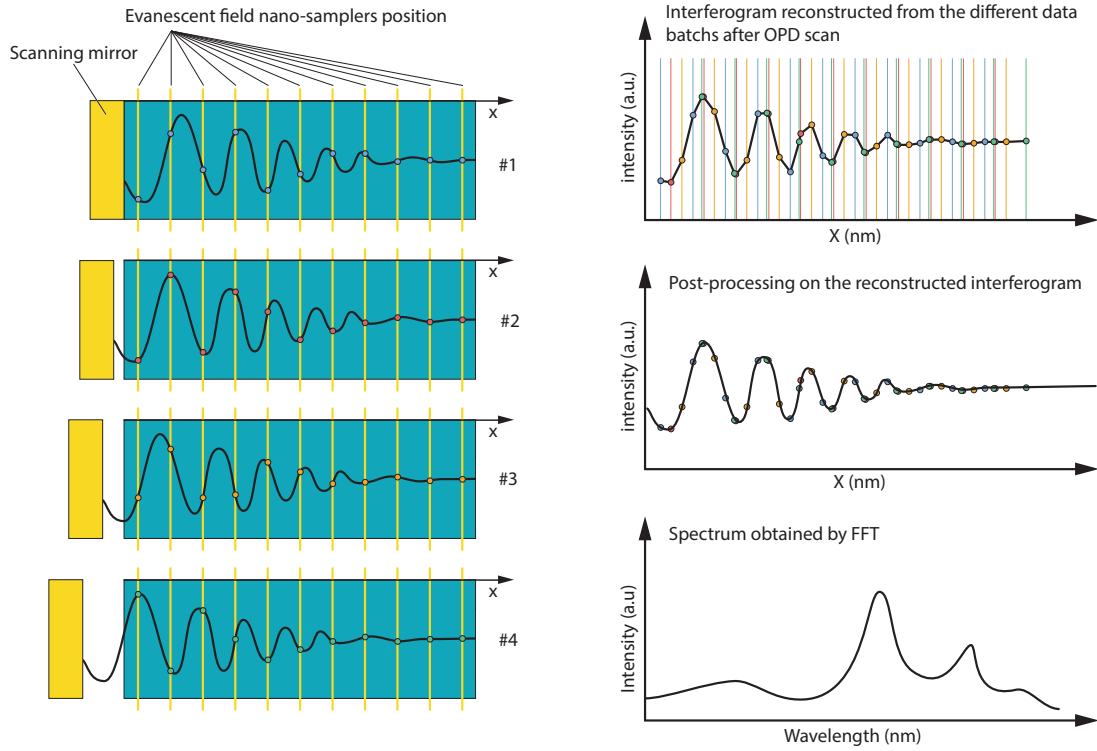


Figure 3.4 – Conceptual sketch of the spectrum retrieval from a scanning SWIFTS. On the left, a waveguide sustaining a standing wave is shown for four different mirror positions. The nano-samplers intensity is recorded for each batch of measurements. The data is recombined in a post-processing step to create the interferogram. The raw interferogram is then numerically post-processed to take into account several errors due to fabrication. The interferogram is then Fourier transformed to find the optical spectrum.

3.2 Objectives

The main objective is to implement a scanning mirror SWIFTS in a prototype having a reduced volume which could simultaneously scan 6 adjacent waveguides. This work should mainly explore new and cost effective fabrication processes leading to a new light injection concept. It should also focus on the miniaturization of the new scanning SWIFTS. Finally, it should qualitatively show some results of the working device.

We focus on the detection within the wavelength range from 750nm to 775nm, with 0.12nm spectral resolution, with system level requirements approaching those of an imaging spectrometer for atmospheric studies and operating in the Oxygen-A band. The spectral resolution defined the minimum length of the sampled interferogram. For 0.12nm spectral resolution, at least a length of 1 mm must be sampled. The nano-sampler pitch will be of 10 μ m. The mirror maximum travel is planned to be around 15 μ m. We based the scanning SWIFTS on polymeric waveguides made out of EpoCore material from Micro Resist Technology GmbH. We expect that these polymeric waveguides have low losses. Their low Δn makes it possible to create a large single-mode waveguide in which it is possible to inject light more easily. The light injection in the single-mode waveguides is planned to be done with special in house fabricated micro-lenses made out of photoresist.

3.3 Approach, Methods and tools

First, we will treat the modelling and optimization of individual parts of the scanning SWIFTS. Second, we will detail the fabrication process of the scanning SWIFTS.

3.3.1 SWIFTS design

The scanning SWIFTS is made out of different parts: the single-mode waveguide, the nano-samplers, the injection optics and the scanning mirror. Here we will describe in detail each of these components.

3.3.1.1 Single-mode Epocore waveguides

The embedded waveguides are based on a negative epoxy-based photoresist called EpoCore and EpoClad. At 850nm, the EpoCore has a refractive index of 1.58 and is used as the core material of the waveguide. At the same wavelength, the EpoClad has a refractive index of 1.57 and is used as the cladding material. Both "Epo" photoresists are transparent from 400nm to 1600nm. As shown in the band diagram in Fig. 3.5, we designed a rectangular waveguide of 3 μ m width and 2 μ m height which is purely single-mode and is supporting the fundamental quasi-transverse electric (q-TE) mode for wavelengths longer than 689nm. For wavelengths between 552nm and 689nm, the waveguide can sustain the fundamental q-TE mode and the fundamental quasi-transverse magnetic (q-TM) mode.

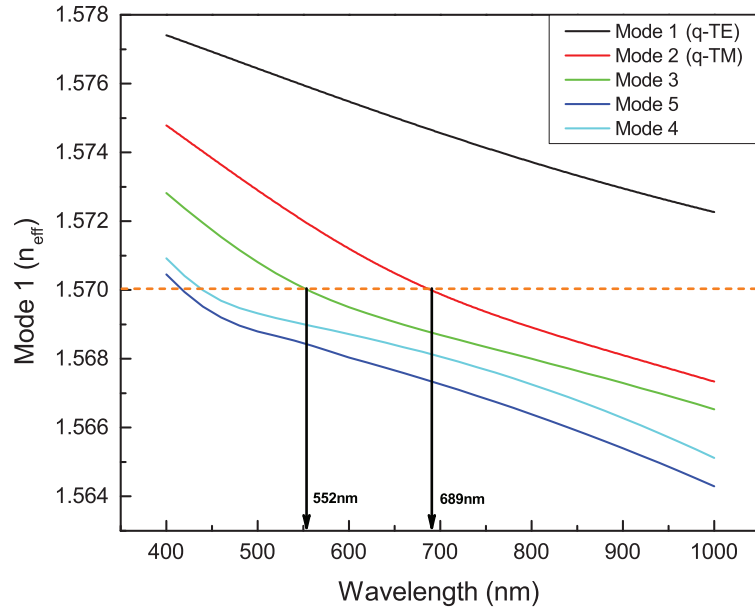


Figure 3.5 – Band diagram of an EpoCore waveguide having a width of 3 μ m and a height of 2 μ m.

In Fig. 3.6 we show a simulation of the amplitude of the electric field distribution at 762.5nm.

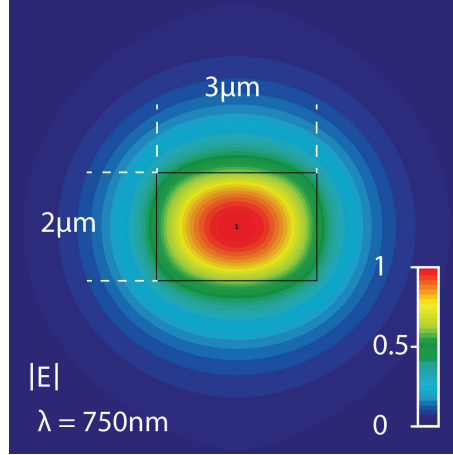


Figure 3.6 – Electric field amplitude of EpoCore single-mode waveguide at $\lambda = 762.5\text{nm}$ simulated with CST Microwave Studio (CST MWS) mode solver. $n_{core} = 1.58$; $n_{clad} = 1.57$, $n_{eff} = 1.574$.

The effective index of the mode at 762.5nm is equal to $n_{eff} = 1.574$. For the scanning SWIFTS, we will assume that this value is constant. For longer wavelengths, the mode will be less confined in the core of the waveguide and for shorter wavelengths more confined.

EpoCore waveguide parameters	
Type	Embedded
NA (in air)	~ 0.18
n_{core}	1.58
n_{clad}	1.57
n_{eff}	1.574
Geometry	$3 \times 2\mu\text{m}$

Table 3.1 – EpoCore waveguide parameters.

3.3.1.2 Design of the Injection optics

It is a real challenge to inject light efficiently into a single-mode waveguide. This comes from the conservation of the etendue which needs to be respected. We tackled the problem by choosing a micro-lens to inject the light into the single-mode waveguides. The micro-lenses will enable us to have several adjacent waveguides next to each other separated by a distance of either $150\mu\text{m}$ or $250\mu\text{m}$. Because of the etendue conservation, the acceptance angle of the incoming light illuminating the micro-lenses is very small if we want to conserve a good injection efficiency. The scanning SWIFTS will be illuminated by a collimated laser beam to inject light efficiently into at least six adjacent waveguides. In Fig. 3.7, we show the ray trace results of the designed micro-lens. If the micro-lens is illuminated by a plane wave the diameter of the Airy disc at its first zero will be given by $A = 1.22\lambda \frac{z}{r}$ and will be equal to about $7\mu\text{m}$ for $\lambda = 750\text{nm}$. We can therefore already say that the mode field diameter (MFD) of the

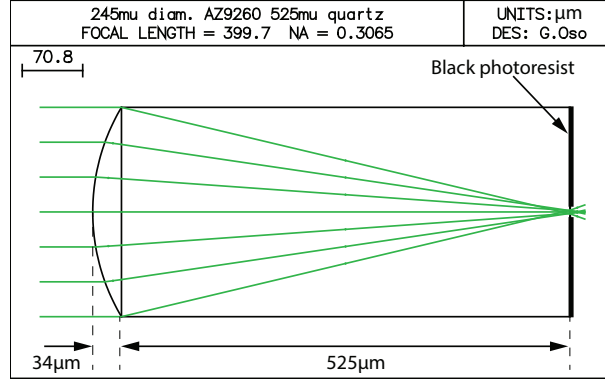


Figure 3.7 – Ray trace with Oslo free educational version of a 245µm in diameter micro-lens focusing on the backside of its substrate.

waveguides should be increased in the future. This can be achieved by decreasing the Δn between core and cladding index of the waveguide.

Because of the intrinsic limited fill-factor of a micro-lens array, some light can pass through the array in between the lenses. This light can be coupled into the chip and perturb the readout of the spectrometer. Therefore, the backside of the micro-lens array will be coated with an opaque layer which will feature apertures of 10µm of diameter centered with each micro-lens to avoid the coupling of light into the cladding of the waveguides. The opaque layer will be made out of a either chrome or black photoresist.

3.3.1.3 Design of the nano-samplers

The required spectral bandwidth we want to cover is between 750nm to 775nm. In that case, the period at which we should place the nano-samplers (array of antenna) to respect the minimal sampling frequency is equal to $T = 3.6\mu\text{m}$ according to equation 3.16 when the effective index of the waveguide is 1.574.

$$T = \frac{\lambda_{min}\lambda_{max}}{4n_{eff}(\lambda_{min} - \lambda_{max})} \quad (3.16)$$

In equation 3.16, the effective refractive index is assumed to be constant through the bandwidth and should be taken at the central wavelength (i.e. 762.5nm). This means that in the case a line array camera is used in conjunction with a direct optical system to record the scattered light intensity its pixel size should be similar or smaller than this period.

3.3.1.4 Summary of the designed scanning SWIFTS

The Fig. 3.8 shows a draft of one channel of our designed chip, including the micro-lens, the waveguide with nano-samplers and the mirror. All the elements are now designed according to the specifications we have set in our objectives. The next step of the work is the fabrication of the chip that will be explained in detail in the next section.

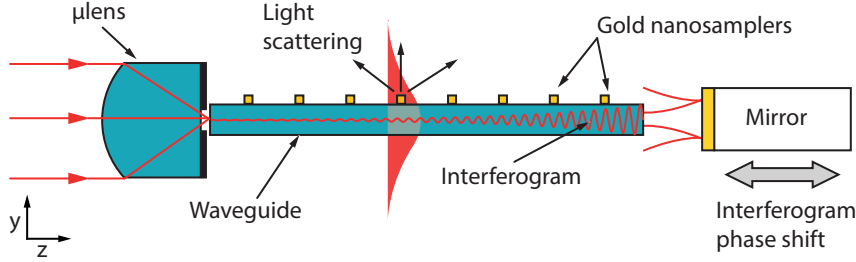


Figure 3.8 – Sketch of the Lippmann SWIFTS configuration with a moving mirror. This allows to increase the sampling frequency of the interferogram, in other terms allow to acquire spectra with larger bandwidth with respect to the static configuration.

3.3.2 Fabrication

The scanning imaging SWIFTS chip consists of the injection micro-lenses, the core waveguide chip with its gold nano-samplers and a custom made gold mirror. Here we quickly review the fabrication process of all these elements.

3.3.2.1 Micro-lens fabrication

The micro-lenses are fabricated on a quartz substrate having an array of apertures of $10\mu\text{m}$ in diameter on the backside [164]. We fabricated these apertures with two different techniques. In a first approach, these apertures were fabricated with a lift-off technique using a 150nm chrome layer (10x the penetration depth at 800 nm). In a second approach we used a special black photoresist named "Everlight EK 410" as replacement of the chrome. This reduces the number of steps needed during the fabrication. Alignment marks are also present on the backside to be able to align each aperture to each individual micro-lens. In Fig. 3.9(a) we show the fabricated micro-lenses with chrome apertures in an epi-illumination and on Fig. 3.9(b) in a dia-illumination where the aperture can be seen.

The micro-lenses are made out of AZ9260 photoresist having a refractive index of about $n_{lens} = 1.6$ at 800nm. The glass substrate is coated with a 600nm thin base layer of AZ1518 which is then backed at 160°C for an hour. A top layer of AZ9260 having a thickness of $22\mu\text{m}$ is then coated on top of the base layer. This second layer is patterned with photolithography in cylinder shapes having a diameter of $245\mu\text{m}$. These cylinders are then molten above the glass transition temperature to be transformed into lenses at 150°C . In a further step it is possible to

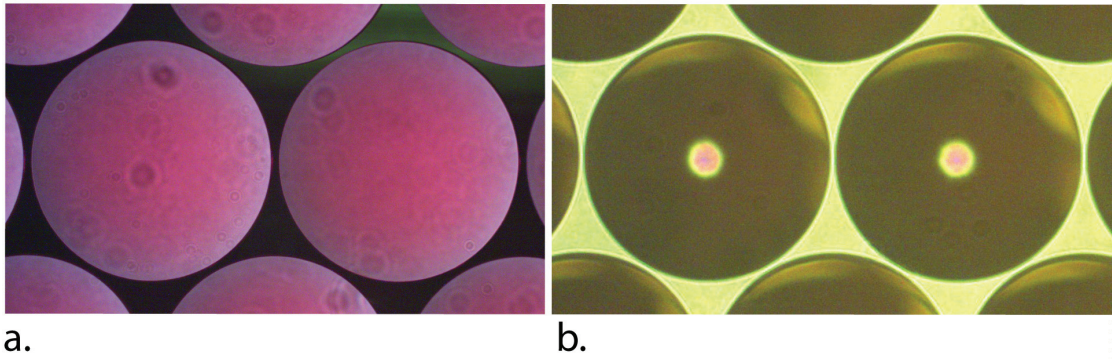


Figure 3.9 – (a) Image of the fabricated photoresist micro-lenses with their backside black photoresist. Epi-illumination. (b) Same image with dia-illumination showing the 10µm apertures through the black photoresist positioned in the back focal plane.

etch them into glass, if needed.

3.3.2.2 Scanning SWIFTS chip fabrication

Fig. 3.10 shows a step by step fabrication process of the scanning SWIFTS chips. The waveguide chip is realized on a 500µm thick glass substrate (D263 Schott). On top of the substrate, the waveguides and the cladding are made out of EpoClad and EpoCore epoxy-based UV photosensitive negative resist from Micro Resist Technology GmbH. The nano-samplers were realized thanks to electron beam lithography (EBL) by Dr. Ivan Shorubalko at EMPA. The entire fabrication process is based on a mix & match process which combines two different lithography techniques.

Bottom cladding The first step consist of the creation of the upper cladding. It is done by coating the glass substrate with a 5µm thick EpoClad layer followed by a flood exposure to cross-link the polymer. All the details of the processing of the Epo negative photoresist can be found in the appendix A.1.3.

Nano-samplers In a second step, the nano-samplers are patterned by EBL. A 70 nm layer of Poly(methyl methacrylate) (PMMA) 950K : Ethyl Lactate 2:3 is deposited on top of the EpoClad layer by spin-coating it at 2000rpm. This is followed by an evaporation of 8 nm of copper to make the surface conductive and suitable for EBL. Nano-samplers having a size of 50 nm (width) x 20 nm (height) x 8 µm (length) are patterned at 30 kV on a Raith 150 EBL system. The aperture is set to 10µm given a beam current of 40pA. The step size is set to 5nm and the write field to 200µm. The nano-samplers are exposed as lines with a dose of 1000pC/cm. After exposure, the conducting copper layer is dissolved in a solution of HNO₃:H₂O 1:30 for 1min. The exposed PMMA is developed in a solution of Methyl isobutyl ketone (MIBK):Isopropyl alcohol (IPA) 1:3 during 1min followed by a 30sec rinsing with IPA. After development of the

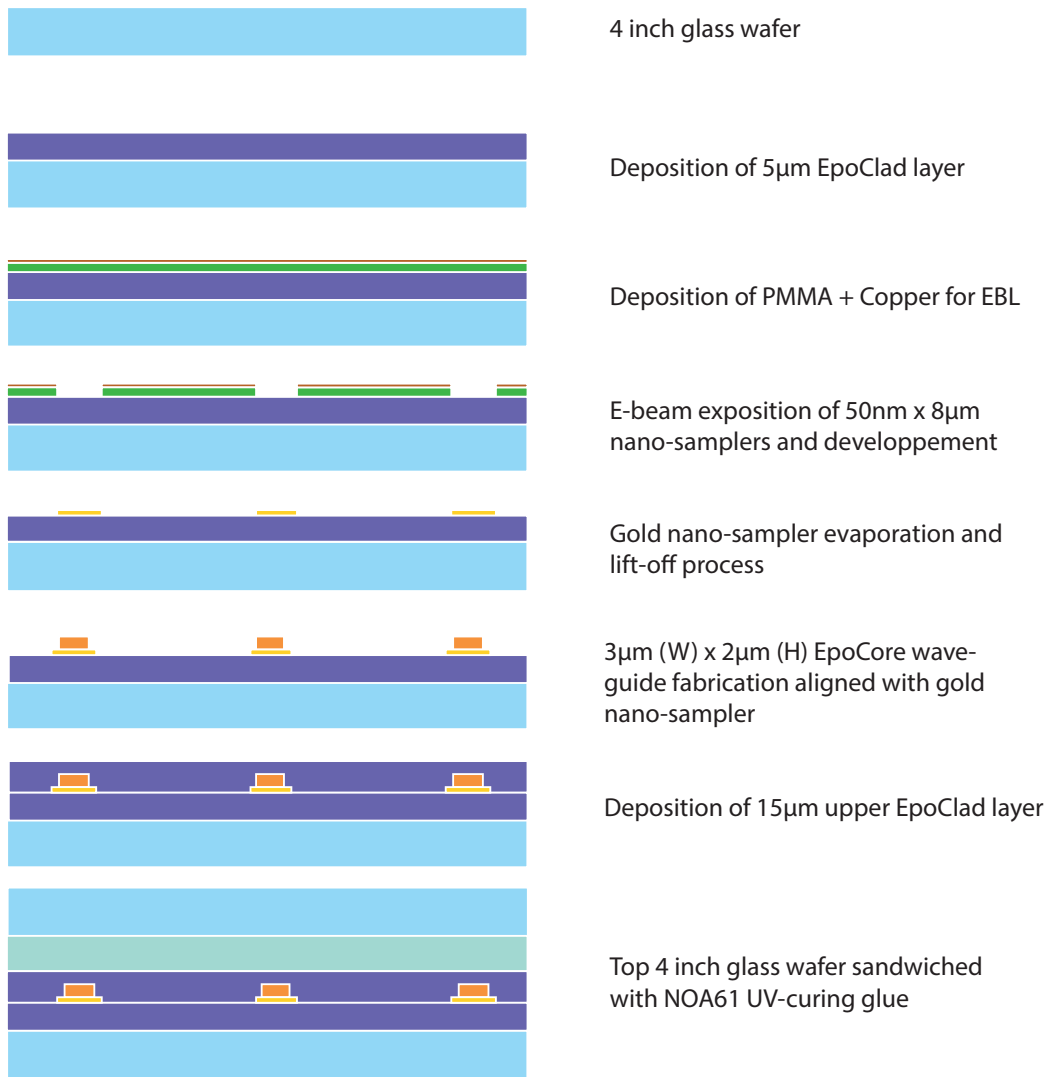


Figure 3.10 – Sketch of the different fabrication steps of the waveguide chip of the SWIFTS spectrometer.

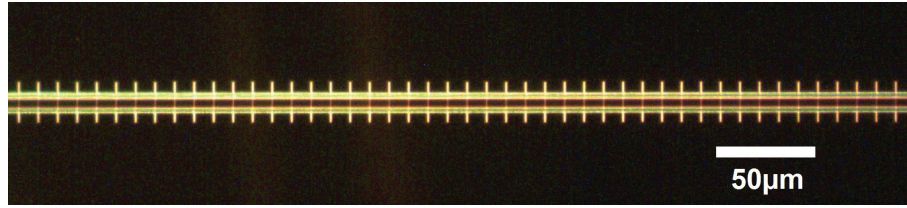


Figure 3.11 – Gold nano-samplers fabricated by EBL with aligned EpoCore waveguide on top.

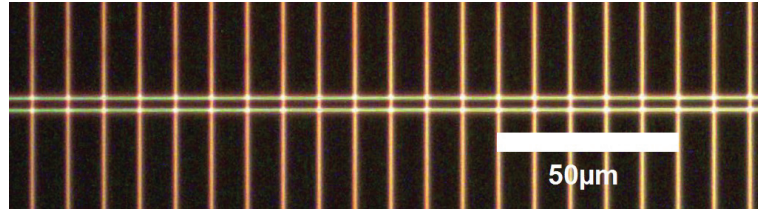


Figure 3.12 – Continuous gold nano-samplers fabricated by EBL with EpoCore waveguide on top. No need for alignment in that case.

exposed PMMA a O₂ plasma descum is realized to clean the PMMA residues. A 2nm thick layer of Ti to enhance the adhesion of the gold is evaporated on the sample. It is followed by a 20 nm gold layer evaporation. The PMMA is then lift-off in an acetone bath help by a short ultrasonic excitation. Fig. 3.11 shows an EpoCore waveguide aligned to the previously EBL fabricated nano-samplers. We also fabricated some continuous nano-samplers to avoid the alignment step. They could be fabricated on large scales thanks to interference lithography technique which is a low-cost process compared to EBL. Fig. 3.12 shows these continuous nano-samplers fabricated by EBL with an EpoCore waveguide on top of them.

EpoCore waveguides The next step is to pattern the waveguide made out of EpoCore [165]. This is done by spin-coating a 2µm thick EpoCore layer on top of the nano-samplers, exposing it after precise alignment of the photolithographic mask with the nano-samplers and developing it (see appendix A.1.3 for further details).

EpoClad upper cladding These waveguides are then covered by a spin-coated 15 µm thick EpoClad cladding, which is cured by UV light.

Sandwich bonding Because of further end-facet polishing problems a second glass substrate needs to be glued on top of the stack. This is done with a spin-coated layer of NOA-61 UV curing glue. Before applying the NOA61, the layer of EpoClad needs to be activate with a short O₂ plasma to increase its adhesion to the NOA61. Once the liquid NOA61 layer is spin-coated on the new glass wafer, both wafers are glued together and put into a plastic bag used normally for the vacuum packaging. By using a standard vacuum packaging machine, the bag is evacuated and both wafers are compressed against each other. The bag is then put into a

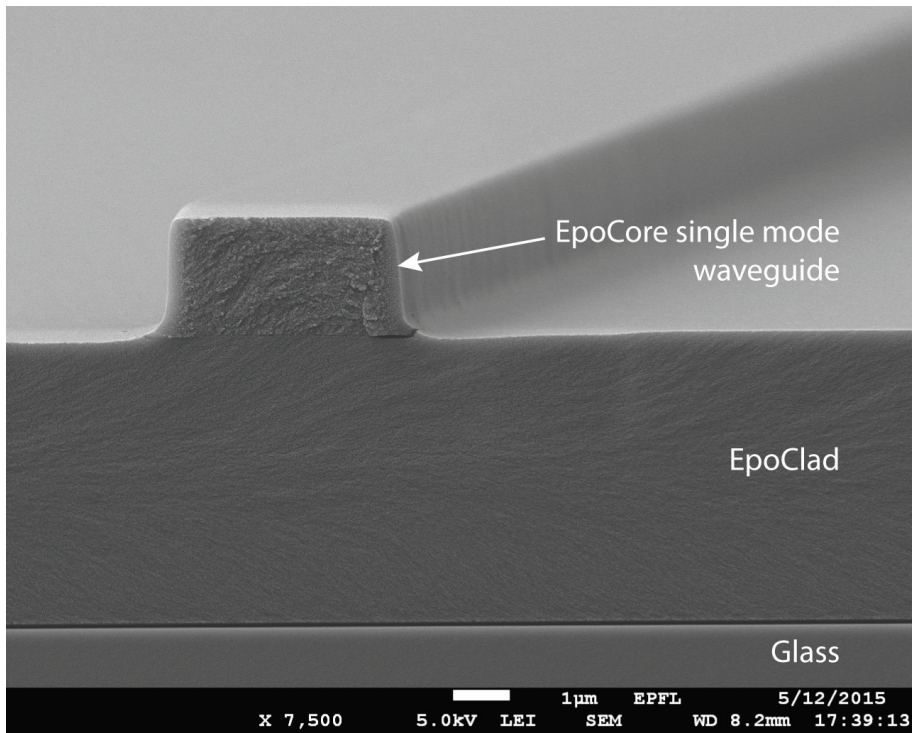


Figure 3.13 – scanning electron microscope (SEM) image of fabricated EpoCore single-mode waveguide.

UV light box to cure the NOA61. With this technique it is possible to avoid the formation of any bubbles in the NOA61 layer.

Facet polishing Finally, the wafers are cut in chips on a MicroAutomation 1006A dicing saw. The chips are cut into dimension of 5mm x 10mm following the alignment marks done in the EBL step. Each individual chip is then polished on both waveguide facet side down to a diamond grain size of 0.01µm. After the polishing the chips are cleaned in an ultrasonic bath containing an alkaline solution of Deconex (Soap).

3.3.2.3 Alignment of the of the micro-lenses

The micro-lenses are aligned to the waveguide facet to maximize the light injection under collimated injection at 660nm of wavelength. A special experimental setup has been build for this purpose. The SWIFTS chip is fixed and the micro-lenses are attached to a 6-axis precision alignment stage. The alignment stage is located under a microscope to verify that the facet of the waveguides are parallel to the back surface of the micro-lenses. The output of the waveguides is imaged by a microscope objective to assess to XYZ alignment. Before starting the alignment, a small amount of low-shrinkage UV-curing glue (Dymax OP-4-20632-GEL) is poured onto the chip facet. The transparent glue is almost index matched to the glass. It has a

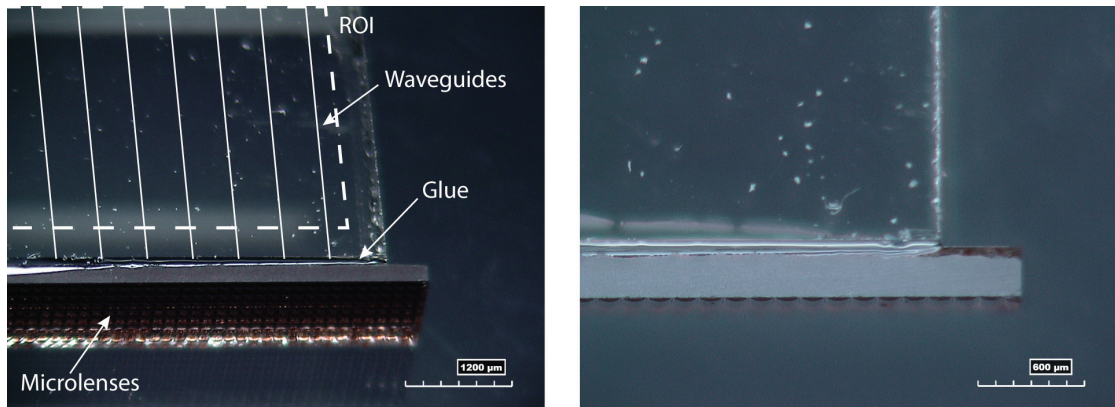


Figure 3.14 – Scanning SWIFTS chip ready to be implemented into the mechanical setup with the moving mirror. The images are showing the integration of the micro-lenses onto the facet of the SWIFTS chip.

viscosity that allow it to stick to the sample. The glue is wetting the surfaces onto which it is put, therefore not glue should touch the upper or lower surface of the SWIFTS chip. Once the alignment is perfect, the glue is polymerized by UV light. The result of the final chip is shown in Fig. 3.14. If you are curious, you can have a look at the video we uploaded on Youtube, which is showing the final chip (<https://youtu.be/PFQQEn9znFw>).

3.3.3 Experimental set-up

The whole spectrometer prototype is shown in Fig. 3.15. Several improvements have been added to the setup since its first version. We will comment on them in later sections. The aim of the optical setup is to image the chip in a 2 by 2mm field of view to be able to collect the light emitted by the nano-samplers of at least six adjacent waveguides in a single image. As explained in the objectives, we had specific requirements concerning the size of the final device. The experimental setup that we will describe in the next paragraph is aimed to be a first demonstrator. This size limitation of the demonstrator created a lot of undesired alignment problems which we could have avoided.

3.3.3.1 Optical read-out of the sampled interferogram

We opted for a SBIG cooled charge-coupled device (CCD) camera as an imaging sensor. We wanted to have a highly sensitivity camera to detect the scattered light even in non ideal conditions and to be able to use the whole dynamic range of the camera. The amount of recorded intensity levels will directly affect the signal-to-noise ratio of the measurement. The camera is an SBIG ST-8300 using a Kodak micro-lensed KAF-8300 CCD sensor with 3326 by 2504 array of 5.4μm square pixels. A 16 bits A/D converter renders the intensity levels of each pixel. The sensor can be cooled with a delta reduction of 35°C for a reduction in CCD dark current. The camera readout time for one full sized image is 3 seconds. We used an inverted

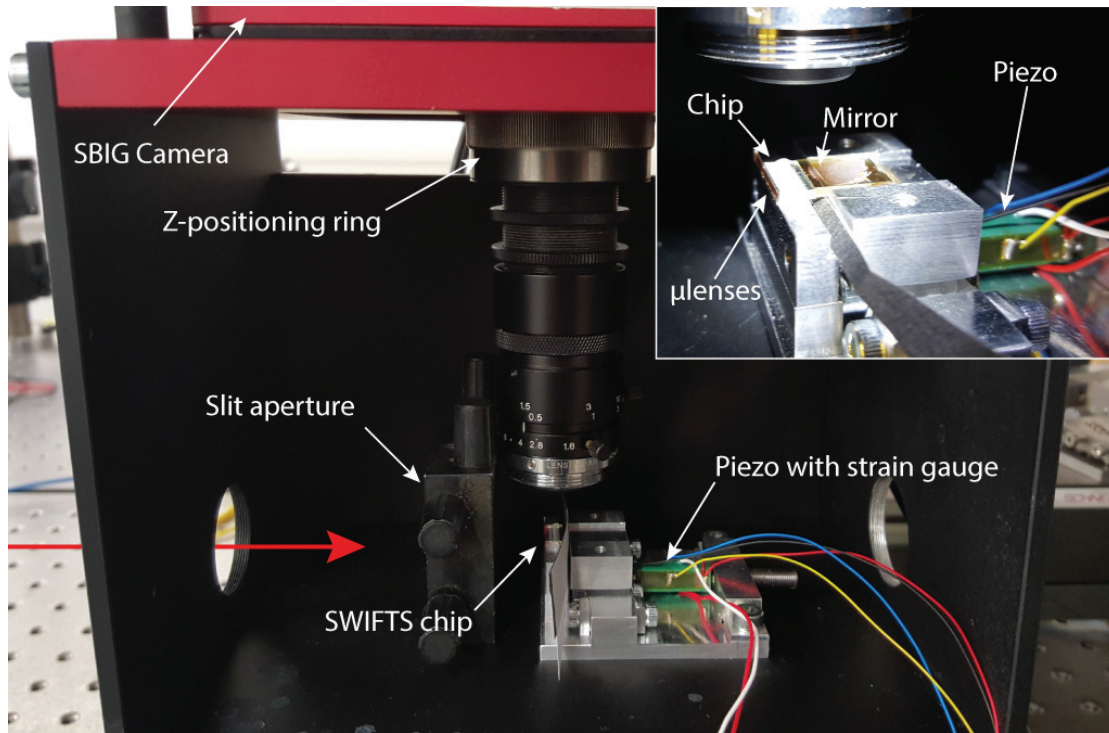


Figure 3.15 – Image of the complete spectrometer setup including the camera and objective that are imaging the planar nano-cavities located on top of the waveguides. The mirror is driven by a closed-loop piezo actuator.

C-mount format camera objective (MVL12L from Thorlabs) having a focal length of 12mm to image the chip onto the CCD. The depth of field of the optical system taking images of the nano-sampler scattering is very narrow because we use an F-number of 4 ($NA = 0.125$) to collect a maximum of light with the camera. In the first optical design of the setup, we placed a beam splitter between the objective and the camera to have a live view on the sample. This saved us a lot of time for every adjustment since we had no camera live view. The chip holder had been designed so that the chip would be in focus when gluing it on it. Since the objective was inverted, we had problems of focusing. The range in which we could change the focus on the objective was too small. Moreover, the reference height of the chip was varying from chip to chip. Therefore we finally have chosen to replace the eyepiece and the beam splitter by a Z-axis positioning ring. The advantage of having a large focus adjustment range exceeded the drawback of losing the live view on the system. The main focus here is to keep the final system compact.

3.3.3.2 The scanning mechanical setup

The scanning SWIFTS device is mounted on a small mechanical setup which is shown in Fig. 3.16. It is made out of the fixed chip holder part and the moving mirror holder part. The mirror holder part is suspended onto four metallic flexure beams and is driven by a piezo-electric

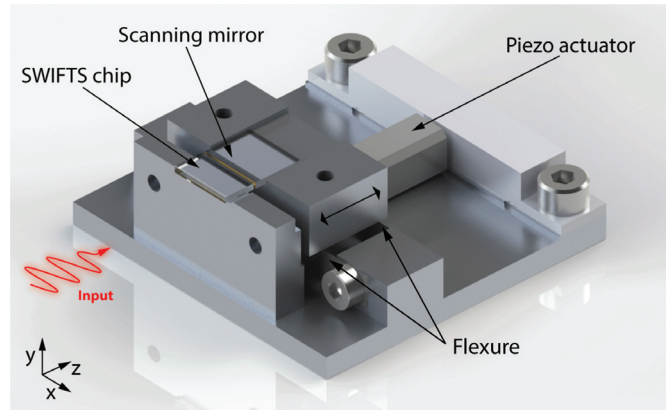


Figure 3.16 – 3D drawing of the chip holder including the scanning mirror driven by a piezo actuator.

actuator fitted with a strain gauge for closed-loop operation. The closed-loop piezo actuator has been measured in a Michelson interferometer to calibrate the absolute travel of the piezo. The absolute position accuracy has been measured to be in the order of $\pm 10\text{nm}$. The chip is glued with UV-curing glue onto the chip holder. Once the chip is fixed, the mirror needs to be perfectly aligned to the chip facet to achieve a minimal gap and a perfect parallelism between both faces. This is done with the help of the gravity by putting the mirror in equilibrium onto the facet of the chip. Once the mirror is positioned, the low shrinkage UV-curing glue is polymerized to fix the mirror. The whole step of fixing the mirror is done with the piezo actuator at maximal extension so that when decreasing the piezo voltage, the gap between the mirror and the chip facet increases up to $17.4\mu\text{m}$. To reduce the stray light collected by the optical system, a slit aperture is placed in front of the micro-lens array which restricts the illumination to the line array of micro-lenses. We experience some problems with unwanted reflections close to the first nano-sampler position. These are coming from the mirror itself and are difficult to be avoided. The upper edge of the mirror should be at the same height than the waveguides. If it is a bit higher, we will see a reflection of the first nano-samplers in the mirror. Other perturbations are coming from the scattering of the edge of the chip and the mirror which are not perfectly smooth. The information carried by the first nano-samplers is of highest importance when measuring a spectrum having a large spectral range since the interferogram has no more signature contrast after a couple of micro meters.

3.4 Results

Several chips with different properties were fabricated and measured. All the chips had a nano-sampler pitch (Δx_{ns}) of $10\mu\text{m}$. The pitch has been defined according to the maximum travel of the mirror, the effective index of the waveguide and the resolution of the observation system. The maximum OPD_m induced by the mirror should be at least corresponding to the OPD_{ns} between two nano-samplers ($N_{ns} = 1$). The OPD is defined for free space and equation 3.17 gives the OPD for the light inside the waveguide between two nano-samplers according to its effective index.

$$OPD_{ns} = N_{ns} \Delta x_{ns} n_{eff} = 15.74\mu\text{m} \quad (3.17)$$

$$OPD_m = N_m \Delta x_m \quad (3.18)$$

The OPD_{ns} between two nano-samplers ($N_{ns} = 1$) is equal to $15.74\mu\text{m}$ at central wavelength of 762.5nm . The effective index of the TE mode at this wavelength is $n_{eff} = 1.574$. The OPD_m induced by one mirror shift is given by equation 3.18 where Δx_m is the fixed mirror step size and N_m the number of mirror steps. We have seen that the scanning mirror in our setup has a maximum travel range of $17.4\mu\text{m}$. This is more than the required $15.74\mu\text{m}$ needed to induce an OPD which enables the full sampling of the interferogram.

Each chip had to pass through different steps of calibration measurements which were done in MATLAB. These steps will be explained in the next sections and are only applied to frequency information given by the spectrometer. No photometric calibration of the spectrometer has been done.

The sampling of the interferogram is done by placing N_{ns} nano-sampler equally spaced by Δx_{ns} on the waveguide in the first place. Then, the mirror is shifted by N_m steps of Δx_m . The raw measurement is a data-set of uncompressed 16bits TIFF grayscale images recorded by the SBIG camera. In this data-set each recorded image corresponds to a specified mirror position. The scanning procedure starts with the mirror at its closest position to the waveguide facet and then moves away from it with a constant minimal step size of 20nm . As the maximum mirror travel corresponds to $17.4\mu\text{m}$, the largest data-set will results in 871 images. The mirror can be moved with larger step sizes if needed. In the experiments we realized, we used the minimal step size of 20nm to characterise the SWIFTS with the highest sampling frequency. The needed step sizes of the mirror movement are defined by equation 3.14 on page 87 and are dependent on the bandwidth of the measured spectrum. The complete interferogram recorded with a phase shift induced by the mirror movement is a convolution of a rectangular function (the N_m mirror steps) with a dirac comb (the nano-samplers). In the Fourier domain,

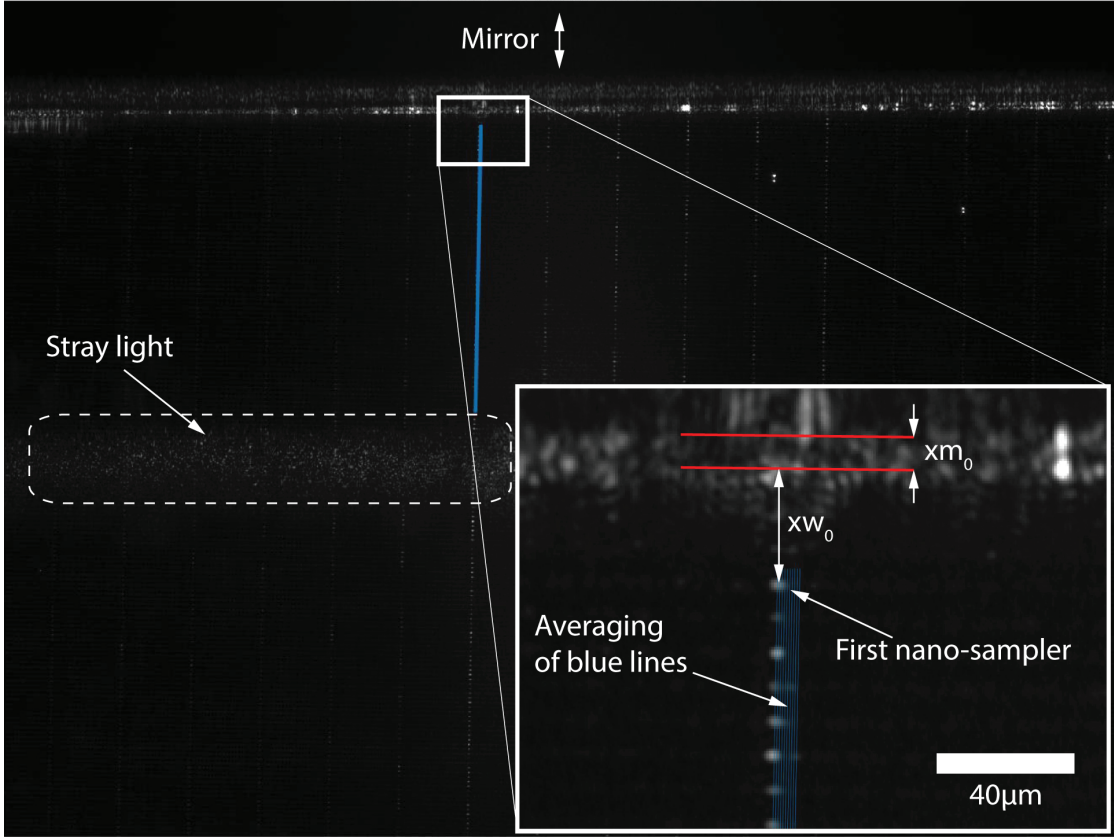


Figure 3.17 – Typical image acquired by the SBIG camera showing the sampled interferogram of six adjacent waveguides. The mirror is on the top. We show how we defined the minimal mirror gap (xm_0) and the distance of the first nano-sampler to the waveguide facet (xw_0). The average value of the blue lines is used to calculate the spectrum.

this results in a multiplication of a Sinc function with a dirac comb. To avoid spectral leakage in the fast Fourier transform (FFT), the dirac comb in the frequency domain needs to fall on the zeros of the Sinc function. Therefore, the mirror step size (Δx_m) and the number of mirror displacement steps (N_m) should fulfill the condition given by equation 3.19. This would result in taking 787 samples separated by $\Delta x_m = 20nm$ with $n_{eff} = 1.574$. This spectral leakage is very sensitive to the mirror displacement error and rely on the accuracy of the calculated effective index of the waveguide. In the case of displacement errors, we will see replications of the spectrum located in the side lobes of the Sinc function.

$$N OPD_{ns} = N_m OPD_m \quad \text{for } N \in \mathbb{Z}^* \quad (3.19)$$

In Fig. 3.17 we show the image number 1 with minimal mirror gap. It shows the under-sampled interferogram of six adjacent waveguides. In this image the mirror is on the top. In the middle

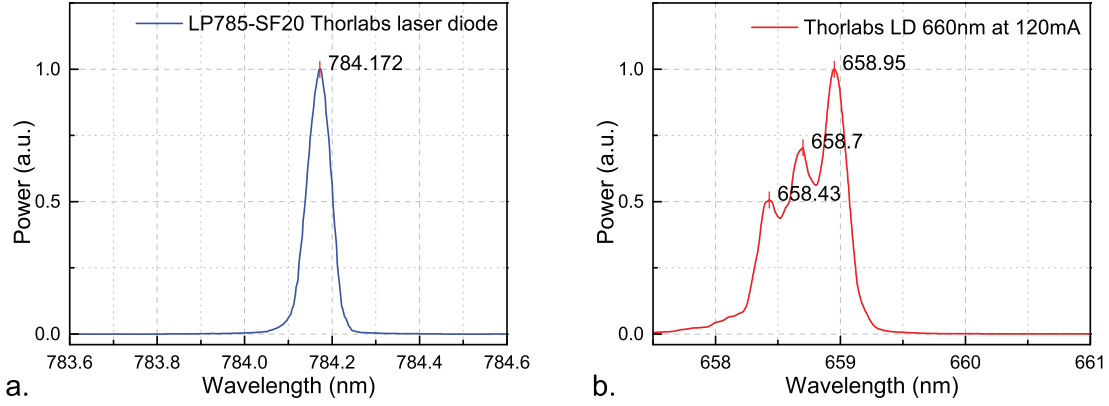


Figure 3.18 – a. Spectrum of the LP785-SF20 laser diode. b. Spectrum of the LP660-SF60 laser diode. The resolution of the spectrum is 0.01nm.).

of the image we can notice some stray light which is perturbing the image. This is typically one of the problems we encountered in our demonstrator setup. The problem is that we cannot remove the affected data points from the interferogram without affecting the result of the discrete Fourier transform. In the future the stray light could be reduced by anodising the aluminum piece of the setup in black and take care of blocking the unwanted light. This first image of the scanning SWIFTS chip is used to measure the minimal mirror gap (xm_0) and the position of the first nano-sampler (xw_0) with respect to the waveguide facet. These length are important to calculate the real optical path difference of our measured samples. The blue line shows the profile on which the peaks of maximum intensity are searched. The extracted profile from the blue line is an average of 5 adjacent lines. The location of these peaks will be recorded and reused in all the next post-processed images.

3.4.1 Calibration light sources

The first experiment will be to measure the spectra of two well defined monochromatic light sources. As their spectrum is well known, they can be used for calibration purposes of the spectrometer. At the beginning of the project we planned to use two different laser diodes from Thorlabs. One in the visible at 660nm (Thorlabs LP660-SF60) and one close to the central wavelength of our baseband at 785nm (Thorlabs LP785-SF20). The two spectra of these laser diodes are shown in Fig. 3.18. From these spectra we can see that the 660nm laser diode is not mono-mode.

When we recorded the interferogram for these laser diodes we immediately noticed that they were mode hopping. We recorded a video of the sampled interferogram which changes at each mode hop of the laser diode. It can be seen on Youtube be following this link (<https://youtu.be/cUWvaforMtk>). As these light source are intended to be used for calibration, we needed to find other alternatives. We finally injected a helium-neon (HeNe) laser emitting at 632.8nm and a tunable external-cavity laser diode (SDL-8630) emitting around 789nm.

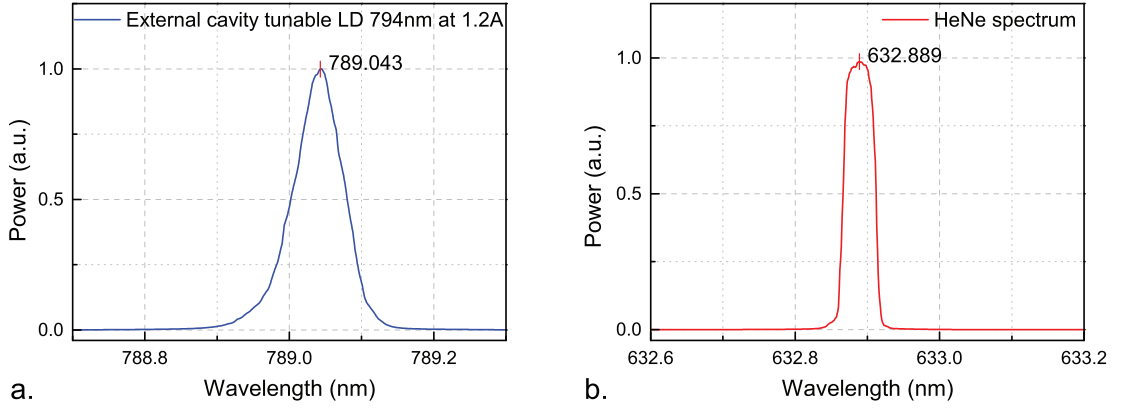


Figure 3.19 – a. Spectrum of tunable external-cavity laser diode (SDL-8630). b. Spectrum of the HeNe laser. The resolution of the spectrum is 0.01nm.

Their spectra are shown in Fig. 3.19. Another alternative that we didn't chose to follow would have be to invest in a distributed feedback laser (DFB) diode which is single-mode and cannot mode hop.

3.4.2 The recorded interferogram

From the chip shown in Fig. 3.17, 153 nano-samplers ($\Delta x_{ns} = 10 \mu\text{m}$) are present in the field of view for each waveguide. Fifteen different waveguides separated by a distance of $150 \mu\text{m}$ are present in the field of view. We have 1.387 pixel/ μm in the image and a magnification of 7.467 of the optical setup. The quality of the images is affected by stray light in the middle of the image as well as close to the mirror. The average intensity of each of the fifteen waveguides is degrading laterally with a maximum located in the center of the chip. This intensity distribution follows the gaussian intensity distribution coming from the laser beam used to inject light inside the chip. If we would have created a flat-top illumination, the average intensity of each waveguide would have been equalized.

After evaluation of the quality of the images, we concluded that only the eight waveguides located in the middle of the chip were usable. And that only approximately the first 64 nano-samplers which were not affected by the stray light could be used to reconstruct the spectrum. This will have a direct effect on the resolution of the extracted spectrum, see equation 3.15.

For the external cavity laser diode emitting at $\lambda = 789\text{nm}$, we extracted a complete interferogram including the data from the first 64 nano-sampler and 871 mirror steps of 20nm each from the waveguide showing the highest average intensity. Even with a reduced number of nano-samplers, the interferogram data results in 55744 sampling points. Fig. 3.20 show the raw interferogram. Each color represents another nano-sampler. According to equation 3.19, we need to remove some samples sets induced by the mirror shift to cover the OPD_{ns} an integer number of times. Therefore, we reduces the number of samples sets to $N_m = 787$ which

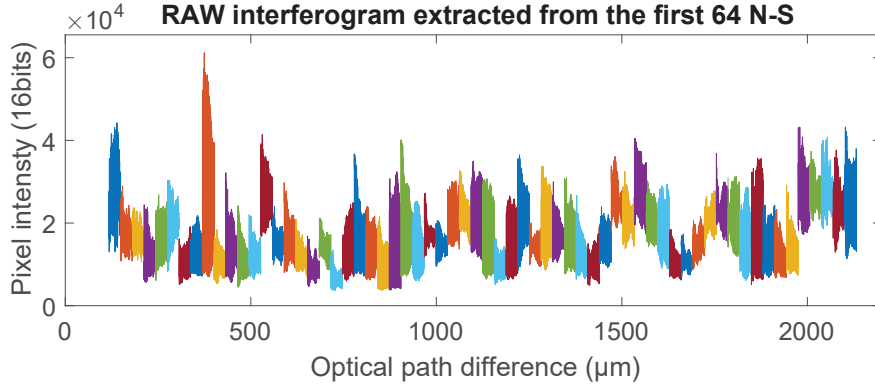


Figure 3.20 – Raw interferogram of the first 64 nano-samplers without any post-processing for 871 mirror steps of 20nm at $\lambda = 789\text{nm}$. Each different color represents another nano-sampler.

will correspond to OPD_{ns} .

In Fig. 3.21 we show the interferogram with 787 mirror steps plotted in 2 dimensions. During the recording of the interferogram, the data of Fig. 3.21 is acquired line by line. For every line, the mirror is shifted by 20nm. The OPD induced by an entire column is equal to the OPD between two adjacent nano-sampler.

The calibration procedure of the scanning SWIFTS should be done at different wavelengths in the used bandwidth. In the following section we will show a typical calibration procedure at $\lambda = 789\text{nm}$. As we know what should be the shape of the expected interferogram in the ideal case, we will apply different corrections to the interferogram to reshape it to its ideal form. As we will see, this calibration procedure is a preliminary approach and more work has to be done to take into account all the unwanted effects perturbing the interferogram.

3.4.3 Post-processing of the interferogram for calibration

3.4.3.1 Nano-sampler DC level calibration

In Fig. 3.22 we can see a zoom on the interferogram of the 5 first nano-samplers. The graph on the top shows the raw interferogram extracted from the images acquired with the camera. In the raw spectrum each nano-sampler has a different mean intensity. This is the DC error. The error mainly comes from the presence of a second standing wave which is created between the two facets of the waveguide. Due to the periodic positioning of the nano-samplers, at a certain wavelength, a phase-matching condition can be found for all the nano-samplers acting like a distributed Bragg grating. This will induce a wavelength dependent perturbation of the DC level of each nano-sampler.

To measure the DC level of each nano-sampler, we injected a monochromatic laser light

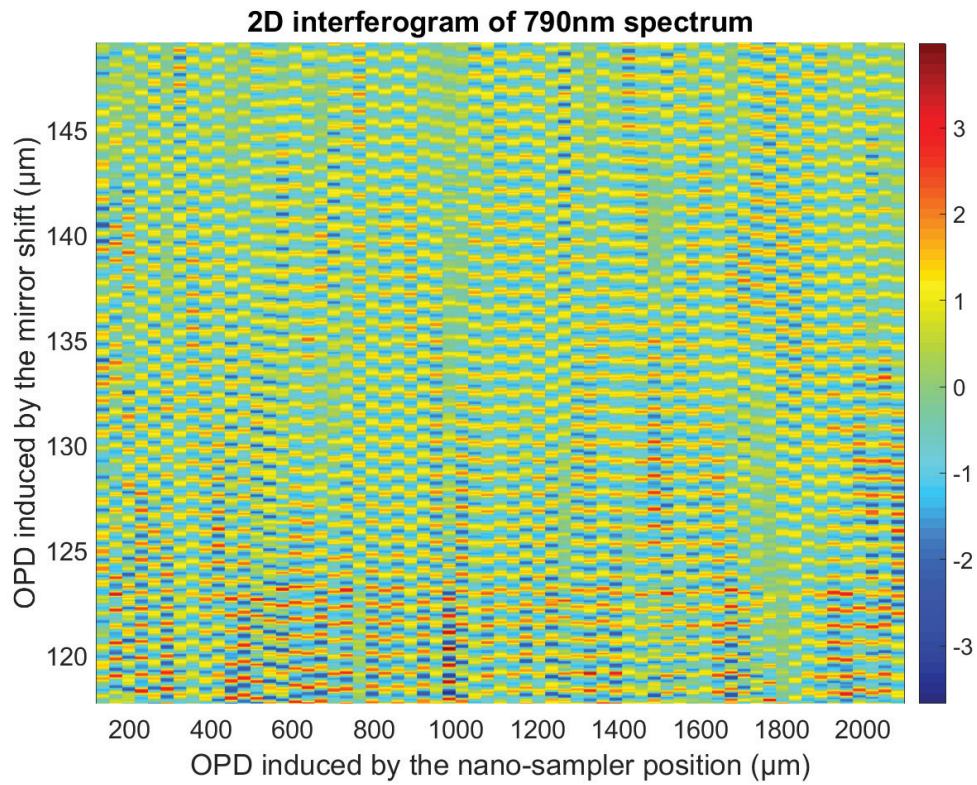


Figure 3.21 – Example of a complete interferogram showed in 2 dimension for 871 mirror steps of 20nm each at $\lambda = 789\text{nm}$. The x-axis represents the OPD induced by the first 64 nanosamplers. The y-axis represents the OPD induced by the mirror.

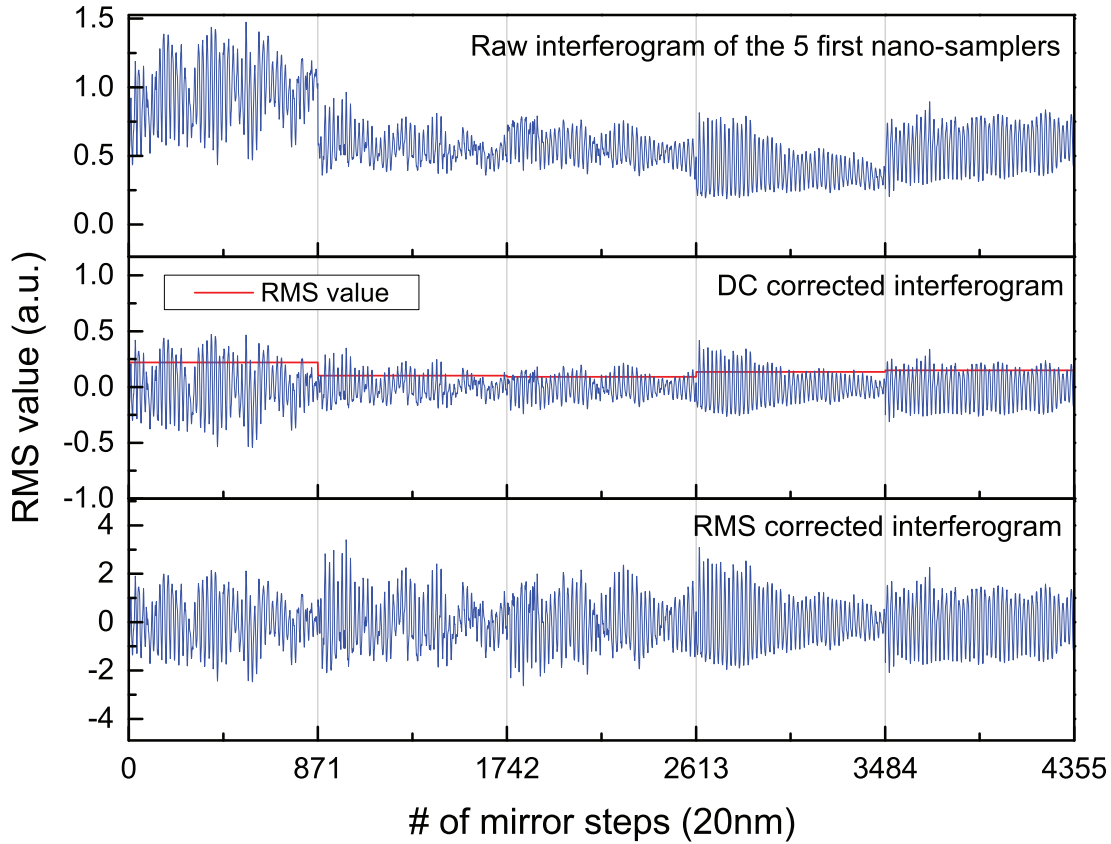


Figure 3.22 – Interferogram of the 5 first nano-samplers on a total of 64. On the top is the raw data. In the middle is the DC corrected data. On the bottom is the RMS corrected data.

source into the waveguides without the mirror at the end of the waveguides. In that case, only the standing wave induced by the Fabry-Pérot resonator is present. This DC level should be recorded at different wavelength to create a complete calibration data. In Fig. 3.22, the saved DC level of each nano-sampler is subtracted from the raw interferogram. The result can be seen on the graph of the middle of Fig. 3.22.

3.4.3.2 Nano-sampler scattering efficiency calibration

The scattering cross-section of each nano-sampler corresponds to its efficiency to scatter light out of the waveguide. For a sinusoid the scattering cross-section can be measured by its root mean square (RMS) level. On Fig. 3.22, on the graph of the middle, the red line corresponds to the RMS value of each nano-sampler. The graph on the bottom shows the interferogram divided by the RMS value of each nano-sampler. Now the interferogram looks way better than in the beginning. Nevertheless, if you look at the x-axis, it is still containing the 871 mirror steps for each nano-sampler which does not correspond to the OPD_{ns} between each nano-sampler.

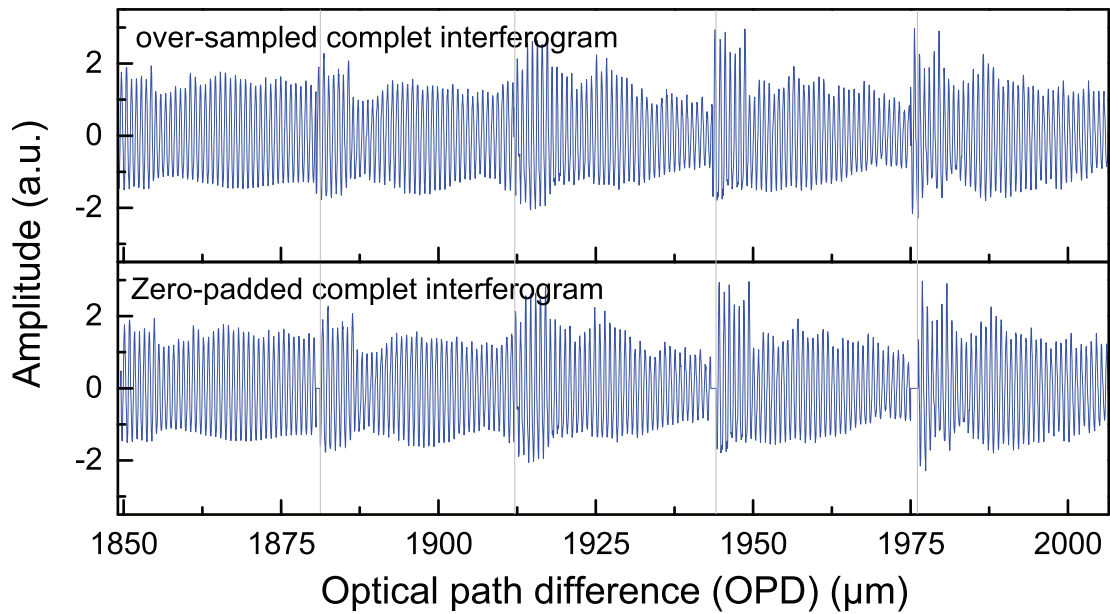


Figure 3.23 – Complete interferogram without overlapping OPD samples on the top. Phase matched interferogram by zero-padding on the bottom.

3.4.3.3 Correction of the nano-sampler position – Phase matching

With the mirror step size of 20nm used during our measurements, we can fulfill the requirement given by equation 3.19 by reducing the 871 samples recorded for each nano-sampler to 787. The interferogram with its right amount of sample is shown on the top of Fig. 3.23. Notice that we now show the data of some other nano-samplers which are not close to the mirror. In contrast with the 3 first nano-samplers of the waveguide, the following nano-samplers are not affected by stray light. The x-axis has now also been plotted in OPD, including the lost OPD from the mirror gap. In that case, the interferogram should be phase matched and no leakage should be seen in the spectrum. Nevertheless, as shown in Fig. 3.24 we see some replications of the spectrum appearing on the side of all major peaks. This leakage effect of the FFT can come from two other errors. Until now, we assumed that there were no positioning errors of mirror shift and of the nano-samplers position. But in case these errors exist, they will induce a leakage effect in the FFT. Therefore, we processed the interferogram to phase match all the individual spectra recorded by each nano-sampler assuming that no error is present in the mirror shift. This will compensated any error of nano-sampler positioning. Each spectrum obtained from individual nano-samplers is compared to each other by cross-correlation to determine their phase match. The individual spectra are then zero-padded in the direction of the minimal phase shift. After this calibration procedure, a zero-padded interferogram is reconstructed. The zero-padded interferogram is shown on the bottom graph in Fig. 3.23. The resulting spectrum found from the zero-padded interferogram is shown in Fig. 3.25. We can see that there are still some remaining peaks coming from FFT leakage. We think that those are probably coming from the non-linear mirror shift. The latter can be corrected

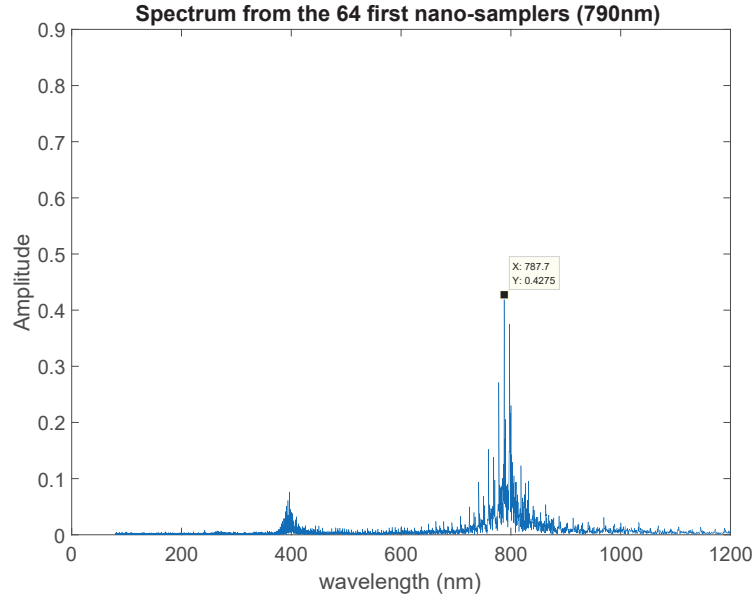


Figure 3.24 – Spectrum of the external cavity laser diode at $\lambda = 789\text{nm}$. The spectrum is obtained by Fourier transform of the non-zero padded interferogram.

be apply a shift in OPD of the samples of individual nano-sampler spectra. To do this, we need to interpolate the interferogram and then correct for the non-uniform mirror shift. This will lead to a non-uniform sampling of the interferogram. Therefore a Nonequispaced fast Fourier transform (NFFT) method should be used. In this work, we did not tried to process the interferogram with NFFT. Nevertheless we found that some free MATLAB packages are implementing these algorithms [166].

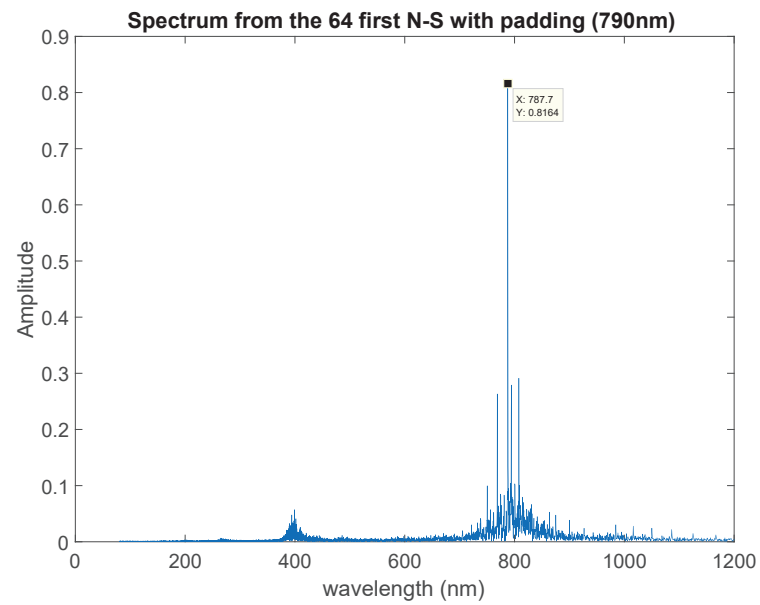


Figure 3.25 – Spectrum of the external cavity laser diode at $\lambda = 789\text{nm}$. The spectrum is obtained by Fourier transform of the zero padded interferogram. Less leakage can be seen.

3.5 Futur perspectives

The goal of miniaturizing a spectrometer thanks to the SWIFTS can be achieved. Of course it doesn't come without some trade-offs. As we have seen, the SWIFTS does have a very high resolution but a small bandwidth because of the under-sampling of the interferogram. With the implementation of the scanning mirror, we could increase the bandwidth of the spectrometer. But as we have shown, the implementation of a moving part creates like the scanning mirror introduces some errors which need to be corrected in some calibration step. Here we just did some preliminary calibrations which revealed the complexity of the problem. A specific calibration procedure needs to be found which can be applied to any fabricated spectrometer. The calibration data should be done at specific wavelengths and then be interpolated to work at any wavelength inside the used wavelength range. The quality of the results shown in this work was altered by the quality of the fabrication of the device and its optical readout setup. Many improvements can be done in reducing the stray light and reducing the minimal mirror gap which limits the bandwidth of the spectrometer. Other waveguide designs should be investigated in which the sampling frequency could be increased without the need of a moving mirror. This can be the case for mono mode slab waveguides on which phase shifted rows of nano-samplers could be patterned [167].

3.6 Conclusion

We showed the realisation of the first scanning Lippmann SWIFTS. This scanning SWIFTS concept is the building block of the realization of an imaging spectrometer having an extended bandwidth. Thanks to a scanning mirror, it is possible to stack the waveguides and the detectors in a 2D matrix which would form a miniature imaging spectrometer. This work was focused on the miniaturization and the fabrication of a scanning SWIFTS. The post-processing shown here has been only done to have a minimal feedback on the effects of fabrication errors and general design mistakes.

We presented the model of an ideal Lippmann SWIFTS. This model predicts the baseline of a Lippmann SWIFTS spectrometer. Moreover it showed that an ideal scattering efficiency of the nano-sampler exists if we want to maximize the contrast of the measured interferogram. The spectrometer has been designed to work for a 25nm bandwidth centered at 762.5nm with a spectral resolution of 0.12nm. All of the components like the micro-lenses, the waveguides and the optics were optimized for these wavelengths.

For the realization of the spectrometer demonstrator, we used an optical system and a camera to read out the scattered information from the sampled interferogram. The SWIFTS chips consist of single-mode waveguides which were made out of transparent epoxy based negative photoresist called EpoCore. The fabrication process of epoxy based EpoCore waveguides showed the feasibility of reasonably large single mode waveguides with very low losses in a simple and cheap process. We also demonstrated the successful realisation of a mix & match e-beam lithography based on EpoCore material. We also showed the first parallel measurement of six adjacent waveguides on the same chip.

The fabrication of the SWIFTS chip and the errors due to the mirror movement have been cancelled by specific calibration steps. The individual DC level of each nano-sampler has been corrected. The scattering efficiency of each nano-sampler has been corrected by measuring its RMS value. In addition, the nano-sampler position error has been corrected by a phase matching algorithm which introduced some zero-padding in the interferogram. Finally, we have shown the spectrum of two monochromatic light sources which could be measured with the scanning SWIFTS.

4 Conclusion

We have studied two new optical sensing approaches based on the interaction of light with metallic nano-structures. These new applications have emerged thanks to the technological advances in nano-scale manufacturing mainly based on electron beam lithography. The ability to fabricate three dimensional metallic nano-structures with a total freedom of design in two dimensions with a resolution down to 10 nanometers are enabling the access to the sub-wavelength play ground for visible light. For both studied sensing approaches we have shown the importance of the integrated waveguide excitation which confines the light and limits its interaction with the nano-structure in space.

The chapter two of this thesis focused on the application of metallic nano-structures exhibiting a characteristic plasmonic resonance as well as some plasmonic waveguiding. These were used to detect the local change of refractive index in femto-liter volumes. We have demonstrated the successful excitation of these plasmonic slot waveguide cavities (PSWC) with the use of a super-continuum light source injected into integrated single-mode silicon strip waveguides. We are persuaded that this bio-sensor is a promising candidate for single molecule sensing at high concentrations. This work paved the way to the study of any kind of plasmonic resonating structure.

The chapter three also dealt with metallic nano-structures. In contrast with the nano-structures used in the chapter two, these metallic nano-structures were not exhibiting a plasmonic response. They were used to perturb the light travelling in a waveguide. Their extremely small size enabled the local probing of the light intensity present in the waveguide. These nano-structures were used to retrieve the intensity of a standing wave generated inside a single-mode waveguide. The information given by the intensity of the standing wave along the waveguide extracted by a multitude of these nano-structures carries the information of the spectrum of the guided light. This sensor is typically called a spectrometer. We developed a Lippmann Standing wave integrated Fourier spectrometer (SWIFTS) whose bandwidth has been enlarged thanks to a moving mirror which was inducing an additional phase change in the interferogram. Here we demonstrated the ability of metallic nano-structures to be the building blocks of sub-wavelength probing.

Chapter 4. Conclusion

Both research projects used the special properties of nano-scale metallic structures to locally interact with light. In both cases, the integration of the excitation showed a strong potential to reduce the size of optical sensors in specific domains of sensing. A more detailed conclusion on the work done in each chapter can be found on page 78 for chapter two and on page 113 for chapter three. Finally, we would say that there is room for a lot of exciting work involving metallic nano-structures in the domain of optics.

A Appendix

A.1 Fabrication recipes

A.1.1 PECVD SiO₂ deposition

The SiO₂ layers are deposited with the PlasmaLab 80+ from Oxford Instrument. The basic recipe which is giving a low stress layer of SiO₂ with a refractive index of 1.45 at $\lambda = 1500\text{nm}$ is given in table A.1.

Process parameter	Parameter value
Pressure	1000mT
RF power	20W @ 13.56MHz
Platen temperature	300°C
SiH ₄ flow	8sccm
N ₂ O flow	710sccm
N ₂ flow	162sccm
Deposition rate	63.6nm/s

Table A.1 – PECVD SiO₂ depositon process parameters

A.1.2 Waveguide dry etching

The waveguides are etched on a STS Multiplex ICP etcher. A "pseudo Bosch process" has been developed to etch the silicon with smooth sidewalls. The complet etching of the waveguides is done in three different consecutive etches. The first etch step is a resist descum to remove the resist residues left on the surface after development. The oxygen plasma descum step is always done after the development of any ZEP520A film. The second etch step is used to etch the 50nm of SiO₂. The third etch step is used to etch the silicon. The process parameters used to remove the resist residues are shown in table A.2. The process parameters used to etch the SiO₂ layer are shown in table A.3. The process parameters used to etch the silicon with the pseudo Bosch process are shown in table A.4.

Process parameter	Parameter value
Pressure	10mT
ICP RF power	0W
Platen RF power	50W
Platen temperature	20°C
O ₂ flow	20sccm
Process time	25sec

Table A.2 – O₂ plasma descum recipe to clean resist residues after development of the ZEP520A

Process parameter	Parameter value
Pressure	3mT
ICP RF power	600W
Platen RF power	200W
Platen temperature	20°C
O ₂ flow	2sccm
C ₃ F ₈ flow	30sccm

Table A.3 – SiO₂ etch process parameters on STS Multiplex ICP etcher

Process parameter	Parameter value
Pressure	10mT
ICP RF power	800W
Platen RF power	15W
Platen temperature	20°C
SF ₆ flow	6sccm
C ₃ F ₈ flow	20sccm

Table A.4 – Pseudo Bosch process parameters on STS Multiplex ICP etcher

A.1.3 EpoCore and EpoClad photolithography parameters

The single-mode waveguides for the SWIFTS device are fabricated with the EpoCore material as waveguide core and EpoClad as waveguide cladding. The EpoClad and EpoCore materials can be bought in mixture having different viscosities to achieve different thickness ranges. In our case, we used EpoClad_5 (for $\sim 5\mu\text{m}$) and EpoCore_2 (for $\sim 2\mu\text{m}$). The Fabrication is a three step process:

1. The deposition and polymerization (flood exposure) of a $5\mu\text{m}$ thick layer of EpoClad_5
2. The deposition of a $2\mu\text{m}$ thick layer of EpoCore_2
3. The exposure through a lithography mask of the layer to define the waveguide.

In table A.5 we give the parameters we used to realize these waveguides. A dose test has been made to define the exact dose needed to have the desired waveguide. This dose has been found to be $175 \text{ mJ}/\text{cm}^2$.

A.1. Fabrication recipes

Photoresist type :

EpoClad_5 EpoCore_2

Description	Units	Values	
Layer thickness	(μm)	5	2
Substrate preparation		For Si and SiO ₂ : 30min at 200°C in the oven; for FR-4 (epoxy): O ₂ plasma; for crosslinked EpoClad: O ₂ plasma	
Spincoating	(tr/min)	3000	3000
	(s)	30	30
Relaxation	(min)	-	-
Prebake on hotplate	(°C)	120	50/90
	(min)	5	2/2
Relaxation	(min)	-	-
Exposition (dose meas. @ 365nm)	(mJ/cm ²)	350 +/- 50	150 - 200
Post exposure bake (PEB) on hotplate. Let it cool down slowly one hotplate	(°C)	120	50/85
Relaxation	(min)	-	30
Developement in Mr-Dev 600	(sec)	90 +/- 20	45 +/- 10
Hardbake on hotplate	(°C)	120-140	120-140
	(min)	30-60	30

Table A.5 – Recipe given by Microresist Technology for layer of EpoClad_5 and EpoCore_2.

Bibliography

- [1] Qing Tan, Armando Cosentino, Matthieu Roussey, and Hans Peter Herzig. Theoretical and experimental study of a 30nm metallic slot array. *Journal of the Optical Society of America B*, 28(7):1711–1715, July 2011.
- [2] D. E. Aspnes and J. B. Theeten. Spectroscopic Analysis of the Interface Between Si and Its Thermally Grown Oxide. *Journal of The Electrochemical Society*, 127(6):1359–1365, June 1980.
- [3] Peter B. Johnson and R.-W_ Christy. Optical constants of the noble metals. *Physical Review B*, 6(12):4370, 1972.
- [4] Edward D Palik. *Handbook of optical constants of solids*. Academic Press, Orlando, 1985.
- [5] Robert Hull. *Properties of Crystalline Silicon*. IET, 1999.
- [6] Gaël David Osowiecki, Elsie Barakat, Ali Naqavi, and Hans Peter Herzig. Vertically coupled plasmonic slot waveguide cavity for localized biosensing applications. *Optics Express*, 22(17):20871, 2014.
- [7] David Bohm and David Pines. A Collective Description of Electron Interactions. I. Magnetic Interactions. *Physical Review*, 82(5):625–634, June 1951.
- [8] David Pines and David Bohm. A Collective Description of Electron Interactions: II. Collective vs Individual Particle Aspects of the Interactions. *Physical Review*, 85(2):338–353, January 1952.
- [9] David Bohm and David Pines. A Collective Description of Electron Interactions: III. Coulomb Interactions in a Degenerate Electron Gas. *Physical Review*, 92(3):609–625, November 1953.
- [10] A. Sommerfeld. Über die Ausbreitung der Wellen in der drahtlosen Telegraphie. *Annalen der Physik*, 333(4):665–736, January 1909.
- [11] R. H. Ritchie. Plasma Losses by Fast Electrons in Thin Films. *Physical Review*, 106(5):874–881, June 1957.

Bibliography

- [12] R. H. Ritchie and H. B. Eldridge. Optical Emission from Irradiated Foils. I. *Physical Review*, 126(6):1935–1947, June 1962.
- [13] Heinz Raether. *Surface plasmons on smooth and rough surfaces and on gratings*. Springer, 1988.
- [14] H. Raether. Surface plasma oscillations as a tool for surface examinations. *Surface Science*, 8(1):233–246, July 1967.
- [15] R. H. Ritchie, E. T. Arakawa, J. J. Cowan, and R. N. Hamm. Surface-Plasmon Resonance Effect in Grating Diffraction. *Physical Review Letters*, 21(22):1530–1533, November 1968.
- [16] Andreas Otto. Excitation of nonradiative surface plasma waves in silver by the method of frustrated total reflection. *Zeitschrift für Physik*, 216(4):398–410, August 1968.
- [17] Erwin Kretschmann. Die Bestimmung optischer Konstanten von Metallen durch Anregung von Oberflächenplasmaschwingungen. *Zeitschrift für Physik A Hadrons and Nuclei*, 241(4):313–324, 1971.
- [18] Xudong Fan, Ian M. White, Siyka I. Shopova, Hongying Zhu, Jonathan D. Suter, and Yuze Sun. Sensitive optical biosensors for unlabeled targets: A review. *Analytica Chimica Acta*, 620(1–2):8–26, July 2008.
- [19] Marazuela and Moreno-Bondi. Fiber-optic biosensors - an overview. *Analytical and Bioanalytical Chemistry*, 372(5–6):664–682, March 2002.
- [20] Matthew A. Cooper. Optical biosensors: where next and how soon? *Drug Discovery Today*, 11(23–24):1061–1067, December 2006.
- [21] John Comley. LABEL-FREE DETECTION New biosensors facilitate broader range of drug discovery applications. *Drug Discovery World*, 2004.
- [22] Owen P. Hamill, A. Marty, Erwin Neher, Bert Sakmann, and F. J. Sigworth. Improved patch-clamp techniques for high-resolution current recording from cells and cell-free membrane patches. *Pflügers Archiv*, 391(2):85–100, 1981.
- [23] G. Binnig, H. Rohrer, Ch. Gerber, and E. Weibel. Surface Studies by Scanning Tunneling Microscopy. *Physical Review Letters*, 49(1):57–61, July 1982.
- [24] Shuming. Nie, Daniel T. Chiu, and Richard N. Zare. Real-Time Detection of Single Molecules in Solution by Confocal Fluorescence Microscopy. *Analytical Chemistry*, 67(17):2849–2857, September 1995.
- [25] Thomas A. Klar, Stefan Jakobs, Marcus Dyba, Alexander Egner, and Stefan W. Hell. Fluorescence microscopy with diffraction resolution barrier broken by stimulated emission. *Proceedings of the National Academy of Sciences*, 97(15):8206–8210, July 2000.

-
- [26] Robert M. Dickson, Andrew B. Cubitt, Roger Y. Tsien, and W. E. Moerner. On/off blinking and switching behaviour of single molecules of green fluorescent protein. *Nature*, 388(6640):355–358, July 1997.
- [27] Eric Betzig, George H. Patterson, Rachid Sougrat, O. Wolf Lindwasser, Scott Olenych, Juan S. Bonifacino, Michael W. Davidson, Jennifer Lippincott-Schwartz, and Harald F. Hess. Imaging Intracellular Fluorescent Proteins at Nanometer Resolution. *Science*, 313(5793):1642–1645, September 2006.
- [28] F. Vollmer and S. Arnold. Whispering-gallery-mode biosensing: label-free detection down to single molecules. *Nature methods*, 5(7):591–596, 2008.
- [29] A. M. Armani, R. P. Kulkarni, S. E. Fraser, R. C. Flagan, and K. J. Vahala. Label-Free, Single-Molecule Detection with Optical Microcavities. *Science*, 317(5839):783–787, August 2007.
- [30] Philip Tinnefeld. Single-molecule detection: Breaking the concentration barrier. *Nature Nanotechnology*, 8(7):480–482, July 2013.
- [31] Phil Holzmeister, Guillermo P. Acuna, Dina Grohmann, and Philip Tinnefeld. Breaking the concentration limit of optical single-molecule detection. *Chemical Society Reviews*, 43(4):1014–1028, September 2013.
- [32] Peter Zijlstra, Pedro M. R. Paulo, and Michel Orrit. Optical detection of single non-absorbing molecules using the surface plasmon resonance of a gold nanorod. *Nature Nanotechnology*, 7:379–382, April 2012.
- [33] A. Messica, A. Greenstein, and A. Katzir. Theory of fiber-optic, evanescent-wave spectroscopy and sensors. *Applied Optics*, 35(13):2274–2284, 1996.
- [34] V. Ruddy, B. D. MacCraith, and J. A. Murphy. Evanescent wave absorption spectroscopy using multimode fibers. *Journal of Applied Physics*, 67(10):6070–6074, May 1990.
- [35] N. J. Harrick. *Internal reflection spectroscopy*. Interscience Publishers, 1967.
- [36] S. Zhu. Frustrated total internal reflection: A demonstration and review. *American Journal of Physics*, 54(7):601, 1986.
- [37] Yu-Chi Chang, Philip Wägli, Vincent Paeder, Alexandra Homsy, Lubos Hvozدارa, Peter van der Wal, Joab Di Francesco, Nico F. de Rooij, and Hans Peter Herzig. Cocaine detection by a mid-infrared waveguide integrated with a microfluidic chip. *Lab on a Chip*, 12(17):3020–3023, July 2012.
- [38] A. Densmore, D.-X. Xu, S. Janz, P. Waldron, T. Mischki, G. Lopinski, A. Delage, J. Lapointe, P. Cheben, B. Lamontagne, and J. H. Schmid. Spiral-path high-sensitivity silicon photonic wire molecular sensor with temperature-independent response. *Optics Letters*, 33(6):596–598, March 2008.

Bibliography

- [39] A. Densmore, D. X Xu, P. Waldron, S. Janz, P. Cheben, J. Lapointe, A. Delage, B. Lamontagne, J. H Schmid, and E. Post. A Silicon-on-Insulator Photonic Wire Based Evanescent Field Sensor. *IEEE Photonics Technology Letters*, 18(23):2520–2522, December 2006.
- [40] Aurel Ymeti, Jan Greve, Paul V. Lambeck, Thijs Wink, van Hövell, Beumer, Robert R. Wijn, Rene G. Heideman, Vinod Subramaniam, and Johannes S. Kanger. Fast, Ultrasensitive Virus Detection Using a Young Interferometer Sensor. *Nano Lett.*, 7(2):394–397, 2006.
- [41] Nile F. Hartman. Integrated optic interferometric sensor, April 1997.
- [42] D. Hofstetter, H.P. Zappe, and R. Dandliker. A monolithically integrated double Michelson interferometer for optical displacement measurement with direction determination. *IEEE Photonics Technology Letters*, 8(10):1370–1372, October 1996.
- [43] F Prieto, B Sep lveda, A Calle, A Llobera, C Dom nguez, A Abad, A Montoya, and L M Lechuga. An integrated optical interferometric nanodevice based on silicon technology for biosensor applications. *Nanotechnology*, 14(8):907–912, August 2003.
- [44] B.E. Little, S.T. Chu, H.A. Haus, J. Foresi, and J.-P. Laine. Microring resonator channel dropping filters. *Journal of Lightwave Technology*, 15(6):998–1005, June 1997.
- [45] Katrien De Vos, Irene Bartolozzi, Etienne Schacht, Peter Bienstman, and Roel Baets. Silicon-on-Insulator microring resonator forsensitive and label-free biosensing. *Optics Express*, 15(12):7610–7615, June 2007.
- [46] A. Ramachandran, S. Wang, J. Clarke, S.J. Ja, D. Goad, L. Wald, E.M. Flood, E. Knobbe, J.V. Hryniewicz, S.T. Chu, D. Gill, W. Chen, O. King, and B.E. Little. A universal biosensing platform based on optical micro-ring resonators. *Biosensors and Bioelectronics*, 23(7):939–944, February 2008.
- [47] D. X. Xu, A. Densmore, A. Delâge, P. Waldron, R. McKinnon, S. Janz, J. Lapointe, G. Lopinski, T. Mischki, E. Post, P. Cheben, and J. H. Schmid. Folded cavity SOI microring sensors for highsensitivity and real time measurement ofbiomolecular binding. *Optics Express*, 16(19):15137–15148, 2008.
- [48] Xudong Fan, Ian M. White, Hongying Zhu, Jonanthan D. Suter, and Hesam Oveys. Overview of novel integrated optical ring resonator bio/chemical sensors. volume 6452, pages 64520M–64520M–20, 2007.
- [49] Jiri Homola, Sinclair S. Yee, and Günter Gauglitz. Surface plasmon resonance sensors: review. *Sensors and Actuators B: Chemical*, 54(1-2):3–15, January 1999.
- [50] Jiri Homola and Jakub Dostálek. *Surface plasmon resonance based sensors*, volume 4. Springer, 2006.
- [51] Jiří Homola. Present and future of surface plasmon resonance biosensors. *Analytical and Bioanalytical Chemistry*, 377(3):528–539, October 2003.

-
- [52] R.D. Harris and J.S. Wilkinson. Waveguide surface plasmon resonance sensors. *Sensors and Actuators B: Chemical*, 29(1–3):261–267, October 1995.
- [53] Jiri Homola. Surface Plasmon Resonance Sensors for Detection of Chemical and Biological Species. *Chem. Rev.*, 108(2):462–493, 2008.
- [54] William L. Barnes, Alain Dereux, and Thomas W. Ebbesen. Surface plasmon subwavelength optics. *Nature*, 424(6950):824–830, August 2003.
- [55] Jon A. Schuller, Edward S. Barnard, Wenshan Cai, Young Chul Jun, Justin S. White, and Mark L. Brongersma. Plasmonics for extreme light concentration and manipulation. *Nature Materials*, 9(3):193–204, March 2010.
- [56] J. C. Tsang, J. R. Kirtley, and J. A. Bradley. Surface-Enhanced Raman Spectroscopy and Surface Plasmons. *Physical Review Letters*, 43(11):772–775, September 1979.
- [57] Uwe Kreibig and Peter Zacharias. Surface plasma resonances in small spherical silver and gold particles. *Zeitschrift für Physik*, 231(2):128–143, 1970.
- [58] Yong Chen and Hai Ming. Review of surface plasmon resonance and localized surface plasmon resonance sensor. *Photonic Sensors*, 2(1):37–49, March 2012.
- [59] Katherine A. Willets and Richard P. Van Duyne. Localized surface plasmon resonance spectroscopy and sensing. *Annu. Rev. Phys. Chem.*, 58:267–297, 2007.
- [60] Kathryn M. Mayer and Jason H. Hafner. Localized Surface Plasmon Resonance Sensors. *Chemical Reviews*, 111(6):3828–3857, June 2011.
- [61] Amanda J. Haes and Richard P. Van Duyne. A unified view of propagating and localized surface plasmon resonance biosensors. *Analytical and Bioanalytical Chemistry*, 379(7–8):920–930, August 2004.
- [62] Stefan Mühlig, Alastair Cunningham, José Dintinger, Mohamed Farhat, Shakeeb Bin Hasan, Toralf Scharf, Thomas Bürgi, Falk Lederer, and Carsten Rockstuhl. A self-assembled three-dimensional cloak in the visible. *Scientific Reports*, 3, August 2013.
- [63] Terukazu Kosako, Yutaka Kadoya, and Holger F. Hofmann. Directional control of light by a nano-optical Yagi–Uda antenna. *Nature Photonics*, 4(5):312–315, May 2010.
- [64] Boris Luk'yanchuk, Nikolay I. Zheludev, Stefan A. Maier, Naomi J. Halas, Peter Nordlander, Harald Giessen, and Chong Tow Chong. The Fano resonance in plasmonic nanostructures and metamaterials. *Nature Materials*, 9(9):707–715, September 2010.
- [65] Holger Fischer and Olivier J. F. Martin. Engineering the optical response of plasmonic nanoantennas. *Optics Express*, 16(12):9144–9154, June 2008.
- [66] Jeffrey N. Anker, W. Paige Hall, Olga Lyandres, Nilam C. Shah, Jing Zhao, and Richard P. Van Duyne. Biosensing with plasmonic nanosensors. *Nature Materials*, 7(6):442–453, 2008.

Bibliography

- [67] E. N. Economou. Surface Plasmons in Thin Films. *Physical Review*, 182(2):539–554, June 1969.
- [68] Z. Han, A. Y. Elezzabi, and V. Van. Experimental realization of subwavelength plasmonic slot waveguides on a silicon platform. *Optics Letters*, 35(4):502–504, February 2010.
- [69] Hyuck Choo, Myung-Ki Kim, Matteo Staffaroni, Tae Joon Seok, Jeffrey Bokor, Stefano Cabrini, P. James Schuck, Ming C. Wu, and Eli Yablonovitch. Nanofocusing in a metal-insulator-metal gap plasmon waveguide with a three-dimensional linear taper. *Nature Photonics*, 6(12):838–844, December 2012.
- [70] J. A. Dionne, L. A. Sweatlock, H. A. Atwater, and A. Polman. Plasmon slot waveguides: Towards chip-scale propagation with subwavelength-scale localization. *Physical Review B*, 73(3):035407, January 2006.
- [71] Ruoxi Yang and Zhaolin Lu. Subwavelength Plasmonic Waveguides and Plasmonic Materials. *International Journal of Optics*, 2012:1–12, 2012.
- [72] G. Veronis and Shanhui Fan. Modes of Subwavelength Plasmonic Slot Waveguides. *Journal of Lightwave Technology*, 25(9):2511–2521, September 2007.
- [73] Georgios Veronis and Shanhui Fan. Guided subwavelength plasmonic mode supported by a slot in a thin metal film. *Optics Letters*, 30(24):3359–3361, December 2005.
- [74] Cécile Delacour, Sylvain Blaize, Philippe Grosse, Jean Marc Fedeli, Aurélien Bruyant, Rafael Salas-Montiel, Gilles Lerondel, and Alexei Chelnokov. Efficient Directional Coupling between Silicon and Copper Plasmonic Nanoslot Waveguides: toward Metal-Oxide-Silicon Nanophotonics. *Nano Letters*, 10(8):2922–2926, August 2010.
- [75] Surbhi Lal, Stephan Link, and Naomi J. Halas. Nano-optics from sensing to waveguiding. *Nature Photonics*, 1(11):641–648, November 2007.
- [76] Felipe Bernal Arango, Andrej Kwadrin, and A. Femius Koenderink. Plasmonic Antennas Hybridized with Dielectric Waveguides. *ACS Nano*, 6(11):10156–10167, November 2012.
- [77] Armando Cosentino, Qing Tan, Matthieu Roussey, and Hans Peter Herzig. Refractive index sensor based on slot waveguide cavity. *J. Europ. Opt. Soc. Rap. Public.*, 7:12039, 2012.
- [78] J. Yang, C. Sauvan, A. Jouanin, S. Collin, J.-L. Pelouard, and P. Lalanne. Ultrasmall metal-insulator-metal nanoresonators: impact of slow-wave effects on the quality factor. *Optics Express*, 20(15):16880–16891, July 2012.
- [79] D. F. P. Pile, T. Ogawa, D. K. Gramotnev, Y. Matsuzaki, K. C. Vernon, K. Yamaguchi, T. Okamoto, M. Haraguchi, and M. Fukui. Two-dimensionally localized modes of a nanoscale gap plasmon waveguide. *Applied Physics Letters*, 87(26):261114–261114–3, December 2005.

-
- [80] J. A. Dionne, L. A. Sweatlock, M. T. Sheldon, A. P. Alivisatos, and H. A. Atwater. Silicon-Based Plasmonics for On-Chip Photonics. *IEEE Journal of Selected Topics in Quantum Electronics*, 16(1):295–306, January 2010.
- [81] Volker J. Sorger, Rupert F. Oulton, Ren-Min Ma, and Xiang Zhang. Toward integrated plasmonic circuits. *MRS Bulletin*, 37(08):728–738, August 2012.
- [82] Roman Bruck and Otto L. Muskens. Plasmonic nanoantennas as integrated coherent perfect absorbers on SOI waveguides for modulators and all-optical switches. *Optics Express*, 21(23):27652, November 2013.
- [83] Frédéric Peyskens, Ananth Z. Subramanian, Pieter Neutens, Ashim Dhakal, Pol Van Dorpe, Nicolas Le Thomas, and Roel Baets. Bright and dark plasmon resonances of nanoplasmonic antennas evanescently coupled with a silicon nitride waveguide. *Optics Express*, 23(3):3088, February 2015.
- [84] M. Castro-Lopez, N. de Sousa, A. Garcia-Martin, F. Y. Gardes, and R. Sapienza. Scattering of a plasmonic nanoantenna embedded in a silicon waveguide. *Optics Express*, 23(22):28108, November 2015.
- [85] Armando Cosentino. *Slot waveguide cavity: from fabrication to characterization and sensing applications*. PhD thesis, EPFL, Lausanne, 2013.
- [86] Qing Tan. *Subwavelength Metallic Structures for Sensing*. PhD thesis, EPFL, Lausanne, 2012.
- [87] T. W. Ebbesen, H. J. Lezec, H. F. Ghaemi, T. Thio, and P. A. Wolff. Extraordinary optical transmission through sub-wavelength hole arrays. *Nature*, 391(6668):667–669, February 1998.
- [88] C. Genet and T. W. Ebbesen. Light in tiny holes. *Nature*, 445(7123):39–46, January 2007.
- [89] Davy Gérard, Jérôme Wenger, Nicolas Bonod, Evgeni Popov, Hervé Rigneault, Farhad Mahdavi, Steve Blair, José Dintinger, and Thomas W. Ebbesen. Nanoaperture-enhanced fluorescence: Towards higher detection rates with plasmonic metals. *Physical Review B*, 77(4):045413, January 2008.
- [90] CST Microwave Studio.
- [91] T. Weiland. A discretization model for the solution of Maxwell’s equations for six-component fields. *Archiv Elektronik und Uebertragungstechnik*, 31:116–120, March 1977.
- [92] T. Weiland. Time Domain Electromagnetic Field Computation with Finite Difference Methods. *International Journal of Numerical Modelling: Electronic Networks, Devices and Fields*, 9(4):295–319, July 1996.

Bibliography

- [93] Kane S. Yee and others. Numerical solution of initial boundary value problems involving Maxwell's equations in isotropic media. *IEEE Trans. Antennas Propag*, 14(3):302–307, 1966.
- [94] Bernd Krietenstein, Rolf Schuhmann, Peter Thoma, Thomas Weiland, and others. The perfect boundary approximation technique facing the big challenge of high precision field computation. In *Proceedings of the XIX International Linear Accelerator Conference (LINAC 98), Chicago, USA*, pages 860–862, 1998.
- [95] Frank Wanlass and C. Sah. Nanowatt logic using field-effect metal-oxide semiconductor triodes. In *Solid-State Circuits Conference. Digest of Technical Papers. 1963 IEEE International*, volume 6, pages 32–33. IEEE, 1963.
- [96] Frank M. Wanlass. *Low stand-by power complementary field effect circuitry*. Google Patents, December 1967. US Patent 3,356,858.
- [97] James G. Goodberlet, J. Todd Hastings, and Henry I. Smith. Performance of the Raith 150 electron-beam lithography system. *Journal of Vacuum Science & Technology B*, 19(6):2499–2503, November 2001.
- [98] Mihir Parikh. Corrections to proximity effects in electron beam lithography. I. Theory. *Journal of Applied Physics*, 50(6):4371–4377, June 1979.
- [99] James D. Plummer. *Silicon VLSI Technology: Fundamentals, Practice, and Modeling*. Pearson Education, 2009.
- [100] H. Jansen, M. de Boer, and M. Elwenspoek. The black silicon method. VI. High aspect ratio trench etching for MEMS applications. In *IEEE, The Ninth Annual International Workshop on Micro Electro Mechanical Systems, 1996, MEMS '96, Proceedings. An Investigation of Micro Structures, Sensors, Actuators, Machines and Systems*, pages 250–257, February 1996.
- [101] Jy K. Bhardwaj and Huma Ashraf. Advanced silicon etching using high-density plasmas. volume 2639, pages 224–233, 1995.
- [102] K. Solehmainen, T. Aalto, J. Dekker, M. Kapulainen, M. Harjanne, Kaupo Kukli, P. Heimala, K. Kolari, and M. Leskela. Dry-etched silicon-on-insulator waveguides with low propagation and fiber-coupling losses. *Journal of Lightwave Technology*, 23(11):3875–3880, November 2005.
- [103] J. Bhardwaj, H. Ashraf, and A. McQuarrie. Dry silicon etching for MEMS. In *Proc. Symp. Microstructures and Microfabricated Systems, ECS*, 1997.
- [104] C.C. Welch, A.L. Goodyear, T. Wahlbrink, M.C. Lemme, and T. Mollenhauer. Silicon etch process options for micro- and nanotechnology using inductively coupled plasmas. *Microelectronic Engineering*, 83(4–9):1170–1173, April 2006.

-
- [105] Laurent Vivien and Lorenzo Pavesi. *Handbook of Silicon Photonics*. Taylor & Francis, April 2016.
- [106] Matthew Borselli, Thomas J. Johnson, and Oskar Painter. Beyond the Rayleigh scattering limit in high-Q silicon microdisks: theory and experiment. *Optics Express*, 13(5):1515, 2005.
- [107] M. C. M. Lee and Ming C. Wu. Thermal annealing in hydrogen for 3-D profile transformation on silicon-on-insulator and sidewall roughness reduction. *Journal of Microelectromechanical Systems*, 15(2), April 2006.
- [108] Lukas Chrostowski and Michael Hochberg. *Silicon Photonics Design*.
- [109] Koji Yamada. Silicon Photonic Wire Waveguides: Fundamentals and Applications. In David J. Lockwood and Lorenzo Pavesi, editors, *Silicon Photonic Wire Waveguides: Fundamentals and Applications*, number 119 in Topics in Applied Physics, pages 1–29. Springer Berlin Heidelberg, 2011. DOI: 10.1007/978-3-642-10506-7_1.
- [110] Michel Bruel, Bernard Aspar, and Andre-Jacques Auberton-Hervé. Smart-Cut: A New Silicon On Insulator Material Technology Based on Hydrogen Implantation and Wafer Bonding^{*1}. *Japanese Journal of Applied Physics*, 36(Part 1, No. 3B):1636–1641, March 1997.
- [111] Graham T. Reed and Andrew P. Knights. *Silicon Photonics: An Introduction*. John Wiley & Sons, October 2004.
- [112] G. Roelkens, D. Vermeulen, D. Van Thourhout, R. Baets, S. Brision, P. Lyan, P. Gautier, and J.-M. Fédéli. High efficiency diffractive grating couplers for interfacing a single mode optical fiber with a nanophotonic silicon-on-insulator waveguide circuit. *Applied Physics Letters*, 92:131101, 2008.
- [113] D. Taillaert, W. Bogaerts, P. Bienstman, T.F. Krauss, P. Van Daele, I. Moerman, S. Verstuyft, K. De Mesel, and R. Baets. An out-of-plane grating coupler for efficient butt-coupling between compact planar waveguides and single-mode fibers. *Quantum Electronics, IEEE Journal of*, 38(7):949–955, July 2002.
- [114] S. Monneret, P. Huguet-Chantôme, and F. Flory. m-lines technique: prism coupling measurement and discussion of accuracy for homogeneous waveguides. *Journal of Optics A: Pure and Applied Optics*, 2(3):188, 2000.
- [115] Jean-Pierre Berenger. A perfectly matched layer for the absorption of electromagnetic waves. *Journal of Computational Physics*, 114(2):185–200, October 1994.
- [116] E. a. J. Marcatili and S. E. Miller. Improved Relations Describing Directional Control in Electromagnetic Wave Guidance. *Bell System Technical Journal*, 48(7):2161–2188, September 1969.

Bibliography

- [117] M. Heiblum and J. Harris. Analysis of curved optical waveguides by conformal transformation. *IEEE Journal of Quantum Electronics*, 11(2):75–83, February 1975.
- [118] P. Bienstman, E. Six, A. Roelens, M. Vanwolleghem, and R. Baets. Calculation of bending losses in dielectric waveguides using eigenmode expansion and perfectly matched layers. *IEEE Photonics Technology Letters*, 14(2):164–166, February 2002.
- [119] Pierre Berini. Plasmon-polariton waves guided by thin lossy metal films of finite width: Bound modes of symmetric structures. *Physical Review B*, 61(15):10484–10503, April 2000.
- [120] Junxi Zhang and Lide Zhang. Nanostructures for surface plasmons. *Advances in Optics and Photonics*, 4(2):157–321, June 2012.
- [121] Sergey I. Bozhevolnyi, Valentyn S. Volkov, Eloïse Devaux, Jean-Yves Laluet, and Thomas W. Ebbesen. Channel plasmon subwavelength waveguide components including interferometers and ring resonators. *Nature*, 440(7083):508–511, March 2006.
- [122] Peter B. Catrysse, Georgios Veronis, Hocheol Shin, Jung-Tsung Shen, and Shanhui Fan. Guided modes supported by plasmonic films with a periodic arrangement of subwavelength slits. *Applied Physics Letters*, 88(3):031101–031101–3, January 2006.
- [123] Wei-Ping Huang. Coupled-mode theory for optical waveguides: an overview. *Journal of the Optical Society of America A*, 11(3):963–983, March 1994.
- [124] G. W. Cong, K. Suzuki, S. H. Kim, K. Tanizawa, S. Namiki, and H. Kawashima. Demonstration of a 3-dB directional coupler with enhanced robustness to gap variations for silicon wire waveguides. *Optics Express*, 22(2):2051–2059, January 2014.
- [125] Martin Suter and Peter Dietiker. Calculation of the finesse of an ideal Fabry–Perot resonator. *Applied Optics*, 53(30):7004, October 2014.
- [126] D. S. Ly-Gagnon, S. E. Kocabas, and D. A. B. Miller. Characteristic Impedance Model for Plasmonic Metal Slot Waveguides. *IEEE Journal of Selected Topics in Quantum Electronics*, 14(6):1473–1478, November 2008.
- [127] Philip McCord Morse, Philip McCord Morse, and Philip McCord Morse. *Vibration and sound*, volume 2. McGraw-Hill New York, 1948.
- [128] Bahaa E. A. Saleh and Malvin Carl Teich. *Fundamentals of Photonics*. Wiley, February 2013.
- [129] Pierre Berini. Bulk and surface sensitivities of surface plasmon waveguides. *New Journal of Physics*, 10(10):105010, October 2008.
- [130] Leif J. Sherry, Rongchao Jin, Chad A. Mirkin, George C. Schatz, and Richard P. Van Duyne. Localized Surface Plasmon Resonance Spectroscopy of Single Silver Triangular Nanoprisms. *Nano Letters*, 6(9):2060–2065, September 2006.

-
- [131] Yurii Vlasov and Sharee McNab. Losses in single-mode silicon-on-insulator strip waveguides and bends. *Optics Express*, 12(8):1622–1631, April 2004.
- [132] R. Soref and B. Bennett. Electrooptical effects in silicon. *IEEE Journal of Quantum Electronics*, 23(1):123–129, January 1987.
- [133] Hans P. Zappe. *Introduction to Semiconductor Integrated Optics*. Artech House, January 1995.
- [134] G. T. Reed, G. Mashanovich, F. Y. Gardes, and D. J. Thomson. Silicon optical modulators. *Nature Photonics*, 4(8):518–526, August 2010.
- [135] P. K. Tien. Light Waves in Thin Films and Integrated Optics. *Applied Optics*, 10(11):2395, November 1971.
- [136] John William Strutt, Lord Rayleigh. *Scientific Papers, Volume 1, 1869-1881*. Cambridge University Press, Cambridge, 1903.
- [137] H_ Davies. The reflection of electromagnetic waves from a rough surface. *Proceedings of the IEE-Part IV: Institution Monographs*, 101(7):209–214, 1954.
- [138] John C. Stover. *Optical Scattering: Measurement and Analysis*. Society of Photo Optical, Bellingham, Wash., USA, 2 edition edition, July 1995.
- [139] Jean M. Bennett. Characterization of Surface Roughness. In Alexei A. Maradudin, editor, *Light Scattering and Nanoscale Surface Roughness*, Nanostructure Science and Technology, pages 1–33. Springer US, 2007. DOI: 10.1007/978-0-387-35659-4_1.
- [140] Petr Beckmann and Andre Spizzichino. The scattering of electromagnetic waves from rough surfaces. *Norwood, MA, Artech House, Inc., 1987, 511 p.*, 1987.
- [141] A. Perot and Charles Fabry. On the application of interference phenomena to the solution of various problems of spectroscopy and metrology. *The Astrophysical Journal*, 9:87, 1899.
- [142] Max Born and Emil Wolf. *Principles of Optics: Electromagnetic Theory of Propagation, Interference and Diffraction of Light*. CUP Archive, February 2000.
- [143] Daniel Hofstetter and Robert L. Thornton. Theory of loss measurements of Fabry Perot resonators by Fourier analysis of the transmission spectra. *Optics Letters*, 22(24):1831–1833, December 1997.
- [144] D. Hofstetter and R.L. Thornton. Measurement of optical cavity properties in semiconductor lasers by Fourier analysis of the emission spectrum. *IEEE Journal of Quantum Electronics*, 34(10):1914–1923, October 1998.

Bibliography

- [145] Gaël David Osowiecki, Mohammad Madi, Ivan Shorubalko, Irène Philipoussis Fernandez, Edoard Alberti, Toralf Scharf, and Hans Peter Herzig. Standing wave integrated Fourier transform spectrometer for imaging spectrometry in the near infrared. In T.S. Pagano and J.F. Silny, editors, *Proceedings of SPIE*, volume 9611, San Diego, USA, 2015.
- [146] Robert O Green, Michael L Eastwood, Charles M Sarture, Thomas G Chrien, Mikael Aronsson, Bruce J Chippendale, Jessica A Faust, Betina E Pavri, Christopher J Chovit, Manuel Solis, Martin R Olah, and Orlesa Williams. Imaging Spectroscopy and the Airborne Visible/Infrared Imaging Spectrometer (AVIRIS). *Remote Sensing of Environment*, 65(3):227–248, September 1998.
- [147] J.S. Pearlman, P.S. Barry, C.C. Segal, J. Shepanski, D. Beiso, and S.L. Carman. Hyperion, a space-based imaging spectrometer. *IEEE Transactions on Geoscience and Remote Sensing*, 41(6):1160–1173, June 2003.
- [148] A Coradine, F Capaccioni, P Drossart, A Semery, G Arnold, U Schade, F Angrilli, M. A Barucci, G Bellucci, G Bianchini, J. P Bibring, A Blanco, M Blecka, D Bockelee-Morvan, R Bonsignori, M Bouye, E Bussoletti, M. T Capria, R Carlson, U Carsenty, P Cerroni, L Colangeli, M Combes, M Combi, J Crovisier, M Dami, M. C DeSanctis, A. M DiLellis, E Dotto, T Encrenaz, E Epifani, S Erard, S Espinasse, A Fave, C Federico, U Fink, S Fonti, V Formisano, Y Hello, H Hirsch, G Huntzinger, R Knoll, D Kouach, W. H Ip, P Irwin, J Kachlicki, Y Langevin, G Magni, T McCord, V Mennella, H Michaelis, G Mondello, S Mottola, G Neukum, V Orofino, R Orosei, P Palumbo, G Peter, B Pforte, G Piccioni, J. M Reess, E Ress, B Saggin, B Schmitt, ; Stefanovitch, A Stern, F Taylor, D Tiphene, and G Tozzi. Virtis : an imaging spectrometer for the rosetta mission. *Planetary and Space Science*, 46(9–10):1291–1304, October 1998.
- [149] Etienne le Coarer, Sylvain Blaize, Pierre Benech, Ilan Stefanon, Alain Morand, Gilles Léron del, Grégory Leblond, Pierre Kern, Jean Marc Fedeli, and Pascal Royer. Wavelength-scale stationary-wave integrated Fourier-transform spectrometry. *Nature Photonics*, 1(8):473–478, August 2007.
- [150] G. Lippmann. On Colour Photography by the Interferential Method. *Proceedings of the Royal Society of London*, 60:10–13, January 1896.
- [151] Gabriel Lippmann. Sur la théorie de la photographie des couleurs simples et composées par la méthode interférentielle. *J. Phys. Theor. Appl.*, 3(1):97–107, 1894.
- [152] P. Connes and E. Le Coarer. 3d Spectroscopy: The Historical and Logical Viewpoints. In *IAU Colloq. 149: Tridimensional Optical Spectroscopic Methods in Astrophysics*, volume 71, page 38, 1995.
- [153] Etienne Le Coarer, Sylvain Blaize, Pierre Benech, Ilan Stefanon, Alain Morand, Gilles Léron del, Grégory Leblond, Pierre Kern, Jean Marc Fedeli, and Pascal Royer. Wavelength-scale stationary-wave integrated Fourier-transform spectrometry. *Nature Photonics*, 1(8):473–478, August 2007. arXiv: 0708.0272.

-
- [154] Etienne Lecoarer and Pierre Benech. Detecteur et camera spectroscopiques interferentiels, June 2006. International Classification G02B6/42, G01J3/26; Cooperative Classification G01J3/45, G01J3/0205; European Classification G01J3/45.
- [155] Etienne Lecoarer and Pierre Benech. Interferential spectroscopy detector and camera, 2006. Classification internationale G01J3/26, G02B6/42; Classification coopérative G01J3/45, G01J3/0205; Classification européenne G01J3/45.
- [156] Minoru Sasaki, Xiaoyu Mi, and Kazuhiro Hane. Standing wave detection and interferometer application using a photodiode thinner than optical wavelength. *Applied Physics Letters*, 75(14):2008–2010, October 1999.
- [157] D. Knipp, H. Stiebig, S. R. Bhalotra, E. Bunte, H. L. Kung, and D. A. B. Miller. Silicon-based micro-Fourier spectrometer. *IEEE Transactions on Electron Devices*, 52(3):419–426, March 2005.
- [158] Jérôme Ferrand. *Etude et réalisation d'un spectromètre intégré à transformée de Fourier (SWIFTS)*. PhD thesis, Université de Grenoble, 2010.
- [159] Eva Ryckeboer, Xiaomin Nie, Ananth Z. Subramanian, Daan Martens, Peter Bienstman, Stephane Clemmen, Simone Severi, Roelof Jansen, Gunther Roelkens, and Roel Baets. CMOS-compatible silicon nitride spectrometers for lab-on-a-chip spectral sensing. volume 9891, pages 98911K–98911K–9, 2016.
- [160] Xiaomin Nie, Eva Ryckeboer, Gunther Roelkens, and Roel Baets. Novel Concept for a Broadband Co-propagative Stationary Fourier Transform Spectrometer Integrated on a Si₃N₄ Waveguide Platform. page JW2A.120. OSA, 2016.
- [161] Dennis Gabor and others. A new microscopic principle. *Nature*, 161(4098):777–778, 1948.
- [162] Christophe Bonneville, Fabrice Thomas, Mikhael de Mengin Poirier, Etienne Le Coarer, Pierre Benech, Thierry Gonthiez, Alain Morand, Olivier Coutant, Eric Morino, Renaud Puget, and Bruno Martin. SWIFTS: a groundbreaking integrated technology for high-performance spectroscopy and optical sensors. volume 8616, pages 86160M–86160M–15, 2013.
- [163] M. Malak, K. Jefimovs, I. Philipoussis, J. Di Francesco, B. Guldemann, and T. Scharf. Functional micro-nano structures for on-chip fourier transform spectrometers. In *2014 Symposium on Design, Test, Integration and Packaging of MEMS/MOEMS (DTIP)*, pages 1–4, April 2014.
- [164] Ph Nussbaum, R. Völkel, H. P. Herzig, M. Eisner, and S. Haselbeck. Design, fabrication and testing of microlens arrays for sensors and microsystems. *Pure and Applied Optics: Journal of the European Optical Society Part A*, 6(6):617, November 1997.

Bibliography

- [165] Maurine Malak, Irène Philipoussis, Hans Peter Herzig, and Toralf Scharf. Polymer based single mode optical waveguide for spectroscopy applications. volume 8846, pages 884615–884615–7, 2013.
- [166] Stefan Kunis, Daniel Potts, and Jens Keiner. Nonequispaced fast Fourier transform.
- [167] Mohammadreza Madi. *High spectral resolution waveguide spectrometer with enhanced throughput for space and commercial applications*. PhD thesis, École polytechnique fédérale de Lausanne, 2016.

Acknowledgements

During this five year long adventure, I had the chance to meet a lot of nice and interesting peoples whom I would like to thank a lot for the time and the help they invested for me. First of all I'd like to sincerely thank my thesis advisor Prof. Hans Peter Herzig. I was one of Hans Peter's former bachelor students at the University of Neuchâtel. And Hans Peter put his trust in me and accepted me as a PhD candidate in his laboratory. I want to specially thank him for his availability at all times and the freedom he gave me during my research. I could always count on his profound knowledge in the field of optics when I was searching for help.

I also would like to thank Dr. Toralf Scharf who guided me through the research on the stationary-wave integrated Fourier transform spectrometer. His deep understanding in the field of spectrometers, which he shared with me was really appreciated.

I would like to thank all my office mates, Dr. Ali Naqavi, Loic Hans, Michail Symeonidis and Babak Vosoughi. Thank you Ali for all our long and interesting discussions we had. From optical simulation techniques or mathematics to religion or Iran, it was always very enriching and a great pleasure. Thank you Loic to have always opened my mind to new discoveries. I was also happy to welcome a new neuchâtelois in the lab.

A big thank you also to my office neighbors Dr. Sara Santi, Grégoire Smolik and Daniel Infante who made me laugh when I needed it. Thank you Sara to have always carefully listen to my complains. To have taught me biology and surface chemistry. Thank you Grégoire, it is amazing how you were always available when I needed a bit of help. Your film maker skills will undoubtedly remain a legend. Thank you Dani, I really appreciated the time we spent together especially the motorcycle tours. I will also keep in mind all your advises about how to take care of orchids.

I would like to specially thank Dr. Nicolas Deschamps, Dr. Raphaël Barbey and Dr. Myun-Sik Kim. The actual team of Post-Docs. Nicolas for his tremendous and insatiable knowledge in optics. Raphaël who always has a quick answer for everything except when it was about chemistry. Myun-Sik which whom I went on boating trips on the lake. I would also like to thank Dr. Elsie Barakat who did an amazing work during her stay in the lab as Post-Doc. She was always ready to help me and share her precious knowledge with me.

Special thanks to the MIR team, Dr. Lubos Hvozďara and Joab Di Franscesco. I appreciated

Acknowledgements

the discussions about physics, fabrication technology and cleaving techniques, as well as the recipe for liquid nitrogen cooled ice-creams and a lot of other funny things...

A big "Merci" to Irène Philipoussis our cleanroom laboratory assistant. It was always a pleasure to work with you and learn about photolithography. Thank you also to Marcel Groccia our electronics engineer. Welding, repairing electronic boards, building photodiodes, were some of the multiple things I learned from you. Thank you Brigitte Khan, our beloved secretary, always available and ready to help.

Thank you also to all my other colleagues from the OPT group with whom I had the pleasure to work : Richa Dubey, Krishnaparvathy Puthankovilakam, Karin Prater, Johana Bernasconi, Sophiane Tournois, Dr. Qing Tan, Dr. Libo Yu, Dr. Vincent Paeder, Dr. Armando Cosentino, Dr. José Dintinger.

Merci à tous mes amis de Neuchâtel, Dr. Arnaud Felber, Dr. Marc Farine, Dr. Vincent Forster, Dr. Yaël Maeder, Carl Lindberg, Cédric Placi, Cyril Marthe, Gautier Lang, Giuliano Stendardo, Gregory Schaller, Mathieu Dubois, Morgan Rosier, Pascal Biedermann, Sébastien Biedermann, Sten Rettby. Ça fait du bien de pouvoir compter sur vous.

I would like to thank my family. My two sisters Léa and Line and especially my parents Ulrike Ernzer and Jacques Osowiecki, for their unconditional support during all these years. They greatly contributed to my natural curiosity and my love for science.

Finally I would profoundly thank my beloved Candice who during all these years was my unshakable source of inspiration. She was always there to support me in the good and the bad moments. Thank you for all these moments we shared and for all those we will in the future. I love you.

Neuchâtel, 17 Octobre 2016

G. Osowiecki



CV

Gaël Osowiecki

Curriculum Vitae

École Polytechnique Fédérale de Lausanne (EPFL)
Sciences et Techniques de l'Ingénieur (STI),
Institut de Microtechnique (IMT)
Optics & Photonics Technology Laboratory (OPT)
Rue de la Maladière 71b
2002 Neuchâtel - Suisse
☎ +41 76 562 17 12
✉ gael.oso@gmail.com

Educational Background

- 2011
2016

PhD Student, *École Polytechnique Fédérale de Lausanne (EPFL)*, EPFL STI
IMT OPT, Neuchâtel, Switzerland.
- 2011
2011

Internship, *Swiss Center for Electronics and Microtechnology (CSEM)*, Development of cavity enhanced spectroscopy based on extraordinary optical transmission, Neuchâtel, Switzerland.
- 2010
2011

MSc Thesis, *Department of Mechanical Engineering, Columbia University*, New-York, NY, USA.
- 2009
2010

MSc en Microtechnique, *École Polytechnique Fédérale de Lausanne (EPFL)*, Orientation: Micro & Nanosystèmes, Lausanne, Switzerland.
- 2009
2009

Internship, *Süss MicroTec Lithography GmbH*, Development of soft UV-nanoimprint (UV-NIL) lithography and conformal imprint lithography (SCIL), Garching, Germany.
- 2007
2009

BSc en Microtechnique, *Institut de Microtechnique - Université de Neuchâtel*, Neuchâtel, Switzerland.

Theses

PhD Thesis

TITLE Excitation of resonant plasmonic cavities by integrated waveguides for sensing applications

ADVISOR Professor Hans Peter Herzig

FUNDING AGENCY Swiss National Science Foundation

MSc Thesis

TITLE Air entrapment observation under impacting droplet by Frustrated Total Internal Reflection

ADVISOR Professor Daniel Attinger (Columbia University) and Professor Nicolas de Rooij (EPFL)

Research Interests

PHOTONICS

- Integrated optics
- Resonator optics
- Spectrometers
- Waveguides
- Diffractive optical elements

MICROFABRICATION

- Photolithography
- Electron beam lithography
- Thin film deposition
- Dry etching
- UV-LIGA
- Electroplating
- Electroless plating

Languages

French Native
English Fluent
German Fluent

Skills

Programming MATLAB, Labview, Python, Visual Basic, \LaTeX
Tools CST Microwave Studio, SolidWorks
Other Skills Communication, Organization, Leadership, Autonomous

Event Organization

2013

IONS-13 conference, EPFL-ETH Zürich, Switzerland.

The IONS-13 is jointly organized by the Swiss OSA student chapters at ETH Zurich and EPFL (Lausanne). The conference targets Master and PhD students in optics and photonics from all over the world.

Awards

2015

Best Poster Award, *International Symposium on Optomechatronics*, Neuchâtel, Switzerland, for his paper entitled: Stationary-wave integrated Fourier transform imaging spectrometer.

Publications

Peer-reviewed articles

- [1] OSOWIECKI, Gaël D. ; BARAKAT, Elsie ; NAQAVI, Ali ; HERZIG, Hans P.: Vertically coupled plasmonic slot waveguide cavity for localized biosensing applications. In: *Optics Express* 22 (2014), Nr. 17, S. 20871

- [2] KIM, Myun-Sik ; SCHARF, Toralf ; NGUYEN, David ; KEELER, Ethan ; RYDBERG, Skyler ; NAKAGAWA, Wataru ; OSOWIECKI, Gaël ; VOELKEL, Reinhard ; HERZIG, Hans P.: Light confinement effect of nonspherical nanoscale solid immersion lenses. In: *Journal of Micro/Nanolithography, MEMS, and MOEMS* 12 (2013), Nr. 2, S. 023015–023015

Conference proceedings

- [1] OSOWIECKI, Gaël D. ; MADI, Mohammad ; SHORUBALKO, Ivan ; PHILIPPOUSIS FERNANDEZ, Irène ; ALBERTI, Edoard ; SCHARF, Toralf ; HERZIG, Hans P.: Standing wave integrated Fourier transform spectrometer for imaging spectrometry in the near infrared. In: *Proceedings of SPIE* Bd. 9611. San Diego, USA, 2015
- [2] OSOWIECKI, Gaël D. ; BARAKAT, Elsie ; NAQAVI, Ali ; HERZIG, Hans P.: Localized biomolecular sensing enabled through plasmonic nanocavities. In: *Proceedings of SPIE* Bd. 9129. Brussels, Belgium : Spie-Int Soc Optical Engineering, 2014 (Proceedings of SPIE), S. 91292B
- [3] OSOWIECKI, Gaël D. ; COSENTINO, Armando ; TAN, Qing ; BARAKAT, Elsie ; ROUSSEY, Matthieu ; HERZIG, Hans P.: Plasmonic Slot Waveguides for Localized Biomolecular Sensing Applications. In: *European Conferences on Biomedical Optics (ECBO)*. Munich, Germany, 2013
- [4] NAQAVI, Ali ; SÖDERSTRÖM, Karin ; PAHUD, Céline ; OSOWIECKI, Gaël D. ; HAUG, Franz-Josef ; SCHARF, Toralf ; HERZIG, Hans P. ; BALLIF, Christophe: Light-trapping in the near field: the case for plasmonic thin-film solar cells. Tucson, Arizona, United States : OSA, 2013, S. RM2D.3
- [5] OSOWIECKI, Gaël D. ; COSENTINO, Armando ; TAN, Qing ; NAQAVI, Ali ; PAEDER, Vincent ; ROUSSEY, Matthieu ; HERZIG, Hans P.: Excitation of Metallic Nano-Cavities by a Silicon Waveguide for Localized Sensing Applications. In: *Proceedings of the EOS Annual Meeting 2012*. Aberdeen, Scotland, UK, 2012
- [6] KIM, Myun-Sik ; OSOWIECKI, Gaël D. ; SCHARF, Toralf ; KEELER, Ethan ; RYDBERG, Skyler ; NAKAGAWA, Wataru ; HERZIG, Hans P.: Investigating reflow and wetting of non-circular nano-pillars to study nano-scale solid immersion lens fabrication. In: *Proceedings of the EOS Annual Meeting 2012*. Aberdeen, Scotland, UK, 2012
- [7] KIM, Myun-Sik ; KEELER, Ethan ; RYDBERG, Skyler ; NAKAGAWA, Wataru ; OSOWIECKI, Gaël D. ; SCHARF, Toralf ; HERZIG, Hans P.: Reflow of non-circular nano-pillars to fabricate nano-scale solid immersion lenses. In: *Proceedings of the IEEE Photonics Society International Conference on Optical MEMS & Nanophotonics*. Banff, Alberta, Canada : IEEE, 2012

